Alma Mater Studiorum – Università di Bologna

DOTTORATO DI RICERCA IN

Scienze Biotecnologiche, Biocomputazionali, Farmaceutiche e Farmacologiche

Ciclo XXXIII

Settore Concorsuale: 05/E1

Settore Scientifico Disciplinare: BIO/10

TITOLO TESI

Convergent bioenergetic defects in Coenzyme Q10 depleted cells by pharmacological inhibition of coq2 enzyme (p-hydroxybenzoate polyprenyl transferase) and by genome editing technology targeting the encoding gene (COQ2)

Presentata da: Irene Liparulo

Coordinatore Dottorato

Prof.ssa Maria Laura Bolognesi

Supervisore

Prof.ssa Romana Fato

Co-supervisore

Prof. Christian Bergamini

Esame finale anno 2021

ALMA MATER STUDIORUM - UNIVERSITY OF BOLOGNA

PhD Programme in Biotechnological, Biocomputational, Pharmaceutical and Pharmacological Science

Convergent bioenergetic defects in Coenzyme Q10 depleted cells by pharmacological inhibition of coq2 enzyme (p-hydroxybenzoate polyprenyl transferase) and by genome editing technology targeting the encoding gene (COQ2)

PhD candidate: Irene Liparulo

***PhD Programme Coordinator**: Professor Maria Laura Bolognesi*

***Supervisor:** Professor Romana Fato*

***Co-supervisor**: Professor Christian Bergamini*

SSD BIO/10

CYCLE 33rd

TABLE OF CONTENTS

Abstract

Primary CoQ_{10} deficiency diseases encompass a heterogeneous spectrum of clinical phenotypes. Among these, defect or mutation on COQ2 gene, encoding a para-hydroxybenzoate-polyprenyl transferase, have been associated with different diseases. Understanding the functional and metabolic impact of COQ2 mutation and the consequent CoQ_{10} deficiency is still a matter of debate. To date the aetiology of the neurological phenotypes correlated to CoQ_{10} deficiency does not present a clear genotype-phenotype association. In addition to the metabolic alterations due to Coenzyme Q depletion, the impairment of mitochondrial function, associated to the reduced CoQ level, could play a significant role in the metabolic flexibility of cancer. This study aimed to characterize the effect of varying degrees of CoQ_{10} deficiency and investigate the multifaceted aspect of CoQ_{10} depletion and its impact on cell metabolism. To induced CoQ_{10} depletion, different cell models were used, employing a chemical and genome editing approach. In T67 and MCF-7 CoQ_{10} depletion was achieved by a competitive inhibitor of the enzyme, 4-nitrobenzoate (4-NB), whereas in SH-SY5Y the COQ2 gene was edited via CRISPR-Cas9 cutting edge technology.

1 INTRODUCTION

1.1 A brief historical perspective of CoQ_{10}

Coenzyme q10 was first isolated by heart beef mitochondria and then characterised and described by Morton and associates in Liverpool in 1955 [1] Crane in 1957 was the first scientist to establish CoQ_{10} as a molecule fundamental for respiratory chain. Wolf et al. determined its complex structure in 1958. Following its isolation by Crane and Green in the 1950s, CoQ Coenzyme Q was defined as a crucial component of oxidative phosphorylation, promoting the electrons transfer from CI and CII to CIII in the ETC. Further studies in following years confirmed its involvement in multiple aspects of cellular metabolism such as its function as a powerful antioxidant, an obligatory cofactor for UCP function, a regulator of mitochondrial permeability transition pores and of the physicochemical properties of membranes. Other new functions could be described in the future years. [2]

1.2 Coenzyme Q10 structure and distribution

Coenzyme Q, also named Ubiquinone (CoQ), is a highly hydrophobic molecule ubiquitously distributed in every eukaryotic cell membrane. Furthermore, Q 10 plays key roles in cell function. One of the most important is its role in the respiratory chain as an electron carrier. It has a pivotal role in oxidative phosphorylation and cell metabolism. Q10 distribution in tissues varies according to cell energetic demands. As a matter of fact, CoQ is known chemically as 2,3-dimethoxy, 5-methyl, 6-polyisoprene parabenzoquinone The polyisoprenoid tail length can vary in between 6 and 10 isoprene units between different species: nine isoprene units in mice (CoQ9), six in yeast (CoQ6), ten in human. [3] The reversible redox cycling is possible since the quinone ring is able to accept and donate electrons, while the isoprenoid tail serves mainly to anchor the Q10 in the membrane (Crane 2001). The distribution of CoQ_{10} is variable between tissue types, ranging from 8µg/g in lung to 114µg/g in heart. [2] Such extensive variation is likely to reflect differences in tissue energy needs. Variation in

CoQ_{10} content is also observed in the brain. Forebrain regions, particularly the striatum have high CoQ_{10} content. The cerebellum also has a relatively high level of CoQ_{10}. The white matter has the lowest CoQ_{10} content. It is hypothesised that the distribution of CoQ_{10} in the brain may reflect the variation in energy requirements. CoQ_{10} distribution could explain why a plethora of pathologies linked to a deficiency of this molecule target especially cells involved in tissue with high energetic demands, such as muscle and neurons.[4].

1.3 Coenzyme Q10 functions

Coenzyme Q10 displays a wide range of functions in the cell, some of them fundamental for cell metabolism. Abrogation of Q biosynthesis results in the incapacity of S. cerevisiae to grow on media containing non-fermentable carbon sources [5] and is embryonically lethal in mammals. [6] For these reasons Coenzyme Q is pivotal to the energetic metabolism of eukaryotes. It is a lipid-soluble electron transporter between NADH dehydrogenase (Complex I), succinate dehydrogenase (Complex II), and the bcl complex (Complex III) on the inner mitochondrial membrane. CoQ also plays additional roles, since is involved in pyrimidine biosynthesis, acting as an obligatory cofactor for dihydroorotate dehydrogenase. [7].It has also been described as a possible modulator of the mitochondrial Permeability Transition Pores (mtPTP)[8]. Furthermore, UQ is an active part of the electron transport systems of the plasma membrane and lysosomes.[9] CoQ_{10} is also broadly described and known for its antioxidant properties. It is a lipid-soluble antioxidant produced endogenously, able to prevent oxidative insults and possible damages of proteins, lipids and DNA. [10]

1.4 CoQ biosynthesis

Mammalians CoQ_{10} biosynthesis is not yet fully characterized. Yeast like S. cerevisiae represents a great useful model for understanding the biosynthesis of CoQ. Biochemical assays combined with molecular allowed to identify genes encoding enzymes required for CoQ biosynthesis. Tzagoloff was

one of the first scientist able to isolate and characterize some of the yeast COQ genes, from S Cerevisiae coq mutants, paving the way for further studies on CoQ biosynthesis in the eukaryotic cell. [11].CoQ biosynthesis requires several biosynthetic steps and it could be divided into four different stages: (i) head group production, (ii) tail production—including isoprene biosynthesis and tail polymerization, (iii) attachment of the tail to the head group, and (iv) a series of head group modifications. These different distinct pathways are located in the cytosol for the side-chain synthesis, and in the mitochondrial matrix for the benzoquinone ring modifications and CoQ assembly. Synthesizing enzymes, responsible for the benzoquinone ring modifications, (Coq3-9) are organised in a biosynthetic multi-subunit complex termed complex Q the mitochondrial oxidative phosphorylation complexes I–V are named in the same way) or CoQ synthome.[12]

1.4.1 Mevalonate pathway

Mevalonate pathway plays a key role in different cellular processes by synthesizing sterol isoprenoids, such as cholesterol, and non-sterol isoprenoids, such as dolichol, heme-A, isopentenyl tRNA and ubiquinone. It has been widely studied for cholesterol synthesis and its implications in cardiovascular diseases. It leads to the synthesis of FPP from Acetyl-CoA. In the case of coenzyme Q10 biosynthesis, the mevalonate pathway is accountable for the production of FPP, the isoprenoid tail of Q10. Acetyl-CoA, derived from glucose, glutamine and/or acetate, is involved in the initial stages of the mevalonate pathway. Three acetyl-CoA molecules produce 3-hydroxy-3-methylglutaryl CoA (HMG-CoA) in a two-step reaction, mediated by two different enzymes (acetoacetyl-CoA thiolase and HMG-CoA synthase). HMG-CoA is then reduced, via an irreversible reaction, by HMG-CoA reductase (HMGCR) to produce Mevalonate, a polyisoprene structure made up of 6 carbon. HMG-CoA is considered the central regulatory enzyme for the mevalonate pathway. However, this enzyme seems to play a further regulatory role in cholesterol biosynthesis and it is regulated through a feedback mechanism. [13]. MVA (6-carbon) is then converted into isopentenyl-diphosphate (IPP) which serves as

a monomeric unit for the consequent synthesis of all downstream metabolites in a so-called "head-to-tail" manner, such as 15-carbon intermediate farnesyl pyrophosphate (FPP). FPP constitutes the major branch-point in polyisoprene biosynthesis. This compound can participate in three different sets of enzymatic reactions. In the first set two FPP units, thanks to repeated "head-to-head" condensations, form squalene, the first intermediate for the sterol pathway. In the second set of reactions, FPP molecules are converted into long-chain polyisoprene alcohols. In the third set FPP condensate with isopentenyl, through "head-to-tail" polymerizations, producing long chains isoprenoids. The main features of these long-chain polyprenols are that double bonds are in the trans configuration. Once the chain length reaches 10 isoprene units in human cells, the polyisoprenil tail is transferred to the benzoquinone head in order to initiate COQ_{10} biosynthesis.[14]

1.4.2 CoQ head group biosynthesis

It is well known that the CoQ head group in mammals is derived from the essential amino acid phenylalanine, which is converted into tyrosine (Tyr) and, subsequently, 4-hydroxybenzoate (4-HB) [15]. Despite this, biosynthetic details of 4-HB production biosynthesis from tyrosine remain still a matter elusive

1.4.3 The last stage of CoQ biosynthesis –prenylation of ring precursor and Head Group Modifications

All the next steps of CoQ_{10} biosynthesis, starting with the attachment of the tail (polyisoprene chain) to the ring precursor (4-HB), occur in association with the matrix side of the IMM. The polysoprenil long chain is attached to the 4-HB head group thanks to an aromatic substitution, catalyzed by the mitochondrial polysoprenil transferases coq2, representing the rate-limiting enzyme for the biosynthesis of CoQ_{10}. Nevertheless, Mugoni et al. speculated that Ubiad1, a non-mitochondrial

prenyltransferase, might catalyze the biosynthesis in the Golgi membrane compartment.[16] For this reason the mitochondrial COQ2 enzyme could be not considered the only prenyltransferase able to catalyze this reaction. In the latter stages of CoQ_{10} biosynthesis a series of hydroxylations (at position 5 and 6) promoted by Coq6/COQ6 and Coq7/COQ7 respectively, O-methylation (Coq3/COQ3) and C-methylation (at position 2) (Coq5/COQ5), modify the 4-HB head group. The sequences of these reactions follow the chemical logic of electrophilic aromatic substitution (EAS) reactions on the aromatic ring. Subsequent ring modification steps include two hydroxylations at positions 5 and 6 of the ring structure that are catalyzed by different enzymes listed belove.

Function	H. sapiens
Elongation of prenyl side-chain	PDSS1/PDSS2
Prenalytion of ring precursor	COQ2
O5 and O6 methylation	COQ3
unknown	COQ4
C2-methylation	COQ5
C5-hydroxylation	COQ6
C6-hydroxylation	COQ7
	ADCK3
	COQ9
	COQ10A/10B

Figure 1 List of Genes and their functions required for ubiquinone biosynthesis in the last stages of CoQ_{10} biosynthesis

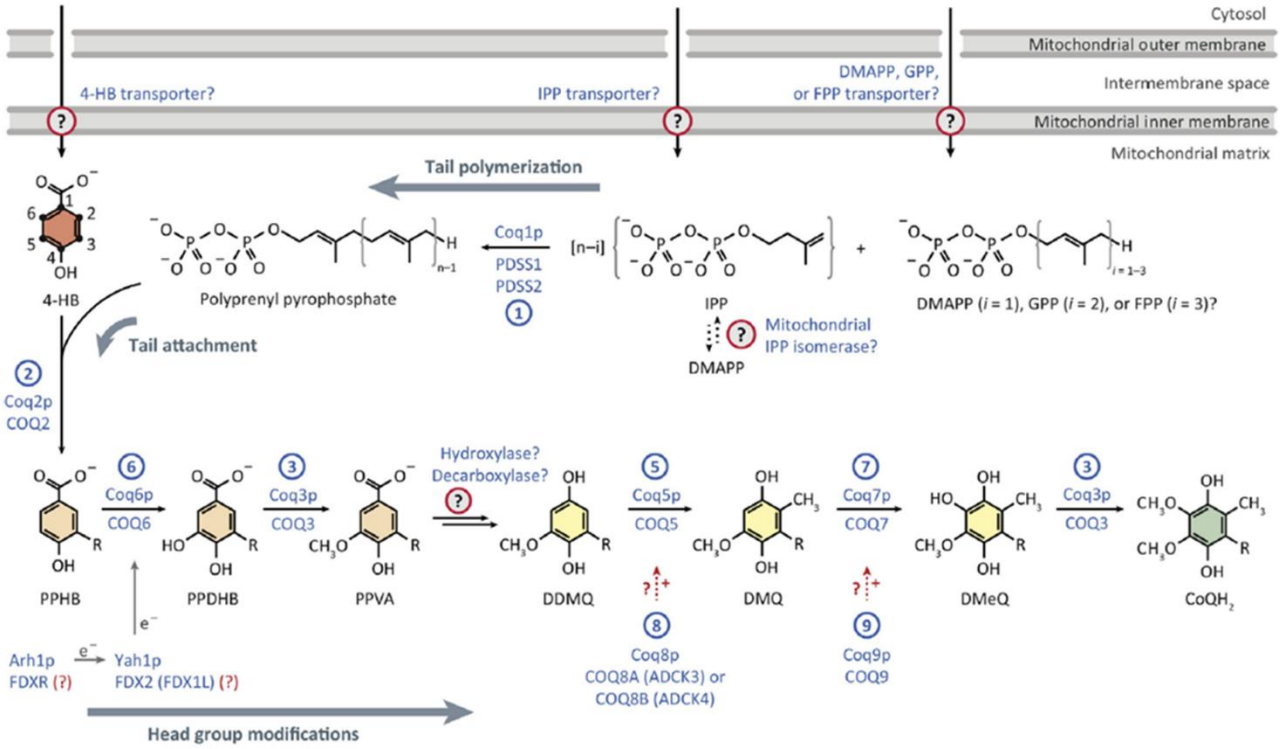

Figure 2 Diagram of the current model of UQ biosynthetic pathway in animals [17]

1.4.4 The CoQ Biosynthetic Complex

One of the main features of conserved CoQ biosynthesis in human cells and yeast is the presence of a high molecular high complex composed of the association of several CoQ proteins, able assembly like Coq3-Coq9 plus Coq11. Complex Q for human cells, termed CoQ-synthome for yeast, is involved in the terminal phase of CoQ biosynthesis and is required for an efficient CoQ biosynthesis. This complex has been characterized via proteomic analysis and immunoblotting assay (CIT.) It is located on the matrix face of the inner mitochondrial membrane and it is hypothesized that these complex can enhance catalytic efficiency and minimize the escape of intermediates that may be toxic due to their redox or electrophilic properties.[18] [19]

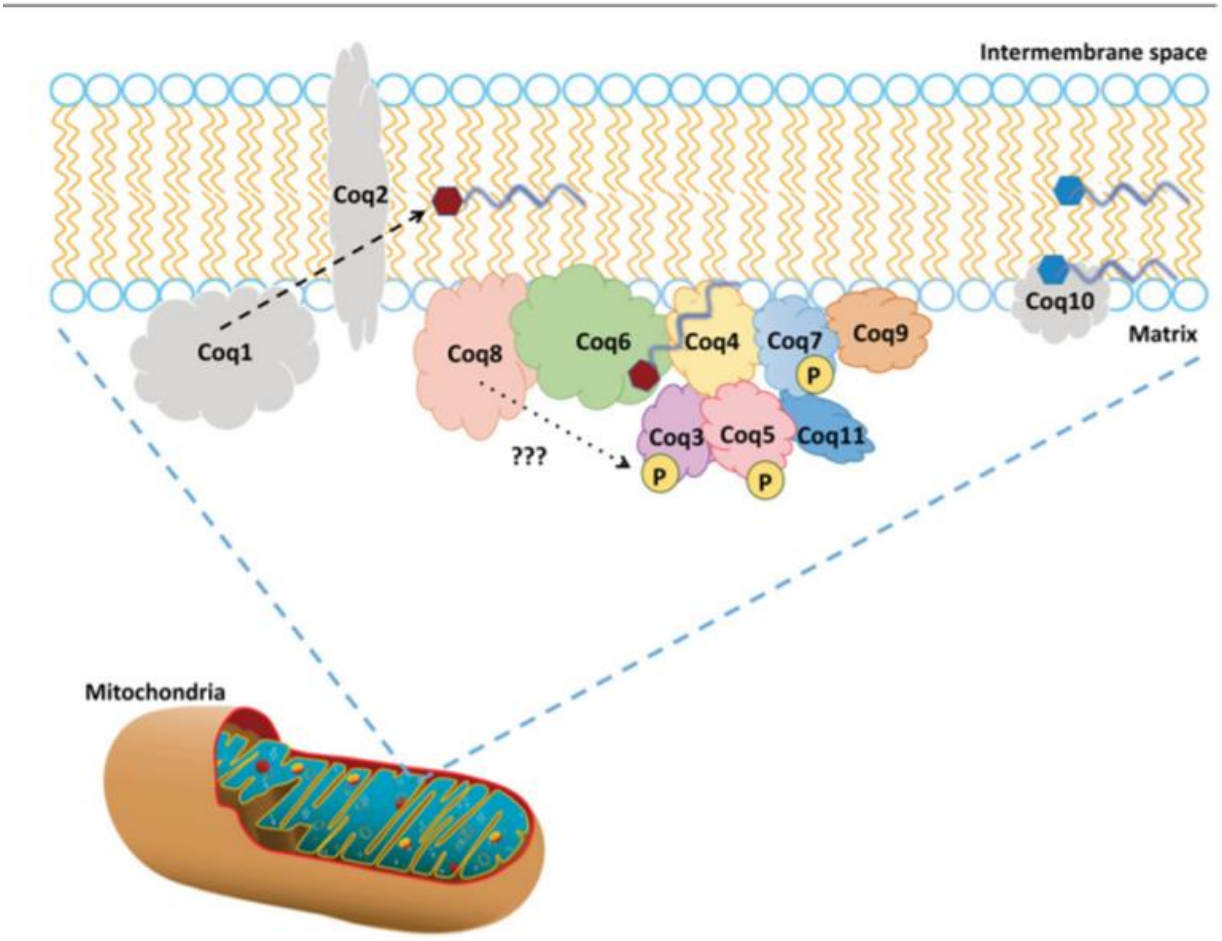

Figure 3 A model of the mitochondrial Q biosynthetic protein complex in S. cerevisiae. [20]

1.5 An overview on CoQ_{10} human deficiencies

1.5.1 Primary CoQ_{10} deficiencies

In the last two decades, there has been a growing number of human patients showing deficiencies of UQ10, often associated with myopathy [21]. Ogasahara et al. [1989] were the first to establish a clinical case of coenzyme Q 10 (CoQ_{10}) deficiency, seemingly of the primary form.[21] Primary CoQ_{10} deficiency, often inherited in an autosomal recessive manner, it is described in several cases as a severe and rare disease that often presents with multisystem disorders. Early diagnosis and interventions are imperative in the management of these kinds of patients: it could be lethal if it is not treated effectively. To date, mutations in seven of the nine genes encoding proteins required for the final

phase of CoQ_{10} biosynthesis inside mitochondria have been reported and more can be expected to follow. [18] Despite these interesting findings, there are not yet clear genotype-phenotype associations and some aspects are elusive. As a matter of fact primary UQ deficiency, like most mitochondrial disorders, often presents with very heterogeneous clinical manifestations, encompassing at least 5 major phenotypes, including the following: 1) encephalomyopathy, characterized by recurrent myoglobinuria, brain involvement, and ragged red fibers; 2) severe infantile multisystemic disease; 3) cerebellar ataxia; 4) Leigh syndrome with growth retardation, ataxia, and deafness; and 5) isolated myopathy.[22] This kind of classification should be probably updated and supposed to be too simplified because of two main reasons: the range of clinical phenotypes is much wider and some phenotypes could be overlapped. CoQ_{10} deficiency disease manifestations could be interpreted taking into account the relatively higher susceptibility that organs such as skeletal muscle, cerebellum and kidney have to damage under conditions of UQ deficiency. A wide variety of biochemical alteration and features, like reduced activities of respiratory chain complexes, oxidative stress, impaired pyrimidine biosynthesis and increased mitophagy, have been observed in all these phenotypes. This heterogeneity in the clinical presentations suggests that multiple pathomechanisms are implied. The age of onset, how the disease could progress and response to UQ_{10} therapy vary greatly among these different cases.

1.5.1.1 COQ2 (encoding PHB-polyprenyl transferase)

CoQ2 gene encoding an enzyme required for the attachment of the polyisoprenyl 'tail' to 4-HB, one of the final step of CoQ_{10} biosynthesis. Coq2 is an integral membrane protein of the inner mitochondrial membrane is imported into mitochondria via the Tim23 pathway.[23] It was originally hypothesized that coq2 might serve to anchor the CoQ-synthome to the inner mitochondrial membrane, however, there is no evidence that coq2 is associated with the other Coq polypeptides that assemble into the CoQ-synthome. [24] At least nine mutations in the COQ2 gene have been found

so far. These mutations are responsible to cause a disorder known as primary coenzyme Q10 deficiency. COQ2 mutations, leading to Q10 deficiency, are accountable for a wide spectrum of disease, usually occurring in infancy or early childhood, but it can become apparent at any age. It can affect many parts of the body, most often the brain, muscles, and kidneys. [25] Quinzii and colleagues described for the first time in 2005 a homozygous missense mutation in the COQ2 gene in two siblings with infantile steroid-resistant nephropathy, and subsequent encephalomyopathy in the eldest child [26]. Both patients have shown CoQ_{10} deficiency in muscle and fibroblasts and decreased activities of CI+III and CII+III in either fibroblasts or muscle. In 2007, Mollet and colleagues reported single base-pair frameshift deletion resulting in a premature stop codon in exon 7 of the COQ2 gene, modifying the last 21 amino acids of the protein. This patient presented with neonatal neurological distress, liver failure, nephrotic syndrome, diabetes mellitus, pancytopenia, seizures, lactatemia and died at 12 days of multisystem failure.[27] CoQ_{10} quantifications revealed a decrease in fibroblasts and enzymological studies of liver homogenate revealed a decrease in Complex I/III and Complex II/III activities. Combined Complex I/III and II/III activities are dependent upon CoQ_{10} thus we would expect the activities to be low in a CoQ_{10} deficient patient. Diomedi-Camassei et al (2007) reported a COQ2 mutation in two patients with early-onset glomerular lesions. The first had the steroid-resistant nephrotic syndrome, with no extra-renal symptoms. The second patient presented with oliguria which rapidly developed into end-stage renal disease and died at 6 months of epileptic encephalopathy complications. Both patients had decreased levels of CoQ_{10} and Complex II/III activity in muscle (Complex I/III not measured). Complex I activity was also decreased and Complex II, III and IV were at the lower limit of the reference range.[28] Thus to date six patients have been identified as having COQ2 gene mutations. COQ2 (p-hydroxybenzoate polyprenyl transferase) encodes the enzyme required for the second step of the final reaction sequence of Coenzyme Q10 (CoQ) biosynthesis. Its mutations represent a frequent cause of primary CoQ deficiency and have been

associated with the widest clinical spectrum, ranging from fatal neonatal multisystemic disease to late-onset encephalopathy.

1.5.2 Diagnosis of primary coenzyme Q10 deficiency

To date, there are no formal or diagnostic criteria for primary coenzyme Q10 deficiency medical diagnosis. Primary coenzyme Q10 deficiency should be suspected in individuals with some certain clinical findings such as:

- Steroid-resistant nephrotic syndrome (SRNS)
- Clinical features of mitochondrial encephalomyopathy, including neurologic findings (hypotonia, seizures, dystonia, nystagmus, cerebellar ataxia or pyramidal dysfunction, spasticity, peripheral neuropathy, and intellectual disability), myopathy, retinopathy, or optic atrophy, sensorineural hearing loss, and/or hypertrophic cardiomyopathy.
- Unexplained ataxia
- Subacute exercise intolerance

Despite these aspects, Q10 deficiency diagnosis is very challenging since the clinical manifestations previously described present a great variability and their onset is still silent at birth and it occurs later, leading within a few days or months to multiorgan failure and consequently to death of the newborn. For these reasons several times, diagnosis is assessed only post mortem. In order to avoid this, a combination of biochemical and clinical diagnosis could implement the exome sequencing and could save lives and improve also prenatal genetic counselling. [29]

1.5.2.1 Biochemical Testing

- Detect levels of CoQ_{10} in skeletal muscle. While coenzyme Q10 tissue content measurements may be performed on cultured skin fibroblasts or blood mononuclear cells,

these tissues may not be reliable in detecting secondary coenzyme Q10 defects [Yubero et al 2015].

- Assessment of complex I+III and II+III activities of the mitochondrial respiratory chain on frozen muscle homogenates. [Rahman et al 2012]

1.5.3 Secondary CoQ_{10} deficiencies

Secondary CoQ_{10} deficiency is less studied than primary ones. They are not linked to mutations in genes directly responsible for CoQ_{10} biosynthesis but may be linked to assembly defects in oxidative phosphorylation (OxPhos) complexes and metabolic pathways

1.5.4 Treatment of human CoQ_{10} deficiencies

Deficiency is not expected to occur in healthy individuals because endogenous production is usually sufficient. Despite this, different studies show how CoQ_{10} amount could decrease with ageing. However, in individuals with primary deficiency of CoQ_{10} or those on statin therapy, the dietary contribution becomes more important and, in some cases, even crucial. Due to the small contribution of CoQ_{10} from the diet, supplementation is the easiest way to increase CoQ_{10} levels to meet physiological requirements. To limit irreversible tissue damage, therapy should be initiated as soon as possible The identification of mutations in genes involved in CoQ_{10} deficiency could allow prenatal diagnosis and treatment from birth since the effectiveness of treatment could be affected by more advanced disease status at the time of the beginning of treatment. [30] The replacement treatment depends on the percentage of the cells remaining in the affected tissues that could be rescued. Some manifestations could be restored whereas some progression of CoQ_{10} deficiency pathologies could be totally or partially reversed unless severe neurologic and/or renal damage are present. [31] Ongoing research has great potential to help guide treatment strategies and genetic counselling.[29] Since the dietary contribution of CoQ_{10} is minimal, the body relies on the endogenous synthesis of this coenzyme. Normal levels of endogenous CoQ_{10} range between 0.55 mg/L and 1.87 mg/L.[32]

Supplementation with oral UQ10 has been shown to be effective in the individuals with mutations in PDSS1, COQ2, COQ4, COQ6 or COQ8/ADCK3 [33] [34] However, the patients born with defective *PDSS2* or *COQ9* genes did not respond to UQ10 and died despite UQ10 treatment. [34]

1.5.5 Chemical Analogs of 4-Hydroxybenzoic Acid on Coenzyme Q Biosynthesis

Parson and Rudney described for the first time 4-HB together with 4-Hbz (4-hydroxybenzaldehyde) as potential precursors of the benzoquinone ring of CoQ in animals, yeast, and bacteria. [35] The origin of 4-HB is not the same across diverse species. In Escherichia coli, 4-HB derived from chorismate pyruvate-lyase reaction catalyzed by UbiC (Nichols and Green, 1992; Siebert et al., 1992), which substrate is chorismic acid. Since the shikimate pathway is not present in animals, in this case, 4-HB derives from tyrosine and phenylalanine. As previously described in section *2.4.3*, 4-HB is prenylated by the enzyme coq2 in eukaryotes and UbiA in bacteria, taking part in the last stage of CoQ biosynthesis, and promoting prenylation in position C3. Aromatic compounds act as substrates or inhibitors of UbiA and coq2 if they fulfil some specific chemical-structural requirements. Substrates have carbon on position C3 activated by a carboxylic acid moiety on C1 and a group on C4 that is electron and hydrogen bond-donor, like hydroxyl or amine groups, whereas aromatic compounds, with electron-withdrawing groups on C4, such as nitro and chloro, inhibit the activity of UbiA or coq2.[36]

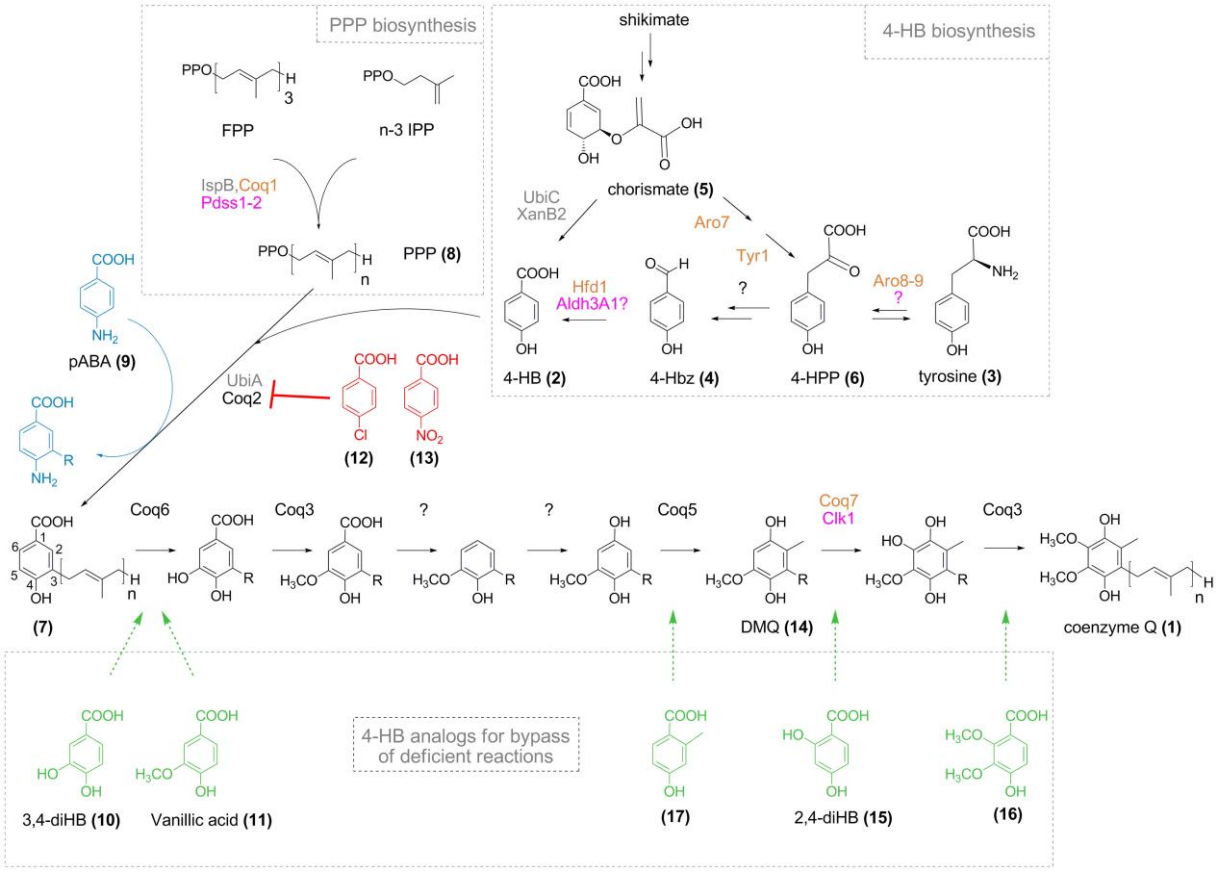

Figure 4 CoQ biosynthesis, effect and mechanism of 4-HB analogues (green, red and blue structures).4-NB is the red structure (13). [17]

For these reasons, 4-HB analogue such as 3,4-dihydroxybenzoic acid (3,4-diHB) and 4-hydroxy-3-methoxy-benzoic acid are used to bypass deficiencies in some steps of CoQ biosynthesis, while 4-HB analogue like 4-nitrobenzoate (4-NB) and 4-clorobenzoate (4-ClB) are used to inhibit CoQ_{10} biosynthesis. Interestingly pABA (4-aminobenzoate) is prenylated by UbiA and coq2, but since mammalian cells are not able to replace the C4 amino group with a C4 hydroxyl group, C4-aminated intermediates of the CoQ pathway are accumulated determining decreased CoQ levels in mammalian cells. Therefore pABA is used as a CoQ biosynthesis inhibitor in mammalian cells. [37] [38] Using 4-HB analogues bypassing CoQ_{10} biosynthesis, could be considered a therapeutic alternative for CoQ_{10} deficiency treatment[39]. However, 4-HB analogues able to inhibit the prenyltransferase reaction could be not used only to elucidate some CoQ biosynthesis steps still uncharacterized, but also to obtain

CoQ deficient models to decipher Coq deficiency metabolic impairments. Forsman et al reported the first study describing how 4-NB, in a dose and time-dependent manner, could impair CoQ_{10} biosynthesis [40] Following study by Quinzii et al. reported how 4-NB treated cells with different Q10 residual levels reshape the bioenergetic profiles. [41] Among the different coq2 inhibitors, 4-NB is the most valuable and used, since 4-NB treatment does not interfere with cell viability nor acted as a pro-oxidant or antioxidant.[40], whereas 4-aminobenzoate derivatives interfere with chromatographic Q detection and 4-chlorobenzoate presented cytotoxic effects. [42]

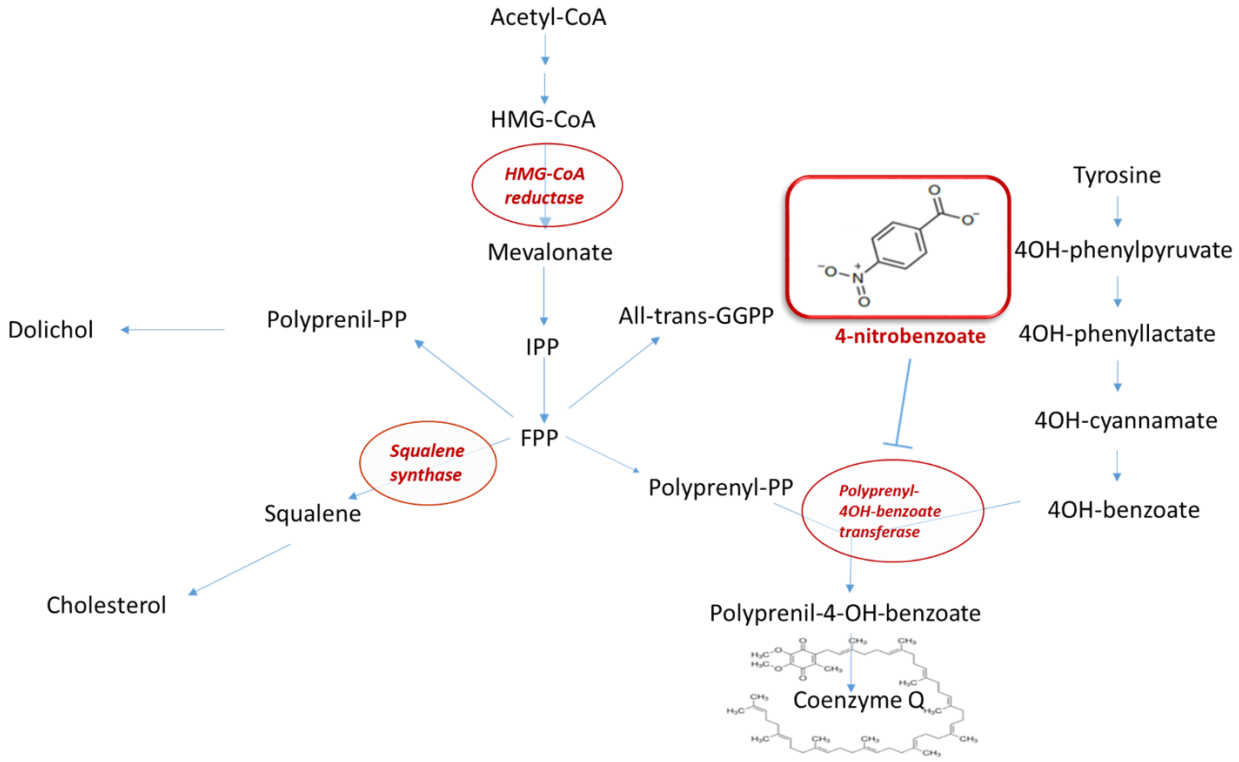

Figure 5 Detailed Mechanism of action of 4-nitrobenzoate. 4-NB is a competitive inhibitor of the enzyme coq2, which is responsible for one of the last fundamental step of CoQ assembly.

Aim of the study

Disorders of Coenzyme Q10 (CoQ_{10}) biosynthesis frequently show neurological and extra neurological involvement such as cerebellar ataxia and/or seizures.[32] Since coenzyme Q10 deficiency, like most mitochondrial disorders, often shows very heterogeneous clinical manifestations, targeting especially cell involved in tissue with a high energetic need, such as muscle and neurons, employing cell line as a tool to study CoQ_{10} depletion, could be useful to understand the complex pathogenesis of the disease.

On the other hand, targeting mitochondria, by inhibition of CoQ_{10} biosynthesis, could be insightful in an attempt to understand cancer metabolism. Investigating CoQ_{10} inhibition in cancer cell metabolism could be useful to understand the mechanisms underpinning cancer cell metabolic plasticity and identify new molecular targets and strategies for future therapies.

To address these points we have established different cell models of CoQ_{10} deficiency.

In MCF-7 and T-67 cell, we obtained CoQ_{10} inhibition by pharmacological inhibition of coq2 by 4-NB, a competitive inhibitor.

In the second case, we exploited a neuronal SH-SY5Y cell line and cutting edge genome editing CRISPR-Cas9, to better clarify whether a genetic mutation could have the same effect as a pharmacological one on CoQ_{10} biosynthesis inhibition. Then, we try to identify metabolic impairments related to CoQ_{10} deficiency, evaluating to what extent CoQ depletion verified in homozygous, heterozygous and pharmacological condition, affect the cell metabolism. In addiction, we tried to define the effect of different Q10 deficiency, previously described as mild or partial (more than 50% residual Q10) or severe (less than 30% of normal). [43] These neuronal cell models (SH-SY5Y and T67) have been chosen since neurological manifestations are very common in CoQ_{10} deficient patients and could provide new insights into the effects of CoQ_{10} deficiency on neuronal mitochondrial function and oxidative stress, opening possible avenues for testing new

pharmacological treatment to ameliorate CoQ_{10} deficiency in patients and investigate genotype-phenotype associations of coq2 inhibition.

This thesis is intended to:

- obtaining Q10 depleted cell line by:
  - targeting the gene COQ2 by genome editing CRISPR-CAS 9 in SH-SY5Y cell,
  - chemical inhibition using a competitive inhibitor 4-HB analogue (4-NB) for T-67 and MCF-7 cell;
- biochemical, metabolic and proliferative characterization
- defining the mechanism of the bioenergetic defects of the cell lines obtained.

2 MATERIALS AND METHODS

2.1 Cell lines

The T67 human glioma cell line was derived by Lauro et al.[44] from World Health Organization (WHO) grade III gemistocytic astrocytoma. Cells were cultivated in Dulbecco's modified Eagle's medium (DMEM; Euroclone, Milan, Italy) containing 1 g L^{-1} glucose, supplemented with 10% fetal bovine serum (FBS), 1% penicillin/streptomycin, 2 mM glutamine and maintained at 37 °C in 5% CO_2 with saturating humidity.

MCF7 breast cancer cells (ATCC, Manassas, VA, USA) were cultured in Dulbecco's Modified Eagle Medium (DMEM; Euroclone, Milan, Italy) containing 5 g L^{-1} glucose, supplemented with 10% FBS, and 2 mM glutamine. Cells were grown at 37°C and 5% CO_2 in a humidified cell culture incubator.

SH-SY5Y cells (ATCC, Middlesex, UK) cells were cultured in Dulbecco's modified Eagle's medium (DMEM; Euroclone, Milan, Italy) containing 5 g L^{-1} glucose, supplemented with 10% (v/v) fetal bovine serum, 100 U/mL penicillin and 100 µg/mL streptomycin (Sigma-Aldrich, St. Louis, MO, USA) and uridine (10 µM).

2.2 Cells treatment

For CoQ depletion, cells were grown for 4 days in complete DMEM supplemented with 4 mM 4-nitrobenzoic acid (4-NB). For exogenous CoQ supplementation experiments, cells were grown for 4 days in the presence of 4 mM 4-NB and additional 24 hours in the presence of 4 mM 4-NB and 0.1 µM of a water-soluble coenzyme Q10 formulation (Q) [45]. For cholesterol removal experiments, cells were cultured in six-well dishes as described above. Then, cells were washed with PBS and incubated in the absence or presence of 1 mM methyl-β-maltodextrin (CD) in DMEM for 30 min at 37 °C in 5% CO_2. After removal of the medium, cells were washed thoroughly with PBS, to get rid of residual CD,

and subjected for further analysis. For cell viability assessment, cells were plated at the density of 5 × 104 cells per well in a six-well dish in the presence of 4 mM 4-NB, 4 mM 4-NB + 0.1 µM Q, or vehicle. Cell count was performed by Trypan blue exclusion method.

2.3 Generation of COQ2 mutant SH-SY5Y cell line

SH-SY5Y cells (American Type Culture Collection, Manassas, VA, USA) were cultured in DMEM (EuroClone, Pero, Italy) supplemented with 10% (v/v) fetal bovine serum, 100 U/ml penicillin, and 100 mg/ml streptomycin (MilliporeSigma, Burlington, MA, USA). Knockdown experiment was performed using Alt-R® CRISPR-Cas9 System (IDT, IL, USA) following the manufacturer's protocol. To knockdown COQ2 we targeted exon 1 using a predesigned Alt-R®. CRISPR-Cas9 crRNA (GGGCTGCAAGTCACCACCGT)(https://eu.idtdna.com/site/order/designtool/index/CRISPR_PREDESIGN), purchased form IDT. The crRNA was incubated with Alt-R® CRISPR-Cas9 tracrRNA ATTO™ 550, and then with Alt-R® S.p. HiFi Cas9 Nuclease V3 to prepare the ribonucleoprotein (RNP) complex. Cells were plated at 80% confluence and transfected. After 30 hours, cells were sorted with an automated Fluorescence-Activated Cell Sorting system (Influx, Becton Dickinson, Franklin Lakes, NJ, USA), and single cells were plated in 96-well plates coated with Poly-D-Lysine (MilliporeSigma). Clones were amplified and screened by PCR and direct sequencing of the target region. Different clones carrying the specific change and with no off-target mutations were selected for the analysis. The SH-SY5Y clone that underwent the same CRISPR/Cas9 genome editing approach but did not carry any change was used as a control cell line (hence defined WT throughout the text).

2.4 COQ2 Mutation Detection

For genomic detection of the COQ2 mutation, a touchdown PCR was performed with 100ng of gDNA. PCR conditions were 1 cycle of 5 minutes at 95,8 °C; 24 cycles of 30 seconds at 95,8 °C, 30 seconds at 628C (–0.58C per cycle), 1 minute at 72,8 °C; 6 cycles of 30 seconds at 95,8 °C, 30 seconds at 50 ° C, 1 minute at 72C; 1 cycle of 10 minutes at 72 °C. PCRs were resolved in 1% agarose gels.

2.5 HPLC analysis

2.5.1 Coenzyme Q extraction

Coenzyme Q extraction was performed as described by Takada et al. [46]. Quantification of CoQ_{10} was performed by HPLC analysis (two-pump system equipped with a photodiode array detector, Agilent, Santa Clara, CA, USA 1100 series). Briefly, 20 µL of ethanolic extract was chromatographed on a C18 Column (Kinetex, Phenomenex, Torrance, CA, USA, 2.6 µm, 100 × 4.6 mm), using a mobile phase consisting of ethanol: water (97: 3, v/v) at a flow rate of 0.4 mL min−1. CoQ peak at λ = 275 nm was identified by comparison and co-elution with a standard. The quantification of CoQ was obtained by peak area measurement compared with standard curves, according to Bergamini et al. [45]

2.5.2 Cholesterol extraction

The total cholesterol content of cells was quantified by HPLC according to Contreras et al. [47] with minor modifications. External cholesterol standards were used for calibration. All the samples were analysed in triplicate. Briefly, cells were detached by trypsinization, washed with PBS, and centrifuged at 300 g for 3 min. The supernatant was discharged, and pelleted cells were treated with lysis buffer (0.1% Triton X-100 v/v) to a final protein concentration of 0.5 mg mL−1. Then, 20 µL of reaction mix (500 mM MgCl2, 500 mM Tris buffer (pH 7.4), 10 mM dithiothreitol, 5% sodium cholate (w/v), 0.1% Triton X-100 (w/v)), 0.8 U mL−1 cholesterol oxidase (Sigma-Aldrich, St. Louis, Missouri, MO, USA), and 0.8 U mL−1 cholesterol esterase (Sigma-Aldrich;) were added to 100 µL of cell lysate. The solution was incubated at 37 °C for 30 min, and the reaction was stopped by adding 100 µL of a 1: 1 methanol/ ethanol (v/v) solution. After 30 min of incubation at 0 °C, the solution was centrifugated at 10 000 g for 10 min. Then, 10 µL of the supernatant was analyzed by HPLC on a Kinetex C18 Column (100 × 4.6 mm, 2.6 µm; Phenomenex). Absorbance at λ = 240 nm was monitored by a photodiode array detector. All experiments were performed in triplicate.

2.5.3 Lactate determination.

The lactate was detected and quantified by HPLC in the culture medium at time 0 and after 6 hours of 1µM oligomycin A treatment (time 6). The Δ-lactate was calculated by subtracting the peak area of lactate at time 6 minus time 0 and normalized on cellular protein content [48]. For lactate determination, the culture medium was diluted 1:10 in the mobile phase and centrifuged at 14000 g for 5 minutes at 4°C. Then, the supernatant was injected in an HPLC system (Agilent 1100 series system) equipped with a phenylic column (Agilent ZORBAX SB-Phenyl, 5 µm, 250×4.6 mm), using a mobile phase consisting of 50 mM KH2PO4, pH 2.9, at a flow rate of 0.8 ml/min. Absorbance at λ=210nm was monitored by a photodiode array detector. To quantitate the amount of lactate, external calibration standards were used. All injections were performed in triplicate.

2.5.4 Adenine nucleotides measurement

Cellular ATP, ADP, and AMP were extracted and detected as described by Jones [78] by HPLC using a Kinetex C18 Column (250 × 4.6 mm, 100 A, 5 µm; Phenomenex). Nucleotide peaks were identified at λ = 260 nm by comparison and co-elution with the standards. The quantification of different nucleotides was obtained by peak area measurement compared with standard curves.

2.5.5 Glutathione determination

Glutathione determination. Intracellular glutathione (GSH) level was measured by HPLC after derivatization with N-ethylmaleimide (NEM) following Giustarini et al. [49]

2.6 Cellular respiration

Cells were cultured in Petri dishes 10 cm diameter and treated as described above. Then, after 48 hours, cells were harvested at 70-80% confluence, washed in PBS, resuspended in complete medium and assayed for oxygen consumption at 30°C using a thermostatically controlled oxygraph (Instech Mod. 203, Plymouth Meeting, PA, USA). Endogenous respiration was measured in DMEM and

compared with the one obtained after injection of 1 µM oligomycin A and 1–6 µM FCCP (carbonyl cyanide 4-(trifluoromethoxy) phenylhydrazone). 5 µM antimycin A was added at the end of the experiments to completely block mitochondrial respiration. Data, expressed as nanomoles of O_2 consumed, were normalized on the cellular protein content, determined by the Lowry method, or on number of cells.

2.7 Measurement of mitochondrial potential (ΔΨm)

Walker and colleagues protocol for measurement of mitochondrial potential was followed with minor modifications.[50] ΔΨm changes were measured in intact cells or in cells permeabilized with 10 µg mL^{-1} digitonin, using a Jasco FP-777 spectrofluorometer, (Jasco, Tokyo, Japan) equipped with a stirring device. Briefly, cells were cultured in Petri dishes and treated as described above. After 24 hours, cells were trypsinized and were washed twice with PBS. 1.5×10^6 cells were resuspended in 2 mL of solution containing 0.25 M sucrose, 10 mM HEPES, 5 mM KH_2PO_4, 1mM EDTA, 50 µM EGTA (pH 7.4), and 100 nM TMRM (λex 558 nm; λem 578 nm; Thermo Fisher). In experiments with intact cells, TMRM fluorescence changes were recorded following the addition of 1 µM oligomycin A and 2 µM FCCP. In experiments with permeabilized cells, 10 µg mL^{-1} digitonin was added and TMRM fluorescence changes were recorded following the addition of 2.5 mM glutamate/malate, 0.1 mM adenosinediphosphate (ADP), 1 µM oligomycin A, 1 µM rotenone, 5 mM succinate, and 2 µM FCCP.

2.8 Pyruvate Kinase (PK) Activity

Pyruvate kinase activity was measured by a continuous assay coupled to lactate dehydrogenase (LDH)[51]. NADH absorbance was followed spectrophotometrically at 340 nm (ε = 6220 M^{-1} cm^{-1}) using a spectrophotometer (Jasco V-550) equipped with thermostatic control and stirring device. Kinetic assays for activity determinations contained cell lysate (1–2 µg), Tris pH7.5 (50 mM), KCl (100 mM), $MgCl_2$ (5 mM), ADP (0.6 mM), NADH (180 µM) and LDH (8 units). Different concentrations of

phosphoenolpyruvate (PEP) ranging from 0 to 1.5 mM were added to initiate the reactions. Michaelis-Menten plot and Lineweaver-Burk plot were used to analyze the Vmax and Km of PK.

2.9 NAD^+-Dependent and $NADP^+$-Dependent Enzyme Activity

NAD+ and NADP+ dependent enzyme activity was measured in cell lysates following resorufin fluorescence emission (λ_{exc} 550 nm; λ_{em} 590 nm). The reaction was performed in a 96-well microplate and measured using a multi-plate reader (EnSpire; PerkinElmer). Briefly, 50 μg of cell lysate was mixed with 1 mM $MgCl_2$, 0.1 mM $CaCl_2$, 3 mM NAD^+ or $NADP^+$, 10 μM rotenone and 200 μM resazurin in 50 mM MOPS buffer (pH 7.4). Then, 10 mM of specific substrates of lactate dehydrogenase (LDH), pyruvate dehydrogenase (PDH), $NADP^+$-dependent isocitrate dehydrogenase (IDH), NAD^+-dependent isocitrate dehydrogenase (IDH), α-ketoglutarate dehydrogenase (KGDH), malate dehydrogenase (MDH), malic enzyme (ME), glutamate dehydrogenase (GDH) and glutaminase (GLS) were added to start the reactions. The linear part of the product accumulation curves was used for the reaction rate determination. In each experiment, fluorescence from four wells was averaged and NAD(P)H: resazurin oxidoreductase rates of the CoQ depleted cells were expressed as a percentage of the rates exhibited by the control cells.

2.10 Spheroid formation assay

Suspension method described by Froehlich et al. [52] was followed with minor modifications for the spheroids formation assay. Briefly, to test the effect of CoQ depletion on spheroids formation, cells were seeded at 1 x 10^5 density in μ-Dish 35 mm, high Bioinert (Ibidi, Germany), in complete medium with 25% of Methocel (Sigma Aldrich). For the treated cells the same medium was supplemented with 4 mM 4-NB. The size of the spheroids was monitored up to 14 days by measuring their diameter using ImageJ software.

2.11 Confocal Microscopy

2.11.1 Mitochondrial network and morphology assessment via live cell imaging

For mitochondrial morphology analysis after 48 h, cells were washed with PBS and loaded with 100 nM MitoTracker Green (MTG, 490nm ex.; 516nm em., Thermo Fisher Scientific Scientific) according to Chazotte et al.[53] Images were acquired on a Nikon C1si confocal microscope (Nikon, Tokyo, Japan). Images analysis was performed using Mitochondrial Morphology plugin (ImageJ) according to Dagda et al. [54] Circularity and aspect ratio (the ratio of the width to the height) values were calculated and analysed on GraphPad software.

2.11.2 Mitochondrial potential measurement via JC-1

To assess how CoQ_{10} could alter mitochondrial membrane potential, JC-1 fluorescence assay was performed. In control cells with normal mitochondrial membrane potential, JC-1 accumulates in mitochondria as aggregates with a red fluorescence emission while the monomeric form is prevalent in the cytoplasm with green fluorescence emission. A high $\Delta\Psi m$ JC-1 forms complexes known as J-aggregates, emitting an orange-red fluorescence

2.11.3 BTP complex as a sensor for oxygen

Intracellular oxygen tension was measured in intact cells, using BTP (bis(2-(2′-benzothienyl)-pyridinato49 N,C3′)iridium(acetylacetonate), a fluorescent dye which light emission is quenched by molecular oxygen. [55] Briefly $3x10^3$ cells were seeded in an 8-well microplate (Ibidi). After 24 hours cells were washed with PBS and stained with 5µM of BTP dissolved in DMEM for 4 hours. After staining cells were washed three times with PBS and Images were acquired. For three-dimensional cell culture additional staining of 8 µM of Hoechst, dissolved in PBS, (Sigma Aldrich) for 10 minutes, was used to stain nuclei.

2.11.4 Lysosomes detection

To visualize lysosomes in live cells, 3 10^3 cells were plated in ibiTreat m-Slide 8-Well (Ibidi) in 300 µl of complete medium and incubated at 37°C in a humidified atmosphere with 5% CO2. After 24 h, cells were transfected with a plasmid carrying the green fluorescent protein (GFP) protein targeted to lysosomes, following the manufacturer's instructions (CellLight™ Lysosomes-GFP, BacMam 2.0; Thermo Fisher Scientific). After 48 hours cells were washed and Hoechst (8 um) was added to stain nuclei for 10 minutes. After that cells were washed again with PBS, and cells were visualized using a Nikon C1si confocal microscope (Nikon, Tokyo, Japan).

2.11.5 Measurement of intracellular NADH

NADH autofluorescence measurements were performed following Frezza et al. with minor modifications. [56] Briefly, cells were cultured in 8-well µ-slides (Ibidi) and treated as described above. Images were collected with a Nikon C1si confocal microscope equipped with a UV laser. Images were converted into a 'fire' lookup table (LUT) for visual representation. At least five randomly chosen fields for each condition were analyzed. NAD(P)H quantification was performed using ImageJ software after background subtraction.

2.11.6 Glucose uptake assay using 2-NBDG

The fluorescent glucose analogue 2-[N-(7-nitrobenz-2-oxa-1,3-diazol-4-yl)amino]-2-deoxy-d-glucose (2-NBDG; Thermo Fisher) was used. Cells were seeded in a 15-well plate (Ibidi) and treated as described above. After 30 min of incubation with 100 µM 2-NBDG, images were acquired with a confocal microscope (Nikon C1si). At least five randomly chosen fields (minimum 40 cells) for each condition were analyzed. Fluorescence intensity quantification was performed using IMAGE software.

2.11.7 Phalloidin staining

To visualize cell cytoskeleton, $3x10^3$ cells were plated in ibiTreat m-Slide 8-Well (Ibidi) in 300 µl of complete medium and incubated at 37°C in a humidified atmosphere of 95% air/5% CO2. After 24 hours, cells were washed three times in PBS, therefore permeabilized for 10 min with PBS 1% Triton (Triton X-100; Sigma-Aldrich, Co., St. Louis, MO, USA), then incubated in blocking solution 1× PBS 1% bovine serum albumin (BSA; Sigma-Aldrich, Co., St. Louis, MO, USA) for 30 min. After three washes in 1× PBS, actin was stained using FITC-Phalloidin (1:250; Sigma-Aldrich, Co., St. Louis, MO, USA). Coverslips were mounted after washes in PBS in ProLong Gold Antifade Mountant with 8 µM Hoechst to stain nuclei.

2.11.8 Chromogenic detection of senescence-associated beta-galactosidase (SA-βgal) activity

SA-βGal activity is a biomarker for the identification of senescent cells in culture and mammalian tissues. Senescence-associated beta-galactosidase (SA-βgal) activity was performed following Campisi et al. with minor modifications. [57] Briefly cells were cultured on a cover slip into 6-wells 24 hours before staining at 50% confluence The following day cell were washed twice with PBS, then fixation solution (1% (wt/vol) formaldehyde in PBS) was added and cells were incubated for 5 min at room temperature. After removing fixation solution cells were washed twice with PBS and staining solution 40 mM citric acid/Na phosphate buffer, 5 mM $K_4[Fe(CN)_6]$ $3H_2O$, 5 mM $K_3[Fe(CN)_6]$, 150 mM sodium chloride, 2 mM magnesium chloride and 1 mg ml − X-gal) was added. Then cells were incubated overnight at 37 °C. After that, cells were washed the cells twice with PBS (2 ml per 35 mm dish), and once with methanol (1 ml per 35 mm dish) and then dried. Then images were acquired by bright-field by an inverted microscope (Carl Zeiss AG, Baden-Württemberg, Germany).

2.11.9 Immunofluorescence staining of GLUT1 and GLUT3

GLUT1 and GLUT3 transporters expression was measured by immunofluorescence. MCF7 cells were grown on glass coverslips in a 6-well plate and exposed to 4-NB for 72 h. Then, cells were fixed, permeabilized and incubated with goat polyclonal primary antibodies against Glut1, or Glut3, (Santa Cruz Biotechnology, Dallas, TX, USA), overnight at 4 °C, followed by appropriate anti-goat-FITC secondary antibodies. Specimens have been embedded in Mowiol (Hoechst, Frankfurt, Germany) and multiple images acquired by using sequential laser excitations at 488 nm to reduce spectral bleed-through artefacts. The images have been collected by using a Nikon C1s confocal laser-scanning micro-scope, equipped with a Nikon PlanApo 60X, 1.4-NA oil immersion lens.

2.11.10 Pimonidazole immunofluorescence staining

Pimonidazole staining was performed as described by Sato et al.[58], with minor modifications. Briefly, T67 cells (2.5 × 104) were seeded in a 6-well plate and cultured in the absence or presence of 4 mM 4-NB. After 96 hours, cells were incubated with fresh medium containing 100 µM pimonidazole (Hypoxyprobe #70132-50-3) for 1 h. Cells were then washed twice with PBS and fixed with 3.7% paraformaldehyde at 4 °C overnight. After paraformaldehyde solution was removed and cells were washed twice with 0.9% NaCl, then were permeabilized with 0.9% NaCl and 0.2% Triton at room temperature for 30 min. Permeabilized cells were kept in NaCl 0.9% and 3% BSA for 1 hour and then incubated with monoclonal mouse anti-pimonidazole antibody (1:1000, Hypoxyprobe #Mab-4.3.11.3) for 30 min at room temperature in the dark. Cells were treated with a FITC-conjugated monoclonal antimouse antibody (1:1000) for 2 h at room temperature in the dark. Images were acquired by a confocal microscope (Nikon). Fluorescence quantification was performed using ImageJ and analysed on GraphPad software.

2.12 Assessment of mitochondrial respiratory chain complex activities

The mitochondrial complex I and complex II activities were measured following Spinazzi et al. [59] with minor modifications. Experiments were performed at least in triplicate. Complex IV (cytochrome c oxidase) activity was determined following Barrientos et al. [60]. Briefly, cells were harvested and resuspended in respiratory buffer (RB): 0.3 M mannitol, 10 mM KCl, 5 mM $MgCl_2$, and 10 mM K_2PO_4, pH 7.4. Then, the cell suspension was injected into the polarographic chamber (1.5×10^6 cell/mL) and the reaction was started by adding ascorbate (10 mM) plus N, N, N′, N′-tetramethyl-p-phenylenediamine (TMPD, 0.2 mM). The oxygen consumption rate was recorded for 5 minutes and finally, KCN (700 µM) was added to block complex IV activity. The final respiratory rate is obtained by subtracting the KCN-insensitive respiration. Data were normalized to the cellular protein content determined by the Lowry method[61].

2.13 Western Blot

Cells were lysed in ice-cold 50 mM HEPES (EuroClone), 1 mM EDTA (Sigma-Aldrich), 10% glycerol (Fisher Fisher Scientific), 1% Triton X-100 (Sigma-Aldrich), 150 mM NaCl in the presence of protease inhibitors (Roche, Basel, Switzerland) and phosphatase inhibitors (Inhibition Cocktail 2 and 3, Sigma-Aldrich). Total protein was measured using Bradford protein assay kit (Biorad DC Protein Assay; Biorad, Hercules, CA USA) according to the manufacturer's instruction. Protein samples (70 µg) were subsequently separated on 10% sodium dodecyl sulfate polyacrylamide electrophoresis (SDS PAGE) gels and electro-transferred onto nitrocellulose membranes (Trans-Blot Turbo Transfer System, Biorad). Membranes were blocked in Tris Buffered Saline (TBS) with 1% Casein (Biorad) for 1 hour at RT and were incubated with primary antibodies at 4°C overnight. Membranes were washed three times in Tris-buffered saline containing 0.1% Tween and incubated with peroxidase-conjugated secondary antibodies for 45 minutes at room temperature. The signals were developed using WESTAR Supernova (Cyanagen, Bologna, Italy) and detected with the ChemiDoc™ XRS+ (Biorad).

Densitometric analysis has been performed with ImageLab software (Biorad). Primary antibodies were used against: vinculin (mouse, 1:10000; Sigma-Aldrich), mTOR and GRP75 (goat, 1:500; Santa Cruz, CA USA). Mfn1, Mfn2, and Drp1 (Abnova, 1:1000, Taipei, Taiwan); OPA1 and Hsp60 (BD Biosciences, 1 : 1000, Franklin Lakes, NJ, USA); HIF-1α (iGeneTex, 1 : 2000, Irvine, CA, USA); and actin (Sigma-Aldrich, 1 : 10 000). Peroxidase-conjugated secondary antibodies used were: anti-mouse IgG (1:10,000; Sigma-Aldrich) and anti-rabbit (1:10000; Sigma-Aldrich), anti-goat IgG (1:10000; Dako, Denmark).

2.14 RNA isolation and quantitative PCR (qPCR)

Total RNA was isolated from SH-SY5Y cultures using the RNeasy Mini Kit (Qiagen, Hilden, Germany). cDNA from 1µg of WT, HP and C6, using the SuperScript™ VILO™ cDNA Synthesis Kit (Thermo Fisher Scientific). Quantitative PCR was performed using SYBER Green Supermix (Thermo Fisher Scientific). All samples were run in triplicate on the ABI7500 Fast PCR machine (Thermo Fisher Scientific). Melting curve analysis for each primer pair was carried out to ensure specific amplification. Relative mRNA expression levels of COQ2, SOD1, were normalized to the USF2A gene. Relative mRNA expression levels of HIF-1α were normalized to TATA-box-binding protein (TBP). The statistical significance was calculated using the Δct values[ct (gene of interest) – c t (reference gene)] for each biological replicate in a group and applying Student's t-test [62]

2.15 Cell viability assays.

For cell viability tests, cells were seeded at $5x10^3$ cells per well in a 96-well plate in complete DMEM and complete DMEM plus 4mM 4-NB respectively. Cells were incubated at 37 °C and 5% CO2 for 24 h to allow adhesion. In some experiment to test the effect of tert-butyl 4 hydroperoxide (TBH) exposure, the complete culture medium was replaced with culture medium plus 100µM TBH. Cell viability was measured after 2 h, 4 h, and 8 h respectively by MTT assay. Accordingly, to test the effect

of glycolysis inhibition 10 mM hexokinase 2-deoxyglucose (2-DG), a hexokinase (HK) inhibitor, was used. Cell viability was measured at 24 h, 48 h, and 72h after addition 8 of 2-DG by MTT assay. To test the energetic reliance of cells on oxidative phosphorylation, the complete culture medium was replaced with glucose-free DMEM supplemented with 10% dialyzed FBS and 5.5mM galactose. To test the reliance on glutamine supplementation, the complete culture medium was replaced by glutamine-free DMEM and 10% dialyzed FBS. Cell viability was assessed up to hours of treatment by MTT assay

2.16 BTP calibration

For BTP calibration, T67 cells were cultured, treated with 4-NB, and incubated with the BTP probe as described above. The fluorescence emission (λex 490 nm, λem 610 nm) of BTP-loaded T67 cells, in PBS supplemented with 10 mM glucose, was titrated in a sealed cuvette at different oxygen saturation levels, at 30 °C, using a Jasco FP-777 fluorometer equipped with stirring device. To quantitatively remove oxygen from the buffer, different dithionite ($Na_2S_2O_4$) concentrations were used, previously determined in the same conditions by using a Clark-type electrode.[63 64 65]

2.17 ROS quantification

2.17.1 MitoSOX

Mitochondrial superoxide production was measured using MitoSOX Red (Molecular Probes, Thermo Fisher Scientific) following manufacturer instructions with minor modifications. Briefly, cells were seeded in 96-well plates (OptiPlate black, Perkin Elmer) at 10x103 cells/well and incubated overnight to allow adhesion. After this time, cells were washed with HBSS (Hank's balanced salt solution) and treated with 5 µM Mitosox red dissolved in HBSS with calcium and magnesium for 30 minutes. After this time cells were washed three times with warm HBSS/Ca/Mg and the fluorescence emission from each well was measured (λexc = 510 nm; λem = 580 nm) with a multi-plate reader (Enspire,

PerkinElmer). Data are reported as the mean ± standard deviation of at least six independent experiments.

2.17.2 DCFDA

Cell lines were seeded at $5x10^3$ cells/well in a 96-wells (OptiPlate Black; Perkin Elmer, Inc. Shelton, CT, USA). and incubated for 16 hours. Cells were treated with 10 µM DCFDA dissolved in medium for 1 hour. Finally, cells were washed with PBS and the fluorescence emission from each well was measured (λexc = 485 nm; λem = 535 nm) with a multi-plate reader (Enspire, Perkin Elmer, Waltham, MA USA). Data are reported as the mean ± standard deviation of at least three independent experiments.

2.17.3 Amplex Red

Cells were cultured and treated as above in 96-well plates (OptiPlate Black; Perkin Elmer). For Amplex Red staining, Mohanty et al. protocol was used with minor modifications.[66] After 24 hours cells were washed with Hank's balanced salt solution (HBSS) and treated with 5 µM Amplex Red reagent (10-acetyl-3,7-dihydroxyphenoxazine) (Thermo Fisher) in HBSS supplemented with calcium and magnesium for 30 min. After 15 minutes cells were washed three times with warm HBSS/Ca/Mg, and the fluorescence emission from each well was measured (λex = 571 nm; λem = 585 nm) with a multi-plate reader (EnSpire; PerkinElmer). Data were normalized on protein content.

2.17.4 Bodipy

$5x10^3$ cells per well were seeded into an 8-well plate (Ibidi). After 24 hours cells were washed with HBSS. Cells were then labelled in 1 ml HBSS containing 5 µM BODIPY 581/591 C11 (Thermo Fisher Scientific) and incubated at 37 °C for 10 min. Staining solution was removed and fresh HBSS was added to the cells. Confocal imaging of BODIPY 581/591 C11 was performed as previously described on two independent biological replicates per treatment. Red and green fluorescence values were

quantified using ImageJ, correcting for background by subtracting the red or green fluorescence in cell-free areas. The BODIPY 581/591 C11 fluorescence emission was calculated as the ratio of the green fluorescence (indicating oxidized probe) to total (green + red, which indicates total reduced plus oxidized probe) fluorescence.

2.18 Cell cycle analysis

Cells were seeded in T25 flasks at a density of 1x10 ^{6} cells in complete medium or complete medium supplemented with 4 mM 4-NB respectively for four days. After this time, cells were detached with 0.11% trypsin, washed in PBS, and centrifuged. The pellet was suspended in 0.01% Nonidet P-40, 10 µg/mL RNase, 0.1% sodium 40 citrate, and 50 µg/mL propidium iodide (PI) for 30 min at room temperature in the dark. PI fluorescence was analyzed using a Beckman Coulter Epics XL-MCL flow cytometer, and cell analysis was performed using the M cycle (Verity) and MODFIT 5.0 software.

2.18.1 Measurement of membrane fluidity

Electron paramagnetic resonance spectra were recorded in intact T67 cells spin-labeled with 1-palmitoyl-2-stearoyl-(5-doxyl)-sn-glycero-3-phosphocholine (5DPC). A thin film of 5DPC was formed on the bottom of a vial from the complete evaporation of 1.5 µL of lipid stock in chloroform (2.9 mM); 2 mL cell suspension (5×10^6 cells mL^{-1} of PBS) was added and gently stirred to incorporate the lipids. Samples were transferred to an EPR glass capillary after an incubation time of approximately 20 min. EPR experiments were performed using a Bruker ESP380 spectrometer, (Bruker Corporation, Billerica, MA, USA) operating at X-band (~ 9.5 GHz), equipped with an SHQ cavity. The microwave frequency was measured by a frequency counter, HP5342A. All spectra were obtained using the following parameters: modulation amplitude 0.2 mT; modulation frequency 100 kHz; time constant 10 ms; conversion time 42 ms; scan width 1.5 mT; 1024 points; temperature 298 K; microwave power 4.7 mW; and 45 scans. The order parameter of 5DPC, S5DPC, can be used to evaluate the fluidity of the cell membrane: A low order parameter implies that the spin label is free to move and therefore

can be related to higher membrane fluidity; S5DPC can be computed from the spectra according to the formula reported by Gaffney. [67]

2.19 Measurement of plasma membrane NAD(P)HFeCN and NAD(P)H oxidase (PMOR) activities

Cells were cultured in Petri dishes and treated as described above. After detachment by trypsin, cells were carefully washed with PBS and pelleted at 300 g for 3 min was performed following Lenaz et al. [68] protocol with minor modifications was followed for determination of NAD(P)H FeCN activity Briefly, intact cells were incubated for 10 min at 37 °C in PBS containing 5 mM glucose, 1 mM pyruvate, 2 µM rotenone, 2 µM antimycin A, 4 µM dicumarol, and 2 mM KCN. The reaction started by adding 250 µM of potassium hexacyanoferrate(II) trihydrate (FeCN). FeCN reduction was followed spectrophotometrically (λ = 420nm) for 4 min using a Jasco V- 550 equipped with cuvette stirring device and thermostatic control. The absorption extinction coefficient used to calculate the rate of FeCN reduction was 1 $mM^{-1}cm^{-1}$. The activity was normalized on protein content. Determination of oxygen consumption by PMOR system in intact T67 cells was performed using a thermostatically controlled oxygraph chamber (Instech Mod. 203) at 30 °C in PBS buffer containing 5 mM glucose, 1 mM pyruvate, 2 µM rotenone, and 2 mM KCN. The specific PMOR-O2 activity was obtained by inhibiting the enzyme with 2 µM DPI.

2.20 Statistical analysis

Statistical analysis and significance for each experiment were analyzed using Prism 8 software (GraphPad, San Diego, CA, USA). All experiments were carried out in three independent experiments, whose number (n) is indicated in each figure legend. Results are expressed as the mean ± SEM. For comparison between multiple groups, analysis of variance (ANOVA) was used followed by Tukey's post hoc test. Error bars indicate standard deviation (SD) or standard error of the mean (SEM). *P ≤ 0.05; **P ≤ 0.01; ***P ≤ 0.001; ****P ≤ 0.0001.

3 RESULTS

3.1 Coenzyme Q biosynthesis induces HIF-1α stabilization and metabolic switch toward glycolysis in T-67 cell

3.1.1 4-NB treatment affects mitochondrial functions

In this study, we used the T67 human glioma cell line treated with 4-nitrobenzoate (4-NB), a competitive inhibitor of coq2. Coq2 is a prenyltransferase involved in CoQ_{10} biosynthesis at the mitochondrial level, previously described in section 2.5.5.

T67 cells cultured for four days in the presence of 4 mM 4-NB displayed a 50% decrease in CoQ content (Fig. 6A) and a mild (10%) decrease in proliferation rate in comparison with untreated cells (control) (Fig. 6B). To assess a possible recovery with Q10 supplementation, we have cotreated cells with 4-NB and a water-soluble CoQ formulation. Q ter supplementation increased the ubiquinone content above control levels and restored the cell growth rate (Fig.6A, B). To evaluate the effect of CoQ depletion on the OxPhos activities, we measured the oxygen consumption rate (OCR) in intact cells in the presence of glucose (endogenous respiration) and after the addition of FCCP (uncoupled respiration). The 4-NB-treated cells exhibited a strong OCR decrease in both endogenous respiration and uncoupled respiration (Fig. 6C) which was mirrored by a significant reduction in the energy charge value (Fig. 6D). The co-treatment with 4-NB and Q partially recovered the uncoupled respiration rates and completely rescued the energy charge values. Despite an OxPhos impairment, the 4-NB treatment caused a slight elevation of the mitochondrial membrane potential (ΔΨm), measured staining cells with tetramethylrhodamine methyl ester (TMRM) and MitoTracker Green (MTG) and calculated TMRM/MTG ratio (Fig. 6E). Moreover, the TMRM fluorescence of 4-NB-treated cells was unaffected by oligomycin A addition and less sensitive to FCCP stimulation than untreated cells (Fig. 6F). The occurrence of decreased OxPhos activity associated with CoQ depletion was further

confirmed by the low Δ-lactate value found in 4-NB-treated cells, which was also not rescued by exogenous CoQ (Fig. 6G).

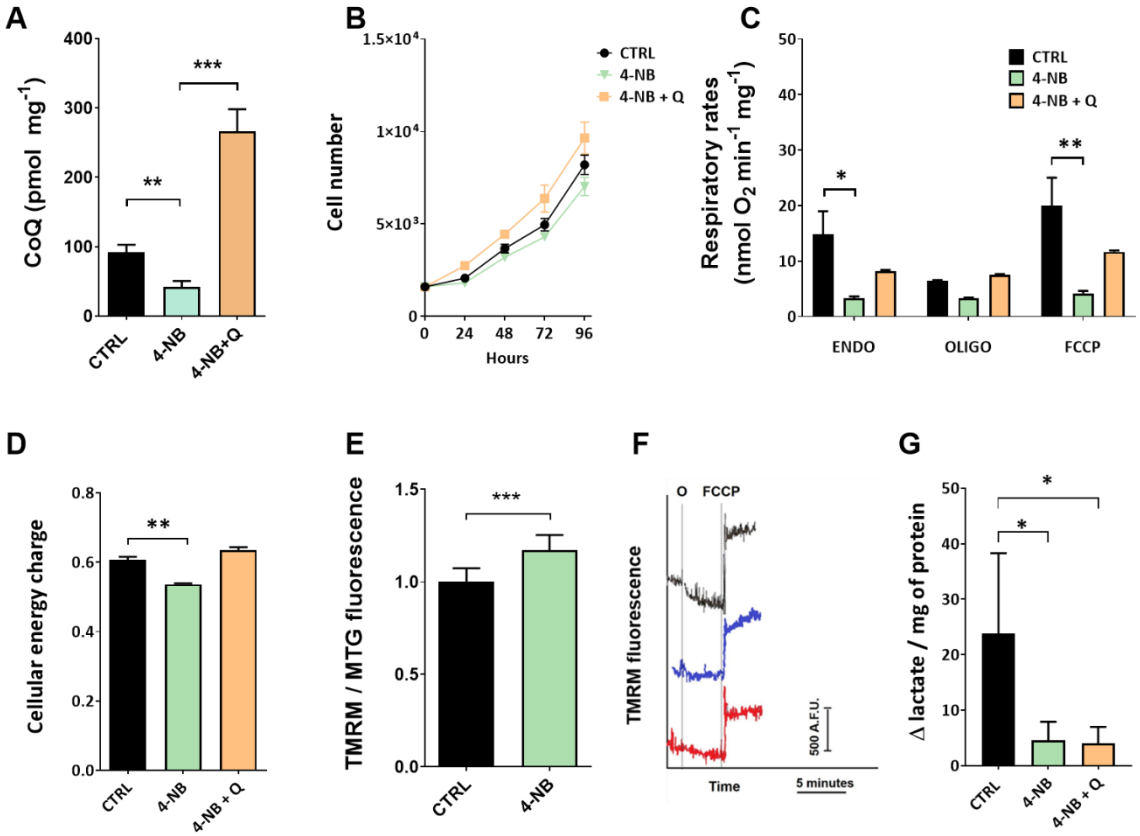

Figure 6 (**A**) Cellular CoQ content quantification by HPLC, normalized on protein content (n = 4). (**B**) Viability of control, 4-NB, and 4-NB + Q-treated cells (n = 3). (**C**) OCR measured in DMEM (endogenous respiration), in the presence of oligomycin A (Olig) and carbonyl cyanide 4-(trifluoromethoxy) phenylhydrazone (FCCP) (n = 4). (**D**) Cellular energy charge quantification (n = 3). (**E**) ΔΨm determination in control and 4-NB-treated cells co-stained with TMRM and MTG. Data are expressed as the TMRM/MTG ratio (n = 3). (**F**) TMRM fluorescence emission in intact T67 cells, following the addition of oligomycin A (O) and FCCP. CTRL, 4-NB, and 4-NB + Q traces are shown in black, red, and blue, respectively. Representative traces of TOT experiments are shown. (**G**) The extracellular lactate was measured at time 0 and after 6 h of treatment with oligomycin A. Data are presented as Δ-lactate values, that is, the difference in lactate peak area between 6 h and time 0, normalized on cellular protein content (n = 3). Error bars indicate SEM. For comparison between multiple groups, analysis of variance (ANOVA) was used followed by Tukey's post hoc test. *P ≤ 0.05; **P ≤ 0.01; ***P ≤ 0.001.

3.1.2 Mitochondrial morphology alteration

It has been extensively described how an impaired OxPhos function can deeply perturb the mitochondrial network morphology. To address this point we investigate mitochondrial network, staining cells with MTG. Control cells exhibited a highly interconnected mitochondrial network, which became swollen and fragmented after treatment with 4-NB. When cells were co-treated with 4-NB

and Q, the interconnectivity was improved, but round shaped structures were present, indicating the persistence of dramatic alterations in the fusion process. Since morphological transitions are regulated by dynamic processes of membrane fusion and fission[69], we evaluated a possible change in the levels of the mitochondrial shaping proteins. To answer this question we performed WB the analyse the expression of Mfn1, Mfn-2 and OPA1, responsible for the fusion at the mitochondrial outer and inner membranes, respectively, and DRP1, involved in the fission process.

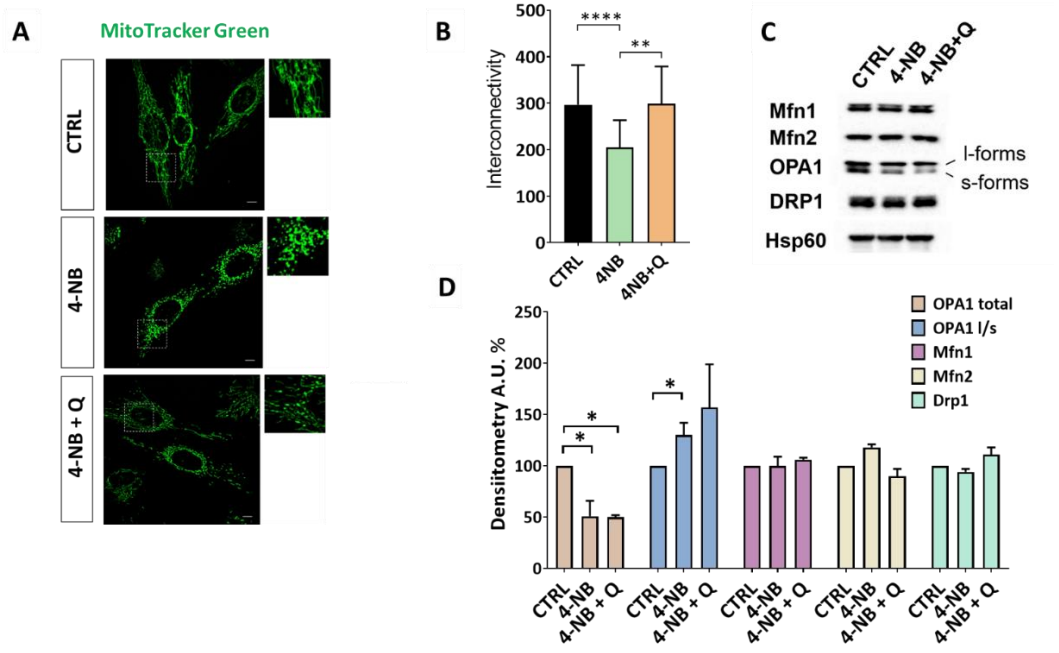

Figure 7 (**A**) Representative images of live T67 cells cultured in the presence of vehicle (CTRL), 4-NB, and 4-NB + CoQ (4-NB + Q), as described previously, and stained with MTG (size bar = 10 µm, n = 3). (**B**) Quantification of mitochondrial interconnectivity performed using ImageJ tools. For each condition, at least two randomly chosen fields were analyzed. (**C**) Mfn1, Mfn2, OPA1, and DRP1 levels determined by western blot analysis in lysates from T67 cell treated as above. (**D**) Quantification of proteins level was performed by densitometry analysis, using Hsp60 as a loading control. Error bars indicate SD. For comparison between multiple groups, analysis of variance (ANOVA) was used followed by Tukey's post hoc test. *P ≤ 0.05; **P ≤ 0.01; ****P ≤ 0.0001

Figure 7C reports a representative western blot obtained in cell lysates, showing that the content of Mfn1, Mfn-2, and DRP1 was similar in control cells and after treatment with 4-NB and 4-NB plus CoQ. Conversely, we found a significant decrease in OPA1 levels when cells were treated with 4-NB, regardless of the CoQ treatment. In particular, control cells showed two bands corresponding to the OPA1 long and short forms, whereas the OPA1 short form band was significantly reduced by 4-NB

treatment. Densitometry analysis reported in Fig. 2D revealed a 50% reduction in total OPA1 content and an increased long/short OPA1 ratio in 4-NB-treated cells in comparison with controls. In agreement with the small recovery observed in the network morphology, the co-treatment of 4-NB with exogenous CoQ failed to rescue the OPA1 alteration. These results suggest that the increased mitochondrial network fragmentation induced by 4-NB is associated with perturbation of the OPA1 long/short form balance.

3.1.3 Cholesterol content affects plasma membrane fluidity

Since CoQ share part of biosynthetic pathway, we hypothesised that mitochondrial prenyltransferase coq2 inhibition could make FPP more available for squalene synthase, and consequently increase cellular cholesterol content. By using two different methods, gas chromatography mass spectrometry (GC-MS) (Fig. 8A,B) and high-performance liquid chromatography (HPLC) analysis, data have shown that cells treated with 4- NB, presented a significant increase in cholesterol content, which was reduced by a short treatment with cyclodextrins (CDs) (Fig. 8C). The co-treatment with 4-NB and water-soluble CoQ formulation reduced the cholesterol content toward control levels (Fig. 8A,C). The correlated CoQ depletion and cholesterol increase perturbed the plasma membrane fluidity, as demonstrated by the TMA-DPH fluorescent anisotropy measurement (Fig. 8D) and by the increased value of the order parameter S in comparison with controls (S4-NB/SCTRL = 1.12), calculated from 5-doxyl-PC EPR spectra (Fig. 8E).

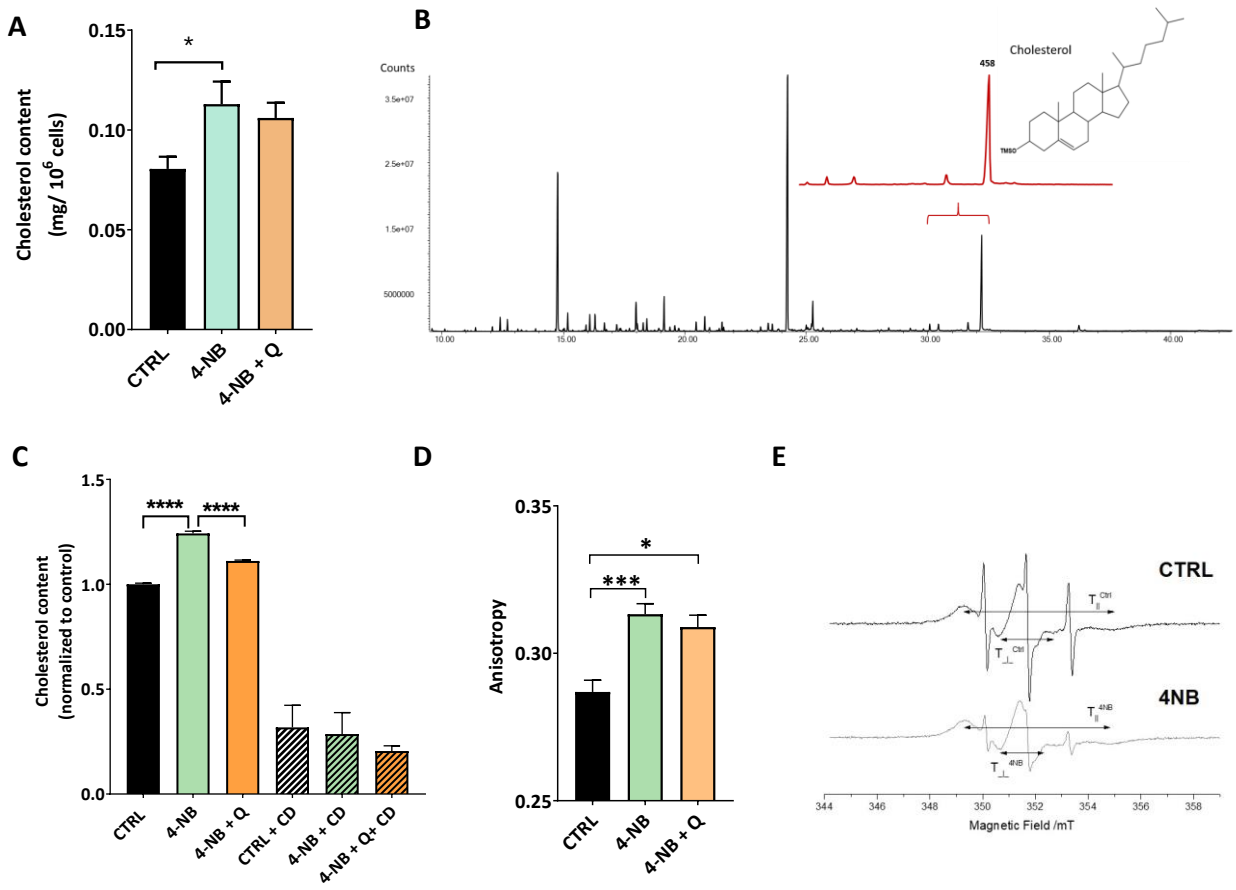

Figure 8 (**A**) Total cholesterol quantification by GC-MS analysis in lysates of T67 cells cultured in the presence of vehicle (CTRL), 4-NB, and 4-NB + CoQ (4-NB + Q), as described in Fig. 1 (n = 3). (**B**) Representative spectrum of GC-MS of cholesterol (**C**) Total cholesterol content assessed by HPLC in lysates of T67 cells treated as above. The total cholesterol determination was performed in the absence and presence of cyclodextrin (CD) treatment (see Materials and methods section for details) (n = 4). **(D**) Plasma membrane steady-state anisotropy was quantified in live T67 cells by using 1-(4-trimethylammoniumphenyl)- 6-phenyl-1,3,5-hexatriene p-toluenesulfonate (TMA-DPH). Error bars indicate SEM (n = 5). (**E**) Representative EPR spectra of T67 cells using 5-doxyl-PC (1-palmitoyl-2-stearoyl-(5-doxyl)-snglycero- 3-phosphocholine) probe. For comparison between multiple groups, analysis of variance (ANOVA) was used followed by Tukey's post hoc test. *P ≤ 0.05; ***P ≤ 0.01; ****P ≤ 0.0001

3.1.4 HIF-1α stabilization

HIF-1α has been recognized as a major key regulator of metabolism under many circumstances. Specifically, it has been reported how increased cholesterol level could upregulate HIF-1α expression content [70]. Therefore, we decided to evaluate the effect of 4-NB on the protein levels of HIF-1α. Western blot analysis revealed that HIF-1α content was higher in 4-NB-treated cells in comparison

with controls, whereas co-treatment with 4-NB and Q reduced the HIF-1α level (Fig. 9A). Quantitative analysis of bands intensity over actin is reported in Fig. 9C, D.

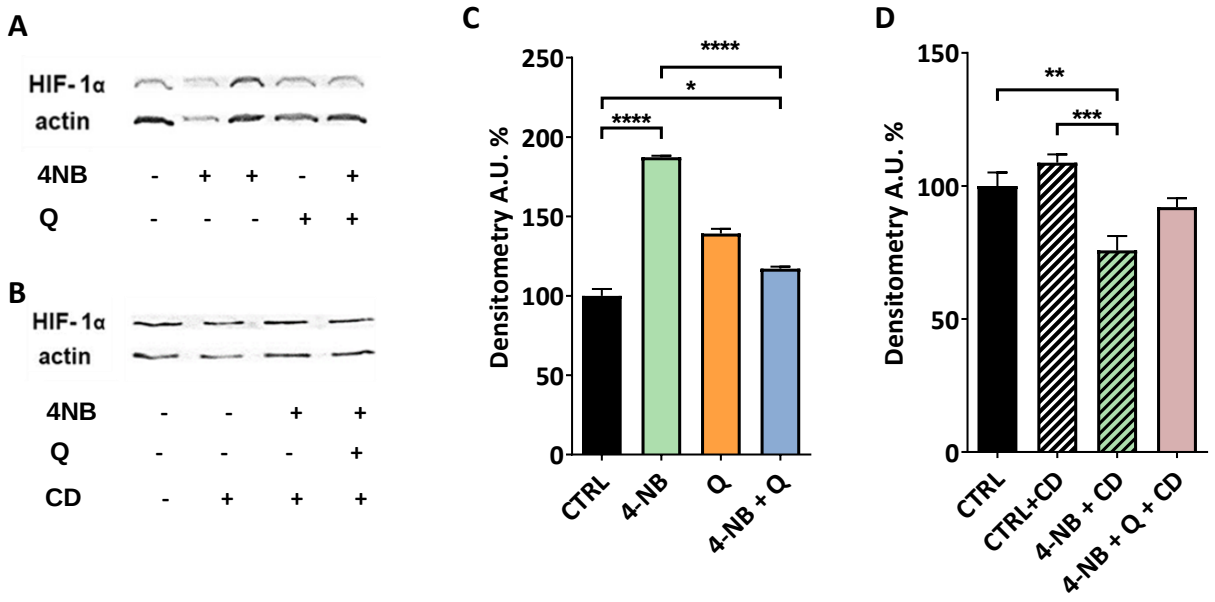

Figure 9 (**A**) HIF-1α protein level was determined by western blot analysis in lysates from T67cells incubated in the presence of vehicle (CTRL), 4-NB, and 4-NB + CoQ (4-NB + Q) (n = 3). (**B**) HIF-1α level was measured in lysates of cells incubated in the absence and presence of cyclodextrin (CD) (n = 3). (**C, D**) Quantification of HIF- 1α protein levels was performed by densitometry analysis, using actin as a protein loading control. Error bars indicate SEM. Data are expressed as mean SD (n = 3). For comparison between multiple groups, analysis of variance (ANOVA) was used followed by Tukey's post hoc test. *P ≤ 0.05; **P ≤ 0.01; ***P ≤ 0.001; ****P ≤ 0.0001. Data are expressed as mean SD (n = 3). For comparison between multiple groups, analysis of variance (ANOVA) was used followed by Tukey's post hoc test. *P ≤ 0.05; **P ≤ 0.01; ***P ≤ 0.001; ****P ≤ 0.0001.

Given that the expression of HIF-1α can be subjected to transcriptional/translation regulation, we determined whether the HIF-1α mRNA expression was increased in 4-NB-treated cells by qRT–PCR analysis. However, we failed to detect any difference, as reported in Fig. 10, suggesting that HIF-1α accumulation is mainly due to a post-transcriptional stabilization. Of interest is that depletion of membrane cholesterol through CD treatment decreased the level of HIF-1α in cells treated with 4-NB, suggesting its dependence on cholesterol-dependent plasma membrane feature perturbation (Fig. 9B, D). It is commonly known that HIF-1α stabilization leads to stimulation of the glycolytic pathway as a metabolic adaptation mechanism [71] [72] that could counteract the detrimental effects of mitochondrial dysfunction caused by CoQ depletion.

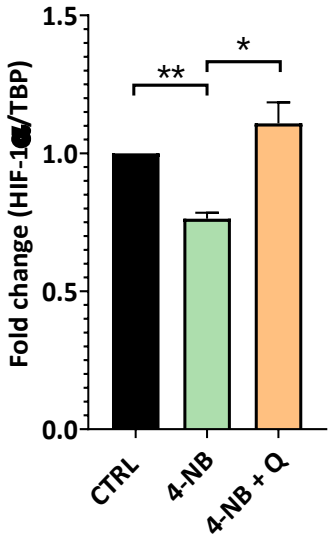

Figure 10 HIF-1α expression level was evaluated by real-time quantitative PCR in T67 cells treated as above. The normalization was performed using TBP. Data are expressed as mean SD (n = 3). For comparison between multiple groups, analysis of variance (ANOVA) was used followed by Tukey's post hoc test. *P ≤ 0.05; **P ≤ 0.01; ***P ≤ 0.001; ****P ≤ 0.0001.

3.1.5 A switch from oxidative metabolism towards glycolysis

Aiming to assess if 4-NB treatments lead to a glycolytic phenotype, we determined the uptake of the fluorescent glucose analogue 2-NBDG, showing a marked increase in CoQ-depleted cells compared with controls. The co-treatment with 4- NB and Q reduced the glucose uptake to values similar to untreated cells (Fig. 11B). The extracellular lactate production was also determined. Lactate content was weakly increased by 4-NB treatment, being not completely rescued by Q treatment (Fig. 11A).

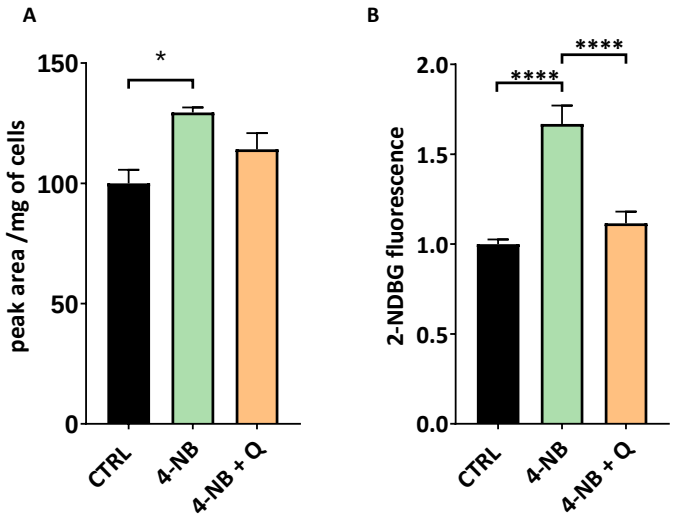

Figure 11 (**A**) Extracellular lactate quantification by HPLC method in live T67 cells (n =5). (**B**).Quantification of 2-deoxy-2-[(7-nitro-2,1,3-benzoxadiazol-4-yl)amino]-D-glucose (2-NDBG) fluorescence in live T67 cells (n = 5). Error bars indicate SEM. For comparison between multiple groups, analysis of variance (ANOVA) was used followed by Tukey's post hoc test. *P ≤ 0.05; **P ≤ 0.01; ****P ≤ 0.0001

We then determined the NADH content, which was significantly increased in 4-NB-treated cells in comparison with controls. Co-treatment with 4-NB and Q restored the levels of NAD(P)H to control levels (Fig. 12A, B).

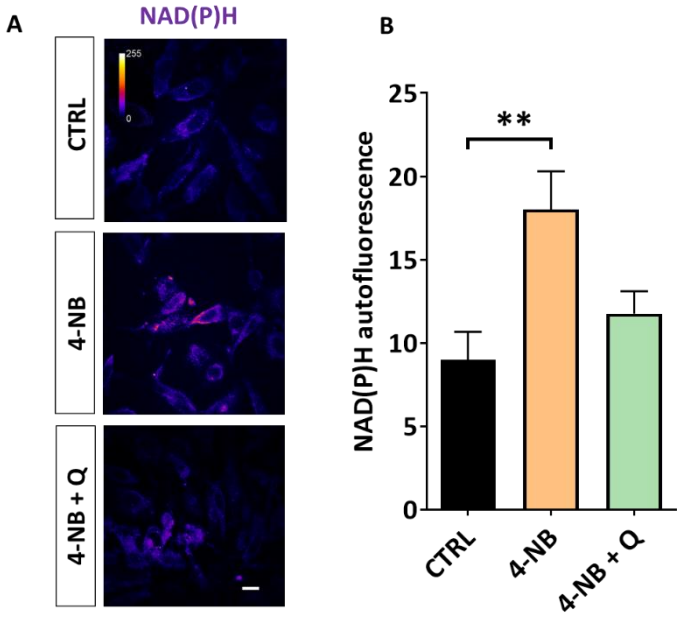

Figure 12 (**A**) Representative images od NADH autoflorescence. Images were converted into a 'fire' lookup table (LUT) for visual representation (scale bars: 10 µm, n = 3) (**B**) NAD(P)H autofluorescence quantification in live T67 cells (n = 3).

For each condition, at least three randomly chosen fields were observed in three independent experiments. Error bars indicate SEM. For comparison between multiple groups, analysis of variance (ANOVA) was used followed by Tukey's post hoc test. **P ≤ 0.01.

The cytosolic NAD+/NADH homeostasis relies on the activity of the lactate dehydrogenase and also of the plasma membrane oxidoreductase (PMOR), a small electron transport chain located in the plasma membrane, comprising two enzymes functionally connected by CoQ: a NAD(P)H dehydrogenase and a CoQ oxidase. In cells with mitochondrial impairment, this inducible enzyme acts to release the cytosolic reducing power by the NAD(P)H dehydrogenase activity which transfers electrons to CoQ and then to the terminal oxidase. The NAD(P)H dehydrogenase activity was assayed using ferricyanide (FeCN) as an exogenous electron acceptor. Since the cytosolic NAD(P)H concentration is always saturating, NAD(P)H-FeCN activity is considered as a measure of the amount of the enzyme. In 4-NB-treated cells, the NADH: FeCN activity was more than threefold higher compared with controls and was reduced after co-treatment with CoQ (Fig. 13A). This finding indicates increased expression of the dehydrogenase part of the PMOR system, which correlates with mitochondrial impairment. Furthermore, the overall PMOR activity, measured as diphenylene iodonium (DPI)-sensitive oxygen consumption in intact cells, was significantly higher in 4-NB-treated cells compared with control (Fig. 13B). In this context, supplementation with CoQ formulation improved the PMOR activity of 4-NB-treated cells (Fig. 13B). On the other hand, the CoQ depletion likely reduces the catalytic efficiency of the PMOR system. The ratio between PMOR oxidase and NADH-FeCN activity, which can be considered indicative of the enzyme efficiency, was 0.053 for controls, 0.028 for 4-NB, and 0.083 for 4-NB + Q-treated cells, highlighting the stimulating effect of CoQ in the PMOR electron transfer mechanism.

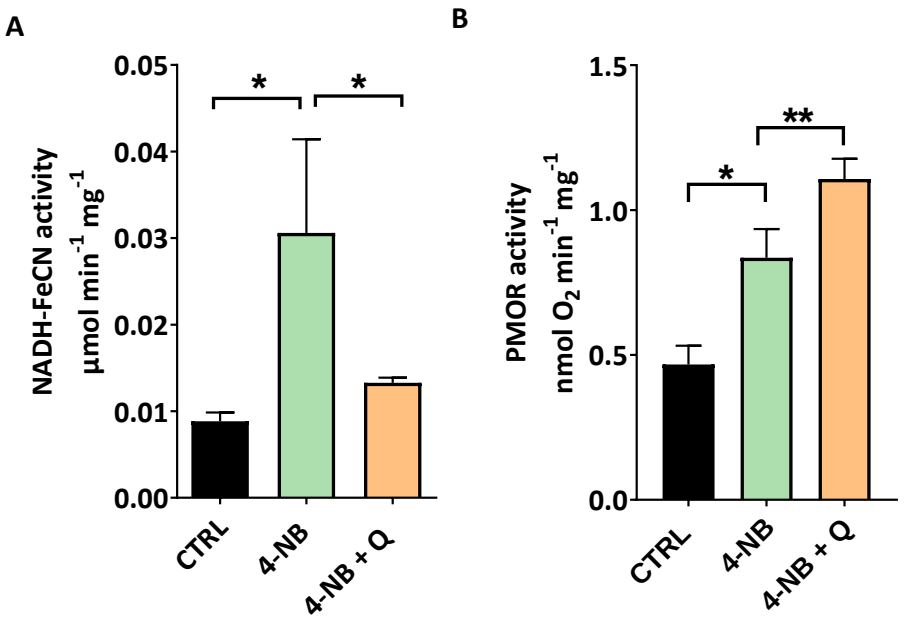

Figure 13 (A) NAD(P)H-FeCN oxidoreductase activity in T67 cells treated as above (n = 3). (**B**) Plasma membrane NADH oxidoreductase (PMOR) activity in T67 cells treated as above (n = 3). Error bars indicate _ SEM. For comparison between multiple groups, analysis of variance (ANOVA) was used followed by Tukey's post hoc test. *P ≤ 0.05; **P ≤ 0.01; ****P ≤ 0.0001.

The increased activity of the PMOR significantly contributes to sustaining the metabolic switch toward the glycolytic pathway by lowering the intracellular reducing power, preserving the cell viability under conditions of mitochondrial energetic failure. We have shown above (Fig. 6F) that ΔΨm measured in intact cells treated with 4-NB was insensitive to oligomycin A and less sensitive to FCCP compared with control cells; moreover, co-treatment with Q was unable to restore the response to these two compounds. Conversely, as reported in Fig. 14, the traces of TMRM fluorescence obtained in digitonin-permeabilized cells were comparable, being controls and 4-NB-treated cells equally sensitive to oligomycin A and FCCP. It has to be noticed that digitonin binds and solubilizes the free cholesterol of the plasma membrane, thus reducing its content. This finding suggests a close dependence of mitochondrial energetic function on cholesterol content increased.

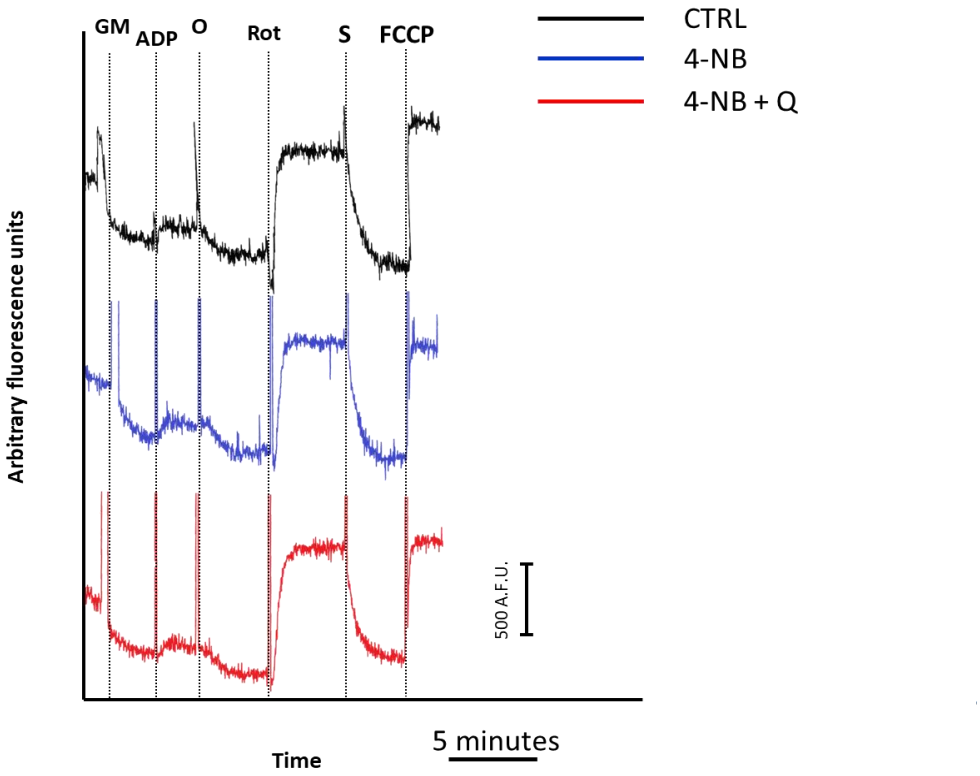

Figure 14 Representative traces of TMRM fluorescence of digitonin-permeabilized T67 cells following addition of glutamate/malate (GM), adenosine-50-diphosphate (ADP), oligomycin A (O), rotenone (R), succinate (S), and carbonyl cyanide 4-(trifluoromethoxy) phenylhydrazone (FCCP).

Considering that HIF-1α stabilization also promotes lipid anabolism, we estimated the intracellular accumulation of lipid droplets by incubation with the fluorescent probe Nile Red. Figure 15 shows that the Nile Red-stained spots were more abundant in 4-NB-treated cells, whereas they were present to a lower extent in control cells and cells co-treated with 4-NB and Q.

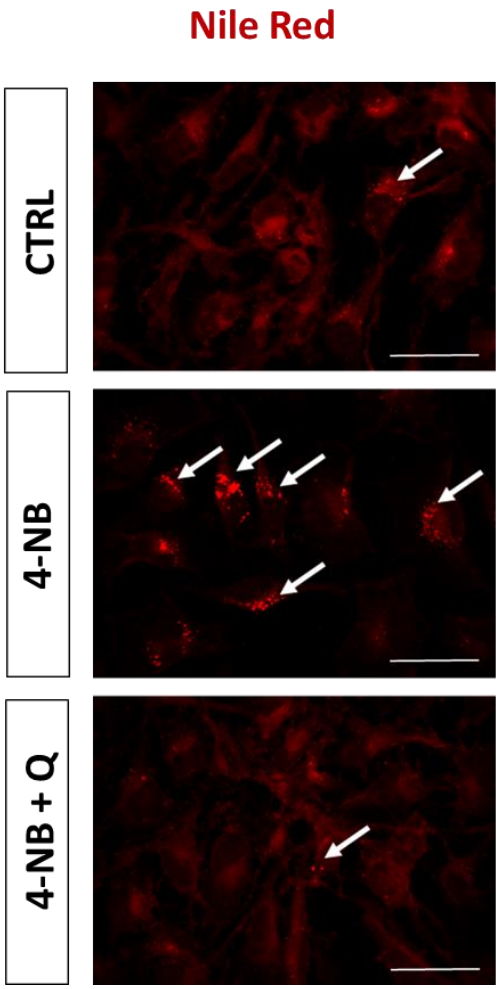

Figure 15 Representatives images of T67 cells stained with Nile red. White arrows indicate Nile red spots. (Size bar = 10 µm).

3.1.6 Increased oxidative stress and partial reduction of intracellular oxygen

We hypothesized that an increased cholesterol content, perturbating the physicochemical properties of the plasma membrane, could cause diminished oxygen membrane permeability thus prompting HIF-1α stabilization.

To investigate this aspect, we first used pimonidazole, which undergoes a reduction in hypoxic cells forming adducts with thiol groups in proteins, peptides, and amino acids in cultured cells. Immunofluorescence detection indeed indicated a higher content of pimonidazole hypoxic adducts in 4-NB-treated cells compared with controls (Fig. 16A, B)

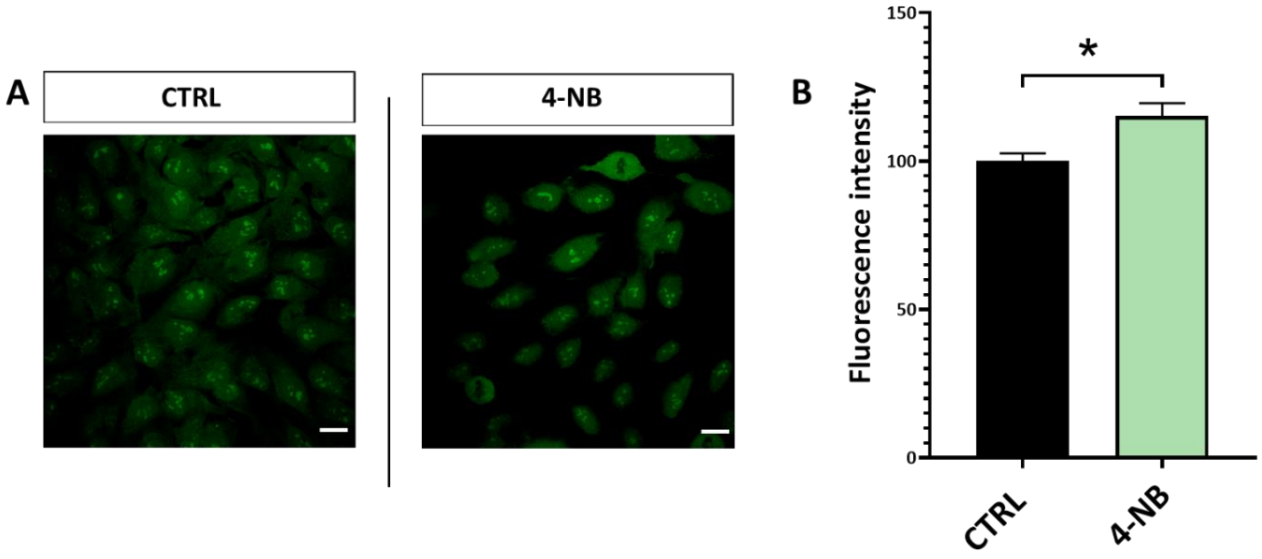

Figure 16 (**A**) Representative images of pimonidazole-stained T67 cells treated without or with 4-NB (scale bars: 10 µm, n = 3). (**B**) Pimonidazole fluorescence intensity quantification. Data are expressed as mean SD (n = 3). Error bars indicate SEM. For comparison between multiple groups, analysis of variance (ANOVA) was used followed by Tukey's post hoc test. *P ≤ 0.05.

To quantify this reduction in intracellular oxygen, we utilized the fluorescent iridium (III) complex probe (BTP) as a live-cell oxygen sensor. Figure 17A shows that T67 cells treated with 4-NB exhibited a higher BTP signal compared with untreated cells, suggesting the occurrence of a reduction in endogenous oxygen. The BTP signal calibration, as a function of oxygen concentration, let us to better estimate an extent of reduction, approximately 50% in cells treated with 4-NB compared with controls (Fig. 17B, C). This oxygen saturation reduction will not be enough to block completely prolyl hydroxylase (PDH)-dependent HIF-1α hydroxylation; nevertheless, it might be enough to reduce it.

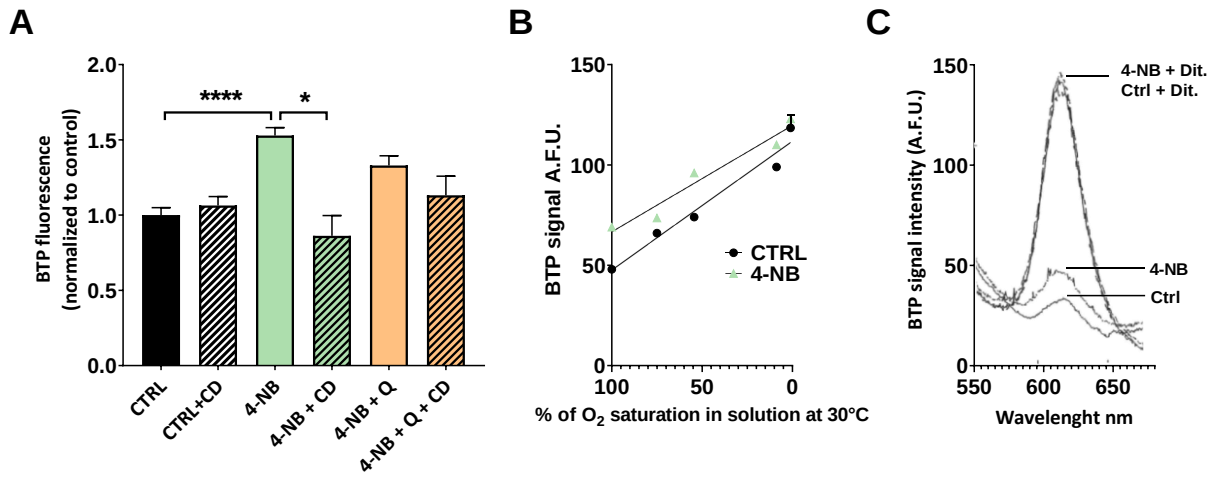

Figure 17 (**A**) Intracellular oxygen was determined in live T67 cells by using the fluorescent probe bis(2-(20-benzothienyl)-pyridinato-N, C 30) iridium (acetylacetonate) (BTP), in the absence and presence of cyclodextrin (CD) treatment (n = 5). Data were normalized on protein content. (**B**) Calibration of BTP fluorescence emission recorded in T67 cells, cultured and treated as above, at different percentages of oxygen saturation in solution at 30 °C. Oxygen was removed from the solution by adding different amounts of dithionite (Dit), as described in the Materials and methods section. Each point is the average of two independent determinations. (**C**) Representative fluorescence traces of T67 cells in 100% oxygen saturated solution (Ctrl, 4-NB) and in 1% oxygen saturated solution (Ctrl + Dit, 4-NB + Dit) (n = 3). Error bars indicate SEM. For comparison between multiple groups, analysis of variance (ANOVA) was used followed by Tukey's post hoc test. *P ≤ 0.05; **P ≤ 0.01; ***P ≤ 0.001; ****P ≤ 0.0001.

HIF-1α stabilization could be induced by increased oxidative stress too. [73] To evaluate this point, we employed two specific fluorescent probes for ROS detection: DCFDA, for intracellular reactive oxygen species measurement and Mito-SOX Red, which selectively targets mitochondria and is oxidized by superoxide anion. Furthermore, we stained the cells with the probe DAF-FM, which becomes fluorescent when coupled with nitric oxide (NO). Cells treated with 4-NB showed higher cellular and mitochondrial oxidative stress, as demonstrated by the increased DCF (Fig.18A) and MitoSOX Red signals (Fig. 18B), as well as a significant elevation of NO levels (Fig. 18C) in comparison with controls. The co-treatment with 4-NB and CoQ restored the superoxide and hydrogen peroxide levels to control values but did not prevent 4-NB-mediated NO production. These results suggest that coq2 inhibition is associated with the occurrence of an oxidative stress, possibly involved in HIF-1α stabilization, in combination with partial reduction in intracellular oxygen.

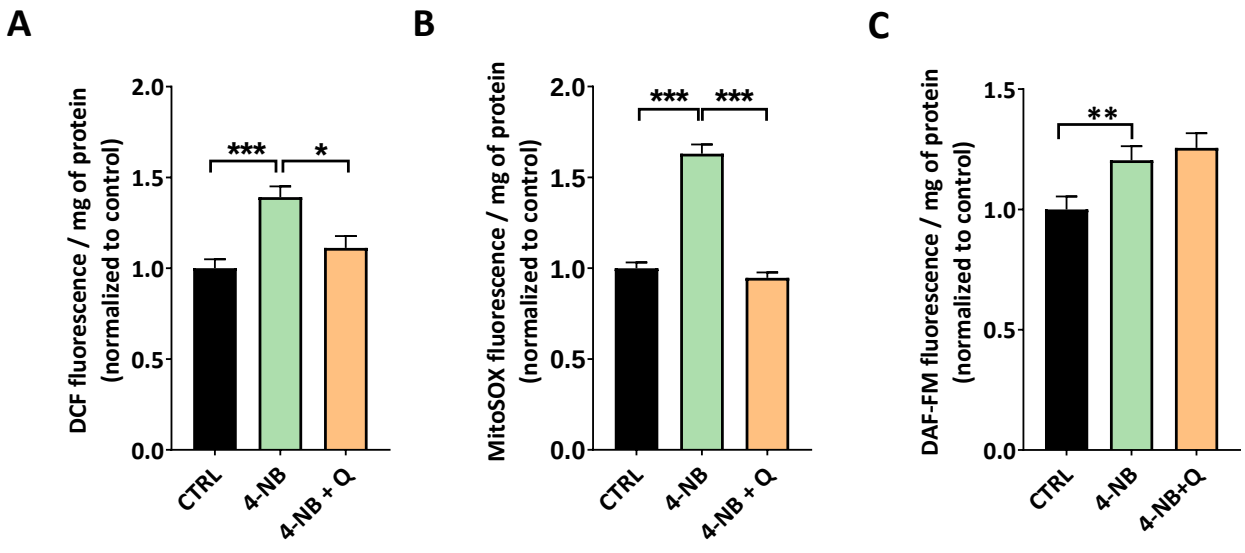

Figure 18 (**A**) ROS production in live T67 cells treated as above was assessed by using dichlorofluorescin diacetate (DCFDA) (n = 4); (**B**) mitochondrial superoxide production by using the mitochondrial specific probe MitoSOX Red (n = 4) and (**C**) nitric oxide production by using 4-amino-5-methylamino-20,70- difluorescein (DAF-FM) (n = 4). Oxidative stress data were normalized on protein content. Error bars indicate SEM. For comparison between multiple groups, analysis of variance (ANOVA) was used followed by Tukey's post hoc test. *P ≤ 0.05; **P ≤ 0.01; ***P ≤ 0.001; ****P ≤ 0.000

3.2 Coenzyme Q depletion reshapes MCF-7 cells metabolism

3.2.1 Mitochondrial dysfunction induced by CoQ_{10} depletion

As widely described in section 2.5.5, 4-nitrobenzoic acid (4-NB) is a competitive inhibitor of coq2, a prenyltransferase involved in CoQ_{10} biosynthesis at the mitochondrial level, previously described. Fig. 20 shows that 4-NB treatment significantly decreased the ubiquinone level in MCF7 cell line by 60%.

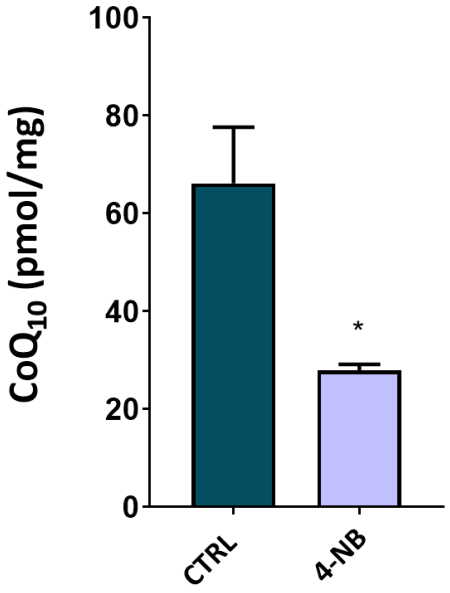

Figure 19 Total ubiquinone determination in control and CoQ depleted MCF-7 cells normalized on protein content, (n = 3). Error bars indicate the standard error of the mean (SD). p values were obtained using unpaired t-test with Welch's correction. * $p \leq 0.05$; ** $p \leq 0.01$.

Given that CoQ_{10} is an obligate component of the mitochondrial electron transport chain (ETC), shuttling electrons from NADH dehydrogenase (complex I) or succinate dehydrogenase (complex II) to the cytochrome bc1 complex (complex III). Therefore, depletion of CoQ_{10} pool could directly impair the oxygen consumption rate (OCR). Fig. 20A shows that the basal OCR, together with the spare respiratory capacity (the difference between uncoupled OCR and oligomycin inhibited OCR), were decreased by 4-NB treatment. Moreover, the OCR after oligomycin addition was unchanged, suggesting that 4-NB treatment does not induce proton leaking. The total absence of oxygen consumption in the presence of antimycin A rules out the possibility of extra-mitochondrial O_2

consumption. CoQ depleted cells showed low respiration rates, which could be related to an impairment of the electron transfer complexes. To clarify this point, we measured the activity of functionally isolated complex I, complex II and complex IV in MCF7 cells. We found that CoQ depletion did not affect complex I (Fig. 20B) and induced only a slight decrease of complex IV activity (Fig. 20D); conversely, CoQ depletion dramatically reduced complex II activity (Figure 20C).

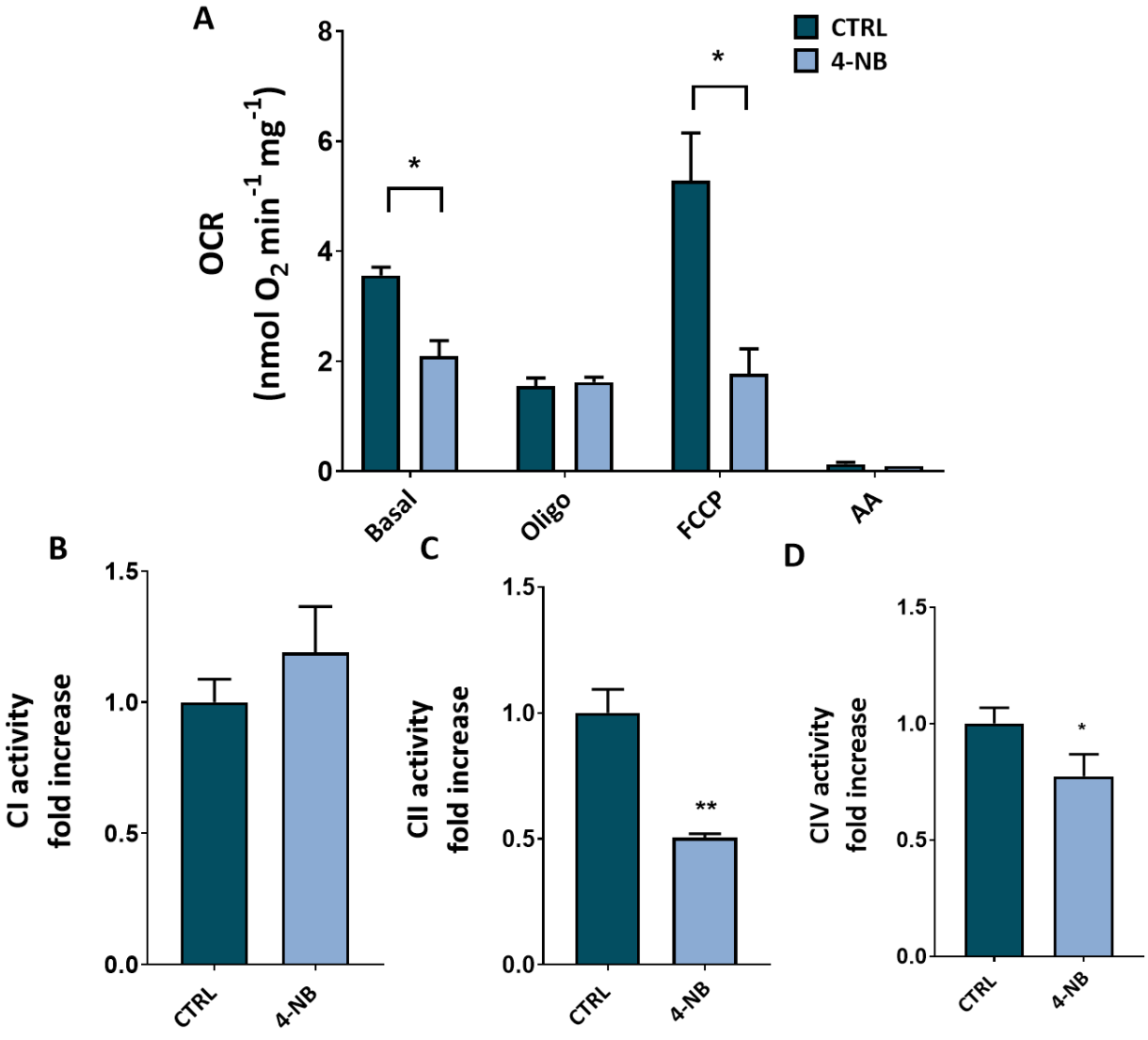

Figure 20 A) Oxygen consumption rate (OCR) in intact cells measured in DMEM (basal respiration), in the presence of oligomycin A (Oligo) and carbonyl cyanide 4-(trifluoromethoxy) phenylhydrazone (FCCP). To inhibit the mitochondrial respiration, 2µM Antimycin A was added at the end of each experiment. (n = 4). Electron transport chain complex I (**B**), II (**C**), and IV (**D**) enzyme activities were assessed in lysates from control and CoQ depleted cells. Results are displayed as fold increase (n = 3).

Since the mitochondrial transmembrane potential (ΔΨm) is a marker of functionality, we stained the cells with the fluorescent dye JC-1, which exhibits potential-dependent accumulation in mitochondria. Fig. 21A and B showed that CoQ depletion induced hyperpolarization in MCF7 cells, indicative of a reduced oxidative phosphorylation activity.

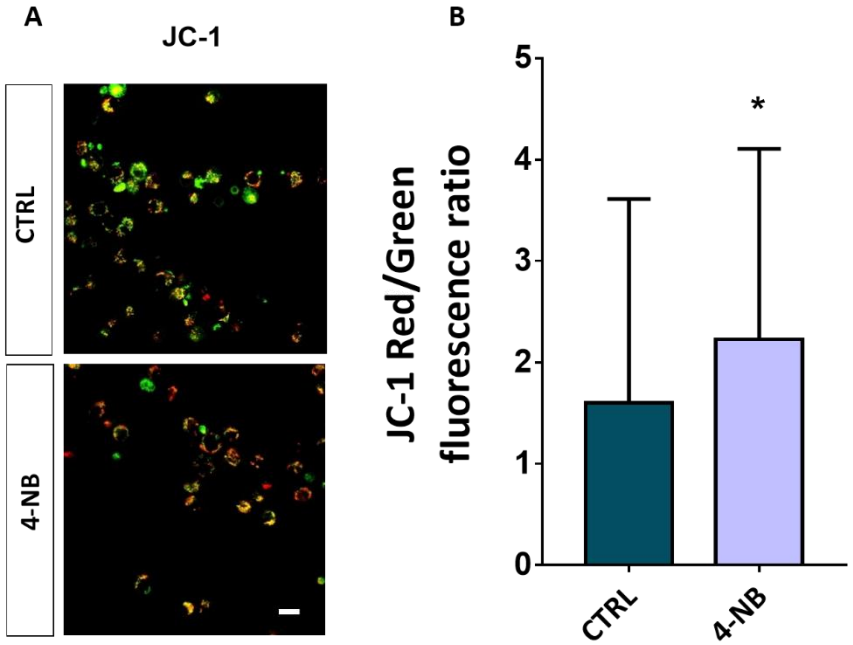

Figure 21 Representative micrographs and their quantification (**A**) of control and CoQ depleted cells stained with JC-1 dye, a cationic dye (green) which exhibits potential-dependent accumulation in mitochondria where it starts forming J aggregates (red). Scale bar: 70 µm. (**B**) The mitochondrial potential was assessed by measuring the red on green fluorescence intensity ratio. Two randomly chosen fields, from three independent experiments, were analyzed for each condition. Statistical analysis was performed using GraphPad Prism software. Error bars indicate the standard error of the mean (SEM). P values were obtained using unpaired t-test with Welch's correction. *P ≤ 0.05.

In eukaryotic cells, the CoQ_{10} and cholesterol share the initial part of their biosynthetic pathways. The inhibition of coq2 by 4-NB inhibits CoQ biosynthesis, making available substrates that can indirectly increase cholesterol synthesis. We measured the total cholesterol level in MCF-7 cells by using HPLC technique, finding that 4-NB treatment increased the cholesterol level in comparison to controls (Fig. 22).

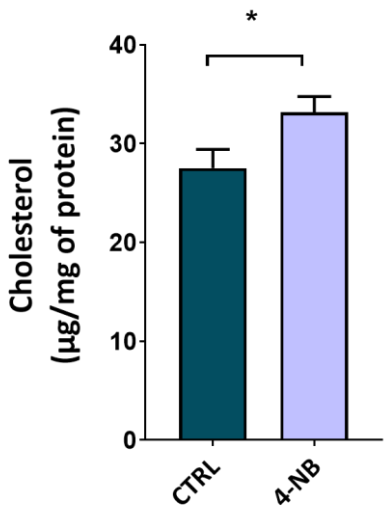

Figure 22 Total cholesterol content in cell lysate from control and CoQ depleted cells normalized on protein content. Error bars indicate the standard error of the mean (SEM). P values were obtained using unpaired t-test with Welch's correction. *P ≤ 0.05.

3.2.2 Mitochondrial morphology

In response to metabolic stresses, mitochondria could undergo morphology transitions, resulting in elongated or fragmented morphology. Changes in mitochondrial morphology can influence the cellular bioenergetic status and are implicated in embryonic development, metabolism, apoptosis, and autophagy [74 54 75]. To evaluate the mitochondrial network morphology, we stained the cells with mitotracker green (Fig. 23A) and measured the circularity and aspect ratio parameters (Fig. 23B, C). Mitochondria exhibiting a perfect circular shape have a circularity value close to 1.0 whereas more elongated mitochondria have a circularity value that is closer to zero. In CoQ depleted cells, we found an increased circularity value, compatible with a less elongated mitochondrial shape in comparison with control.

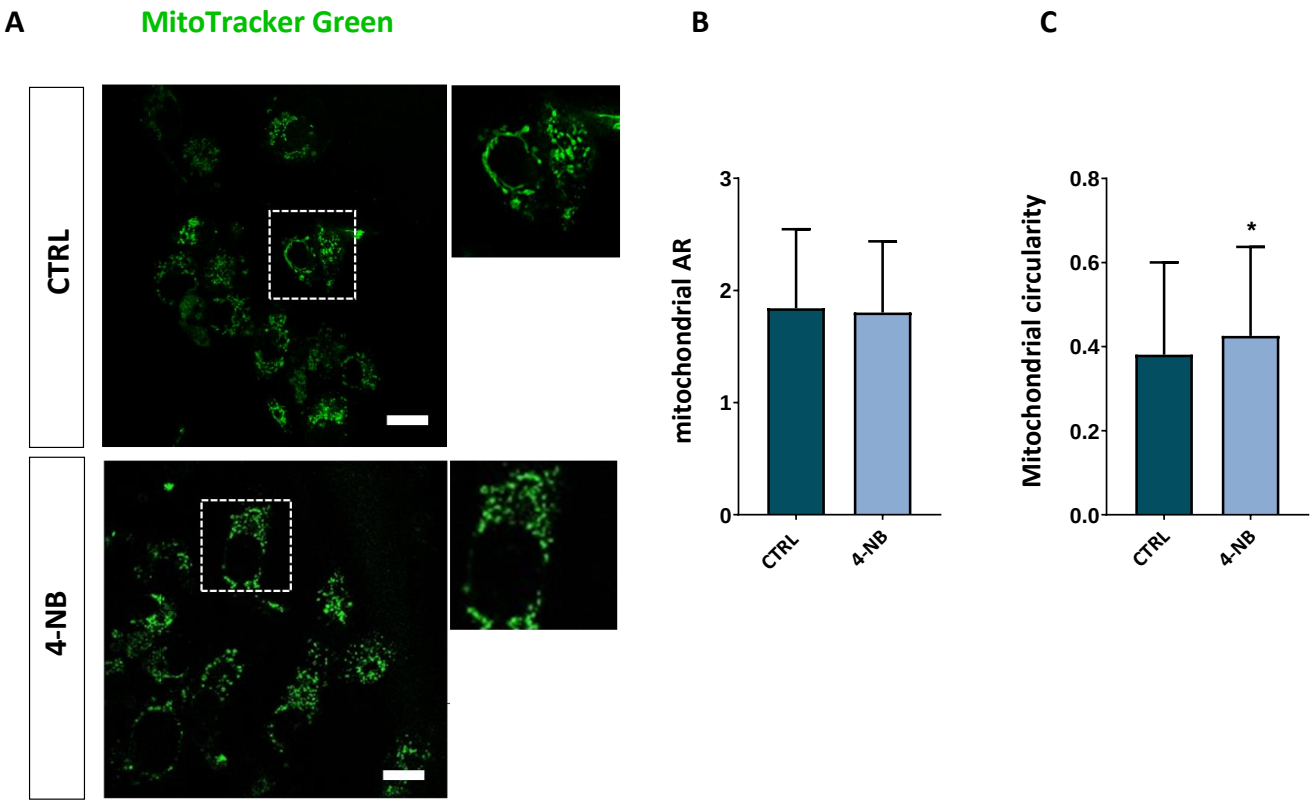

Figure 23 (A) Representative micrographs of control and CoQ depleted cells stained with Mitotracker green. Mitochondrial circularity value determination and aspect ratio (**B,C**) using ImageJ software. For each condition were analyzed at least two randomly chosen fields from three independent experiments. Scale bar: 70 µm. Statistical analysis was performed using GraphPad Prism software. Error bars indicate the standard error of the mean (SEM). P values were obtained using unpaired t-test with Welch's correction. *P ≤ 0.05.

3.2.3 Redox state and cellular bioenergetics in CoQ depleted cells

Mitochondria are critical for maintaining redox homeostasis since they are involved in many redox-dependent processes. They produce high amounts of reactive oxygen species (ROS) and present many redox systems, including glutathione (GSH/GSSG) and nicotinamide adenine dinucleotide (NADH/NAD^+) reduced/oxidized forms, pivotal for redox homeostasis maintenance.[76] Among these systems, NAD^+/NADH is a marker of cellular redox state, regulating catabolic versus anabolic reactions and able to link the oxidative phosphorylation with the TCA cycle. We measured the NAD(P)H level in cells treated with 4-NB, in the presence/absence of the specific complex I inhibitor

rotenone and the uncoupler FCCP. We observed a significant increase of intracellular NADH in CoQ depleted cells in comparison with controls. (Fig. 24A, B).

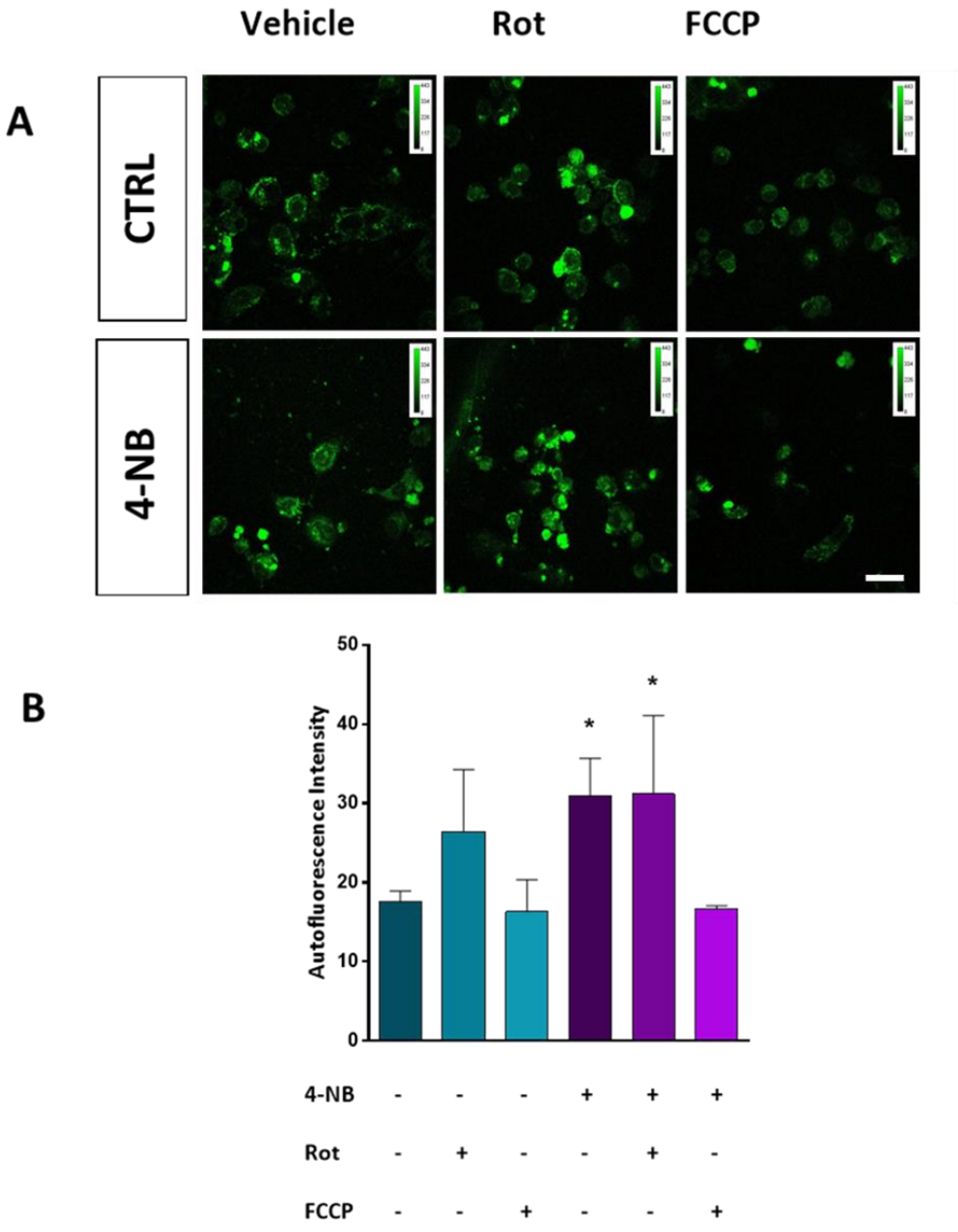

Figure 24 (**A**) Representative micrographs and their quantifications (**B**) of NAD(P)H autofluorescence in control and 4-NB treated cells in the presence of 10µM Rotenone (Rot) or 10µM carbonyl cyanide 4-(trifluoromethoxy) phenylhydrazone (FCCP). Scale bar: 70 µm. For each condition were analyzed at least two randomly chosen fields from three independent experiments with ImageJ software. Statistical analysis was performed using GraphPad Prism software. Error bars indicate the standard error of the mean (SEM). P values were obtained using unpaired t-test with Welch's correction. *$P \leq 0.05$.

.The addition of FCCP decreased the NADH level in both control and 4-NB-treated cells. An increased intracellular reducing power together with increased mitochondrial membrane potential could promote electron escape from the respiratory chain generating ROS. Furthermore, the depletion of an antioxidant molecule such as the reduced form of CoQ_{10}, could imbalance the ROS homeostasis in CoQ depleted cells. We found that CoQ depletion significantly decreased the GSH level in MCF7 cells (Fig. 25A). To address this point, we investigated the resistance to oxidative stress of 4-NB treated cells using the radical inducer TBH. Figure 25B shows that 4-NB treated cells are more vulnerable to TBH in comparison to controls. This result suggested that CoQ depletion unbalances the oxidative stress homeostasis, making cells unable to compensate for a further increase in ROS.

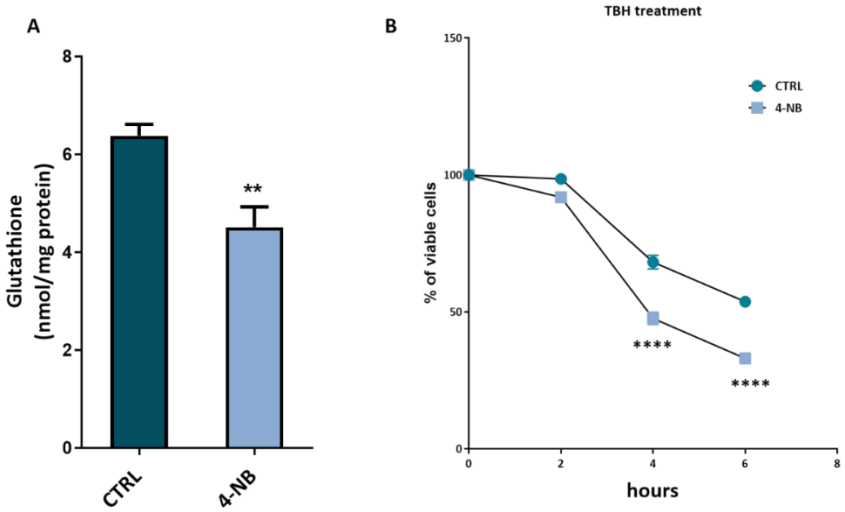

Figure 25 (**A**) Determination of reduced glutathione content determination in control and 4-NB treated cells. (**B**) MCF-7 cells were cultured in complete DMEM for 96 hours in the presence of 4mM 4-nitrobenzoic acid (CoQ depleted) or vehicle (CTRL), then the cells were exposed to 100µM tert-butyl hydroperoxide (TBH) up to 6 hours. For comparison between multiple groups, P values were obtained using the analysis of variance (ANOVA) followed by Tukey's post hoc test. *P ≤ 0.05; **P ≤ 0.01.

The redox imbalance found in CoQ depleted cells strongly suggests an energetic impairment. To better clarify this point, we measured the adenylate energetic charge in MCF7 cells using the following equation: ([ATP] + ½ [ADP])/([ATP] + [ADP] + [AMP]). It resulted that the energetic charge was unaffected by 4-NB treatment up to 4mM, while higher concentrations significantly decreased it

(Fig. 26A). Despite a reduced OXPHOS, cells treated with 4mM 4-NB maintained the energetic charge, implying an adaptive metabolic response. As previously resulted and described in T67 cell line, [77] mitochondrial-defective cells can switch their metabolism towards glycolysis and/or downregulate the energy demand, to face with impaired oxidative phosphorylation. Previous results in T67, reported a metabolic switch toward glycolysis in cells depleted of CoQ, driven by the hypoxia-induced factor HIF-1α. To evaluate this point the intracellular oxygen level has been measured, using an iridium (III) complex dye (BTP), mentioned and used previously in section 5.1.5 and 5.2.6. BTP fluorescence intensity was noteworthy higher after 4-NB treatment (Fig. 26B). The BTP fluorescence intensity observed in CoQ depleted cells suggests a decreased intracellular oxygen content. Thus we performed HIF-1α western blot and we observed an higher stabilitazion in 4-NB treated cells than control. (Fig. 26C).

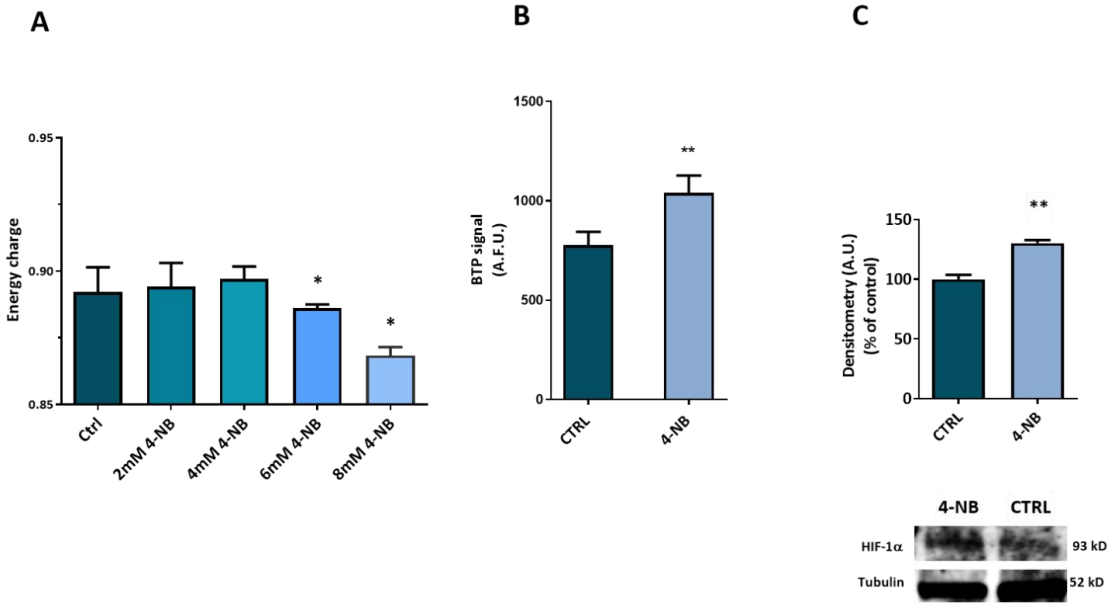

Figure 26 (**A**) Cellular energy charge quantification in cells cultured for 96 hours in the presence of different concentrations of 4-NB (n = 3).(**B**) Quantification of fluorescence emission in control and 4-NB treated cells stained with the dye bis (2-(2'-benzothienyl)-pyridinato-N, C30) iridium (acetylacetonate) (BTP). BTP is a live-cell O2 sensor which fluorescence emission is quenched by molecular oxygen. Error bars indicate the standard error of the mean (SEM). (**C**) Quantification of HIF-1α performed by densitometry analysis, using tubulin as a loading control (n = 2). Statistical analysis was performed using GraphPad Prism software. For comparison between two groups, P values

were obtained using unpaired t-test with Welch's correction. For comparison between multiple groups, P values were obtained using the analysis of variance (ANOVA) followed by Tukey's post hoc test. *P ≤ 0.05; **P ≤ 0.01.

3.2.4 Glucose uptake and utilization in CoQ depleted cells.

Glucose uptake in CoQ depleted cells was assessed using the fluorescent glucose analogue (2-NBDG) Fig. 27.

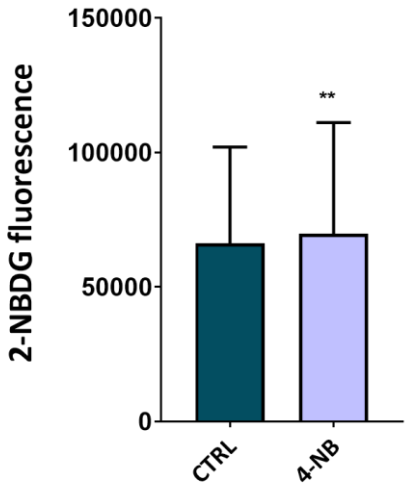

Figure 27 MCF-7 cells were cultured in complete DMEM for 96 h in the presence of 4 mM 4-nitrobenzoic acid (CoQ depleted) or vehicle (CTRL). Glucose uptake determination in MCF-7 cells using the glucose fluorescent analogue 2-deoxy-2-((7-nitro-2,1,3-benzoxadiazol-4-yl) amino)-D-glucose (2-NDBG). Statistical analysis was performed using GraphPad Prism software. Error bars indicate the standard error of the mean (SEM). p values were obtained using unpaired t-test with Welch's correction. *P ≤ 0.05; **P ≤ 0.01.

Taking into account that an increased glucose uptake rate accounts for the glycolytic phenotype induced by CoQ depletion, we verify a possible increased expression of glucose transporters. We evaluated by immunofluorescence the expression of the transporters GLUT1 and GLUT3, which largely contribute to glucose uptake. CoQ depleted cells showed an increased expression of GLUT1 and GLUT3 in comparison to controls (Fig. 28A, B, C).

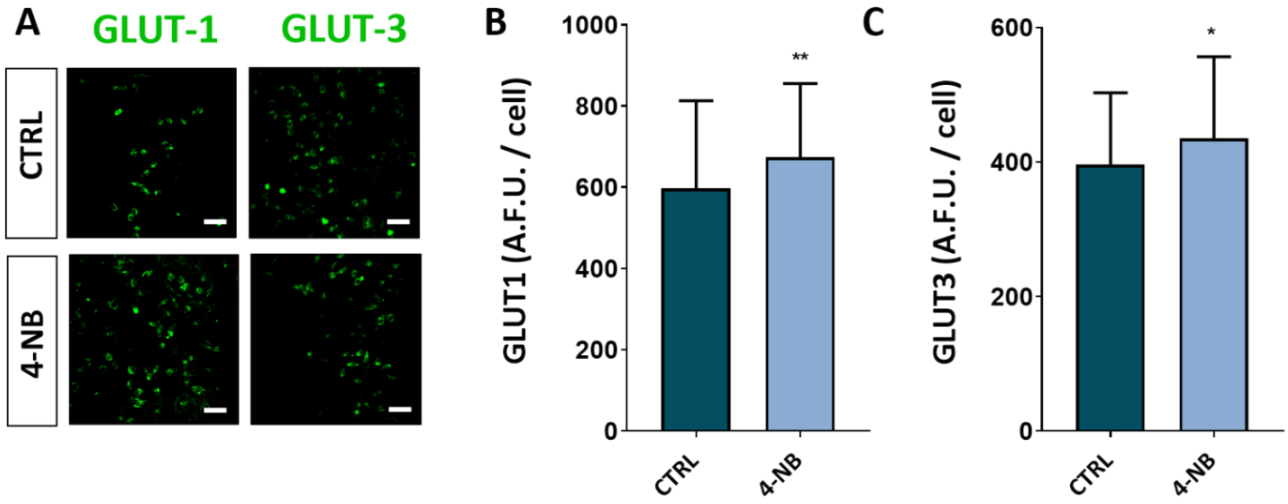

Figure 28 A) Representative micrographs and their quantification (**B**) of GLUT1 and (**C**) GLUT-3 immunostaining in control and CoQ depleted cells. Scale bar: 70 µm. Statistical analysis was performed using GraphPad Prism software. Error bars indicate the standard error of the mean (SEM). p values were obtained using unpaired t-test with Welch's correction. *P ≤ 0.05; **P ≤ 0.01

Increased lactate production is a distinctive feature of glycolytic metabolism. As shown in Fig. 29A, the basal lactate secretion rate was 1.46±0.11 nmol mg-1 hour-1, and 1.03±0.09 nmol mg^{-1} $hour^{-1}$ in control and CoQ depleted cells, respectively. The maximal lactate secretion rate, achieved by inhibiting the oxidative phosphorylation with oligomycin A, was 3.78±0.29 nmol mg-1 hour-1 and 7 2.28±0.21 nmol mg^{-1} $hour^{-1}$ in control and CoQ depleted cells, respectively. Remarkably, oligomycin treatment induced an increase of the lactate secretion rate compared to the basal value by 260% in control and 220% in CoQ depleted cells (Fig. 29A, B); this suggests that CoQ depletion has compromised the mitochondrial functionality pushing the cells toward a glycolytic metabolism. Pyruvate kinase (PK) is one of the regulatory enzymes of the glycolytic pathway, which catalyses the conversion from phosphoenolpyruvate (PEP) to pyruvate. Calculating the Km and Vmax parameters of PK from the Michalis-Menten (Fig. 29C) and Lineweaver-Burk plots (Fig. 29D), we found that the CoQ depletion decreased the Km value of the enzyme, while unaffecting the Vmax. The higher affinity of PK to PEP in 4-NB treated cells suggests an allosteric activation of the enzyme.

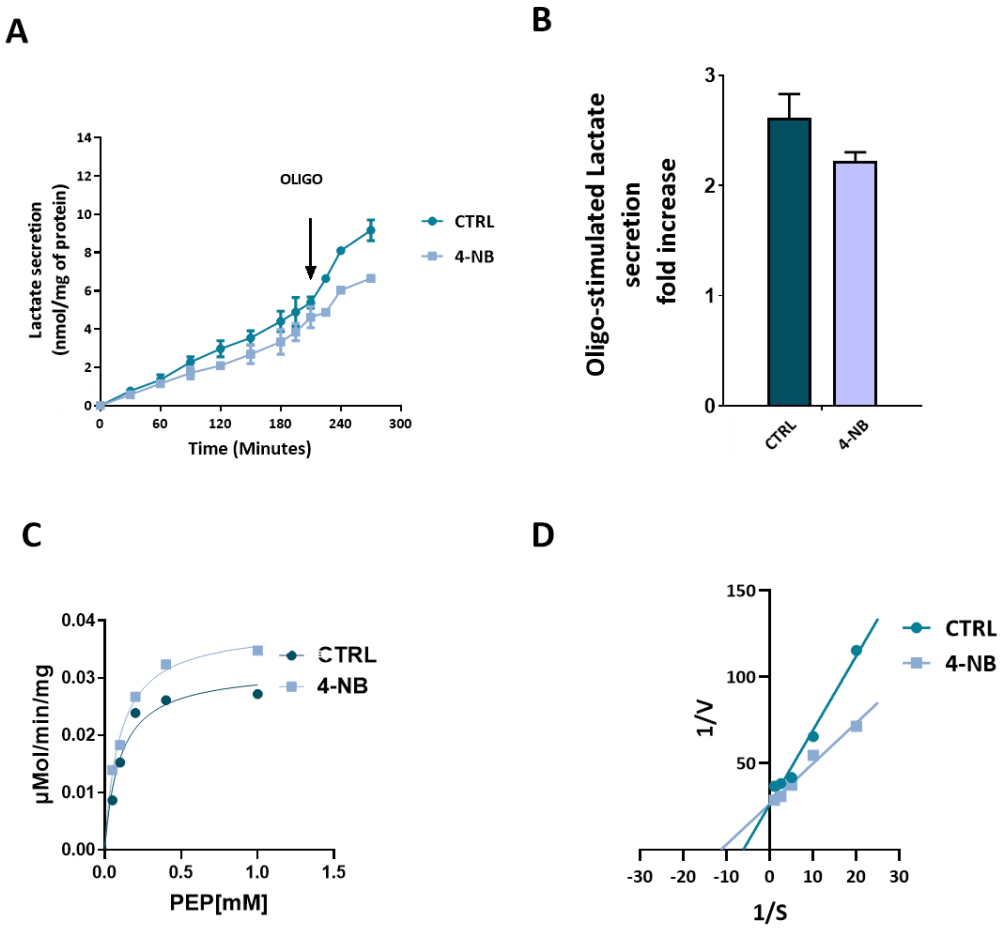

Figure 29 A) Lactate secretion determination in culture medium from control and CoQ depleted cells. 1µM Oligomycin A was added to maximize lactate production. Lactate was quantified by HPLC and the data were normalized on cellular protein content. **B**) Fold increase of cellular lactate secretion after oligomycin A addition in control and CoQ depleted cells. **C**) Michaelis and Menten and (**D**) Lineweaver-Burke plots of pyruvate kinase (PK) activity obtained in the presence of increasing concentrations of phosphoenolpyruvate (PEP) in control and CoQ depleted cells.

3.2.5 . Glutaminolysis, pyruvate metabolism, and TCA cycle in CoQ depleted cells

Increased glutamine anaplerosis is a key metabolic pathway for OXPHOS-defective cells. Anaplerotic replenishment of the TCA cycle from glutaminolysis is a two steps conversion, involving firstly the hydrolysis of glutamine, through glutaminase (GLS), and then the conversion of glutamate to α-KG, through glutamate dehydrogenase (GDH). In Figure 31 A, we showed that CoQ depleted cells present a glutaminase (GLS) activity markedly increased, while glutamate dehydrogenase (GDH) activity was unaffected. Additionally, CoQ depletion induced upregulation of both NAD(P)+-dependent isocitrate

dehydrogenase and NAD+-dependent isocitrate dehydrogenase, as well as malate dehydrogenase (MDH), malic enzyme (ME) and lactate dehydrogenase (LDH). Pyruvate dehydrogenase complex (PDC) and α-ketoglutarate dehydrogenase (KGDC) activities were unaffected. The cell cycle analysis data reported that CoQ depleted cells arrested in G0/G1 phase, related to a decrease of the S phase (Fig. 30B,C)

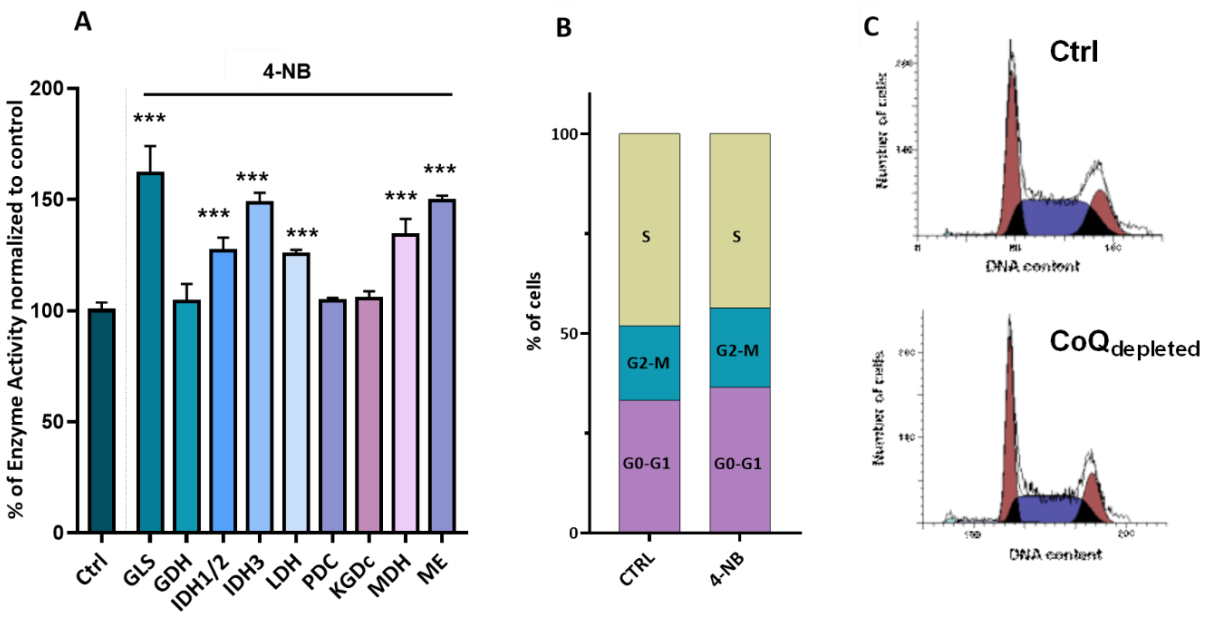

Figure 30 MCF-7 cells were cultured in complete DMEM for 96 hours in the presence of 4mM 4-nitrobenzoic acid (CoQ depleted) or vehicle (CTRL). (**A**) Enzyme activities (glutaminase, GLS; glutamate dehydrogenase, GDH; isocitrate dehydrogenase1,2 and 3; IDH1/2, IDH3; lactate dehydrogenase LDH; pyruvate dehydrogenase complex, PDC; α-ketoglutarate dehydrogenase, KGDC; malate dehydrogenase, MDH; malic enzyme ME) in control and CoQ depleted cells. Data refers to the percentage increase in comparison with controls. (**B, C**) Cell cycle analysis and quantification by flow cytometry in control and CoQ depleted cells using propidium iodide dye staining. The column graph shows the percentage of cells in each cell cycle. Statistical analysis was performed using GraphPad Prism software. Error bars indicate the standard error of the mean (SEM). P values were obtained using the analysis of variance (ANOVA) followed by Tukey's post hoc test. ***P ≤ 0.001.

3.2.6 Effect of mitochondrial dysfunction on cell proliferation

We investigated the effect of ubiquinone depletion on cell growth, finding that 4-NB treatment suppressed MCF7 cell proliferation in a time and concentration-dependent manner (Fig. 32A), as

verified in T6 and other cell line like fibroblast [40] [43] To assess a possible switch from an oxidative toward a glycolytic metabolism of the CoQ depleted cells, we used the competitive glycolysis inhibitor 2-DG (Fig. 31C), or we replaced the glucose with galactose in the culture media (Fig. 32B), showing that CoQ depletion sensitized the cells both to 2-DG inhibition and galactose treatment, highlighting their energy dependence on glycolysis. Nevertheless, we reported in Fig. 31D that CoQ depletion did not sensitize the cells to glutamine deprivation. Since mediates the survival response to hypoxic stress could be mediated by HIF-1α stabilization, we treated the cells with a cell-permeant α-ketoglutarate (TαKG), able to increase the degradation of HIF by reactivating the prolyl hydroxylase domain (PHD). IC50 values of 176.5µM and 122.1µM for control and CoQ depleted cells were calculated using different TαKG concentrations (Fig. 31E), suggesting that cancer cells with mitochondrial dysfunction depend on HIF-1α stabilization.

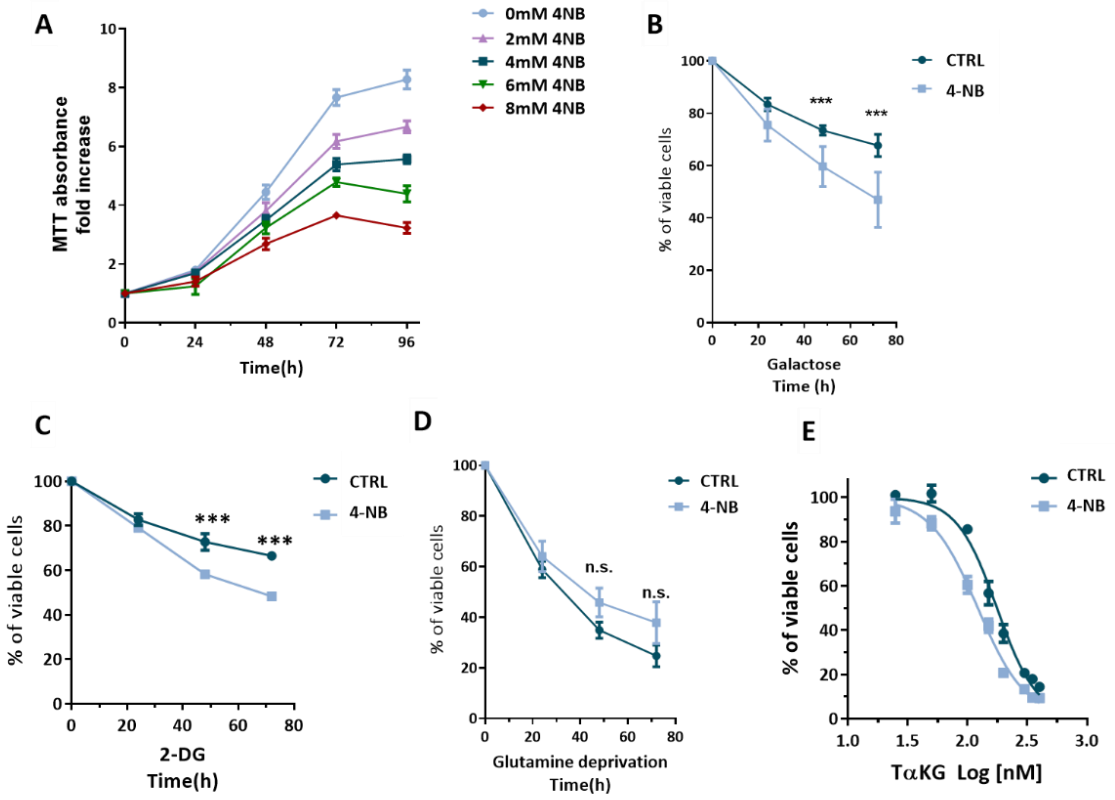

Figure 31 (**A**) MCF-7 cell proliferation was assessed by MTT assay in the presence of different concentrations of 4-nitrobenzoic acid up to 96 hours. (**B**) Control and CoQ depleted cells were cultured in glucose free medium supplemented with dialyzed FBS and 5.5mM galactose. (**C**) Control and CoQ depleted cells were cultured in

complete medium in the presence of 10 mM hexokinase (HK) inhibitor 2-deoxyglucose (2-DG). **D**) Control and CoQ depleted cells were cultured in a glutamine free complete medium. (**E**) Control and CoQ depleted cells were cultured in complete medium for 24 hours in the presence of different concentrations of trifluoromethyl benzyl-α-ketoglutarate (Tα-KG). Cell proliferation was assessed by MTT assay. Cell proliferation was assessed by MTT assay. Statistical analysis was performed using GraphPad Prism software. Error bars indicate the standard error of the mean (SEM). P values were obtained using unpaired t-test with Welch's correction. ***P ≤ 0.01.

Finally, we tested the sensitivity of CoQ depleted cells to two common anticancer agents: doxorubicin and cisplatin. The results reported belove show that CoQ depletion does not affect the IC50 for cisplatin (Fig. 32A), while increased the IC50 for doxorubicin (Fig. 32B).

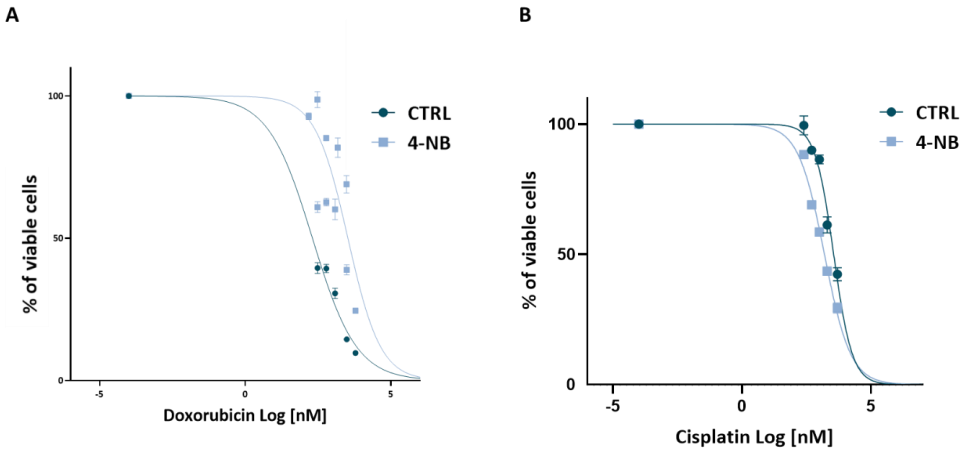

Figure 32 Control and CoQ depleted cells were cultured in complete medium for 24 hours in the presence of different concentrations of doxorubicin (**A**) and cisplatin (**B**) for 24 hours. Cell proliferation was assessed by MTT assay. Statistical analysis was performed using GraphPad Prism software. Error bars indicate the standard error of the mean (SEM). P values were obtained using unpaired t-test with Welch's correction. ***P ≤ 0.01.

3.2.7 Effect of CoQ depletion on spheroids formation and spheroid oxygen content

To investigate the ability to form spheroids in CoQ depleted cells, we used 3D MCF-7 spheroid model treated with 4-NB. [78] As it has been shown previously in T67 cells, CoQ_{10} depletion could lead to a hypoxic cell condition. Thus we tried to translate our previous findings on spheroid growth and spheroid oxygen content. To determine this, we growth control and CoQ depleted cells for 14 days in dishes with a non-adherent surface, finding that CoQ depletion significantly inhibited the formation of spheroids (Fig. 33A, B).

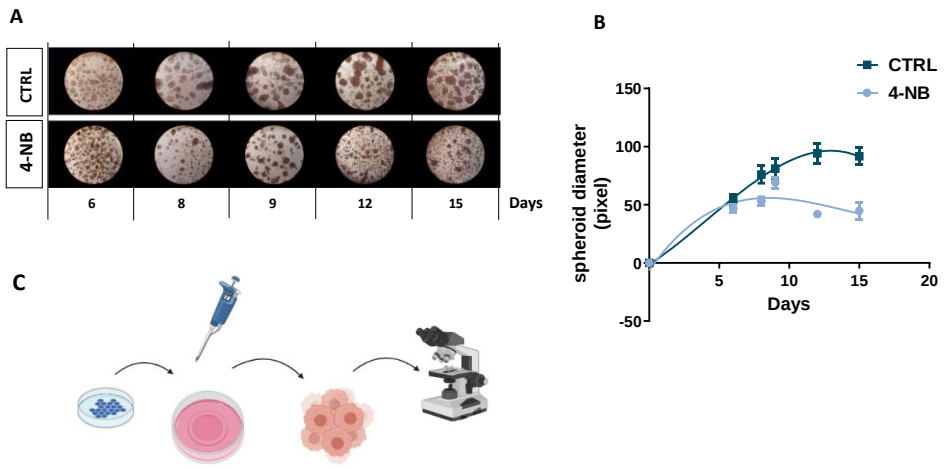

Figure 33 (**A**) Representative phase contrast light micrographs of control and CoQ-depleted spheroids at different time points. Control and CoQ depleted cells were cultured in complete medium and complete medium supplemented with 4 mM 4-NB respectively in high Bioinert Ibidi dishes with 25 % of Methocel to allow spheroids formation. (**B**) The diameter of the spheroid was monitored for 15 days and measured using ImageJ software . (**C**) Schematic overview of the spheroid generation protocol (suspension culture) in high Bioinert Ibidi dishes, described in section 2.6.

Furthermore, we stained the spheroids with the oxygen-sensitive probe BTP, finding that CoQ-depleted spheroids were in a more hypoxic state in comparison to controls, as pointed out from BTP fluorescence emission.

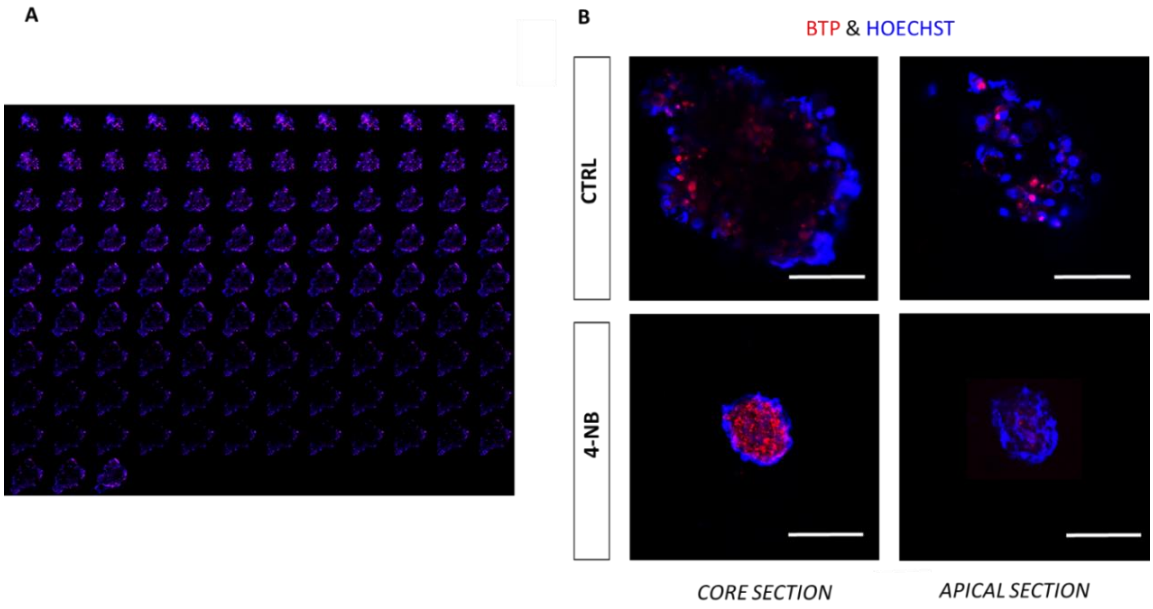

Figure 34 (**A**) Representative micrographs of MCF-7 spheroid Z-stacks. (**B**) Representative micrographs of control and CoQ-depleted spheroids, core section and apical section, stained with Hoechst and the oxygen sensitive probe BTP. Bar size = 100µm.

3.3 Effects of CoQ_{10} depletion induced in SH-SY5Y by targeting COQ2 by CRISPR-Cas9 genome editing

3.3.1 Generation and Characterization of COQ2 SH-SY5Y mutated cells

To investigate the functional role of COQ2 variant we induced mutation in SH-SY5Y cell line using the CRISPR/Cas9 technology. Cells were transfected with gRNA and Cas9-nickase plasmids and the oligo DNA carrying the variant to insert the specific modification in SH-SY5Y DNA (Fig. 35). Homozygous and heterozygous editing was observed in several clones, which were further confirmed using PCR and Sanger sequencing. Several clones were obtained but only a few clones were chosen for further study. Among different clones, genetic analysis identified a heterozygous mutation with a 59 pair bases deletion (H9) and an omozygous mutation with a 28 bp deletion and a premature stop codon (C6). (Fig. 36). These clones, carrying the specific change, have been amplified and were used for the analysis. A SH-SY5Y clone that underwent the same CRISPR/Cas9 genome editing approach but resulted in no changes, was used as a control cell line (hence defined WT throughout the text). qPCR showed a reduced level of the COQ2 transcript. The presence of COQ2 m RNA maybe is due to nonsense-mediated mRNA decay mechanisms.[79](Fig. 37).

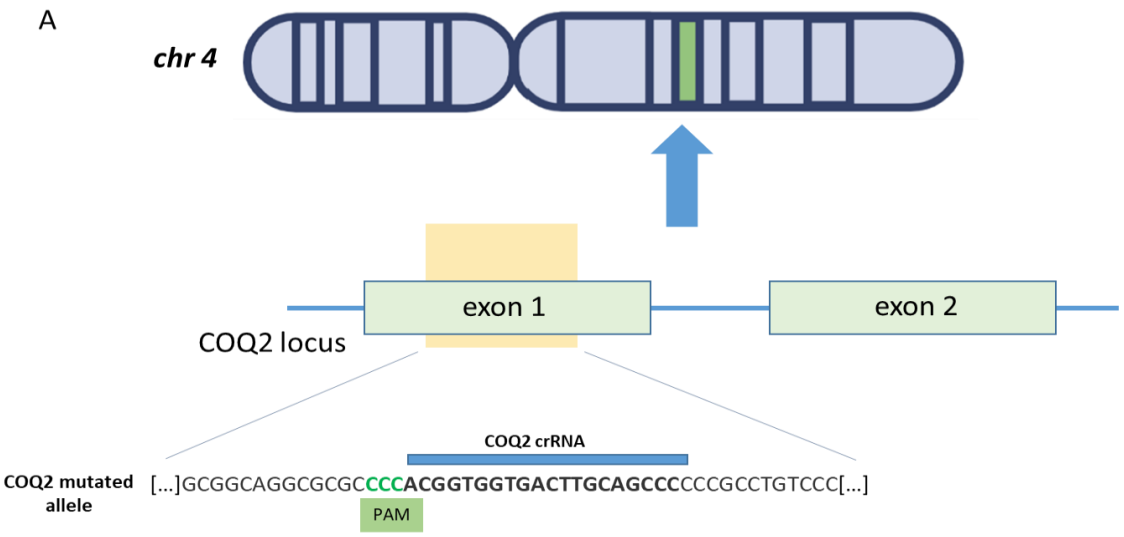

Figure 35 Generation of COQ2 mutated SH-SY5Y cell line.

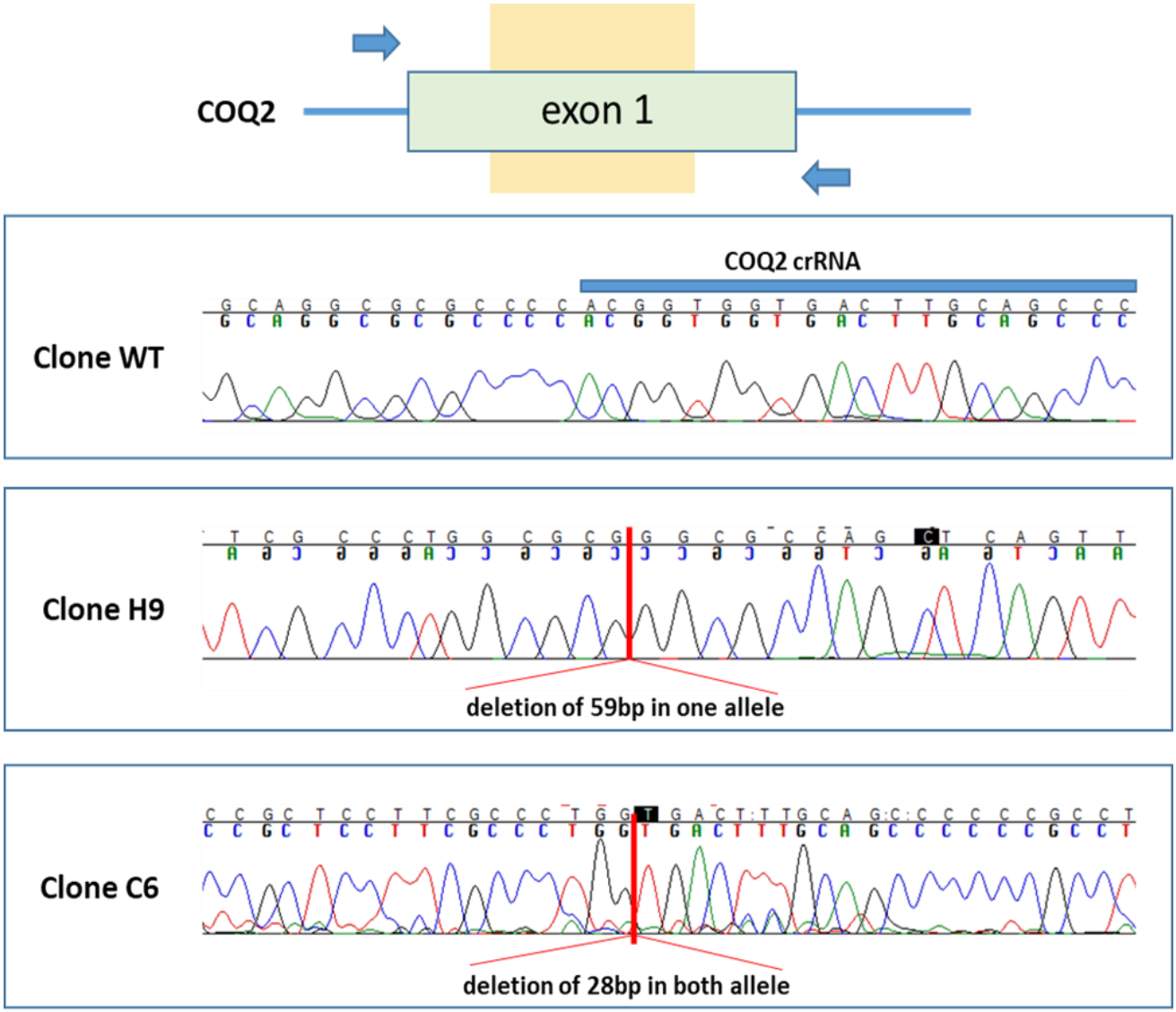

Figure 35 Generation of COQ2 mutations in SH-SY5Y cell line. SH-SY5Y cell were transfected with CRISPR/Cas9 and genotyped. Electropherogram shows COQ2 sequence carrying the mutation on the clone H9P1 and on the clone C6P2.

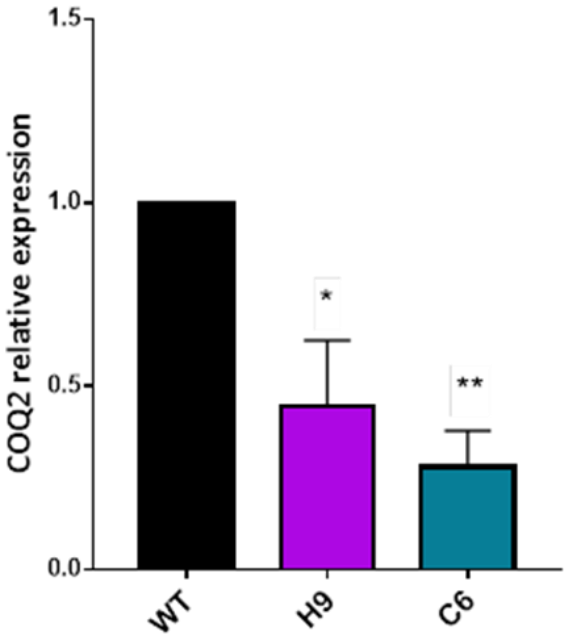

Figure 36 Relative level of COQ2 transcript normalized to WT. Error bars represent standard deviations of three experiments. For comparison between multiple groups, P values were obtained using the analysis of variance (ANOVA) followed by Tukey's post hoc test. *P ≤ 0.05; **P ≤ 0.01.

3.3.2 CoQ_{10} depletion induced by COQ2 mutation

The content of CoQ_{10} in cultures was determined by HPLC analysis. Since in the first month clones were maintained in DMEM supplemented with a hydrosoluble Q10 formulation, we were able to detect. Q10 in all clones even after one week of Q10-free culture media. (Fig. 39A). Performing the extraction in cells maintained for two weeks in a medium without Q10 supplementation, HPLC analysis revealed a Q10 content 50% lower in H9 and in C6 Q10 peak could not be detected (Fig.38-39).

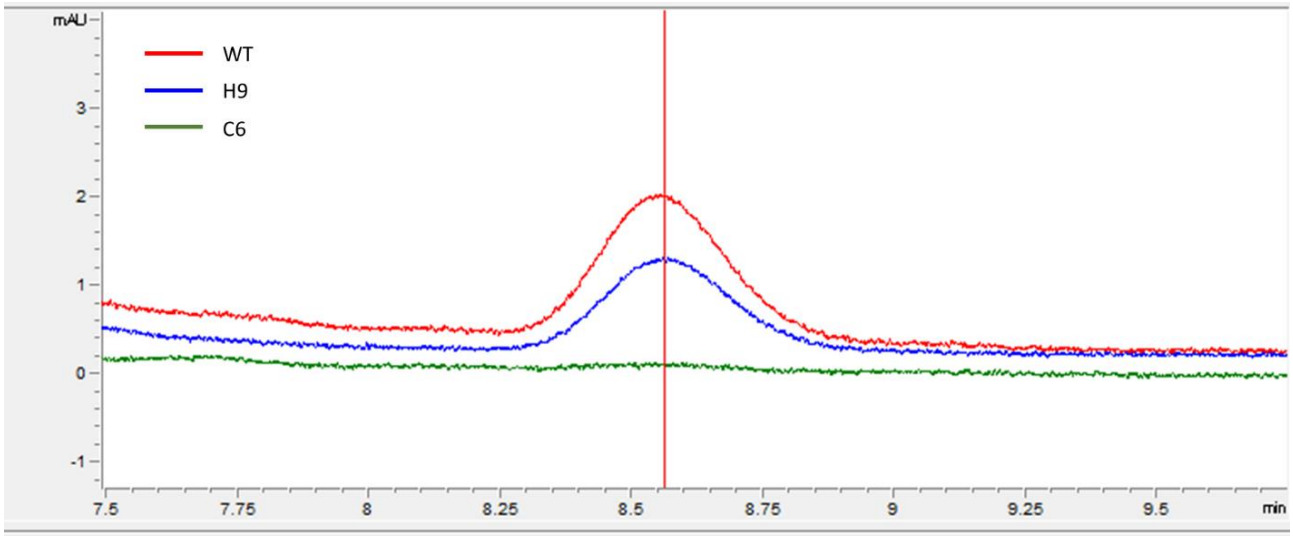

Figure 37 Representative overlaid chromatograms of CoQ_{10} determination (HPLC with electrochemical detection) extracted by HPLC in clones. (Peaks are not normalized). Quantification is reported in figure 39B.

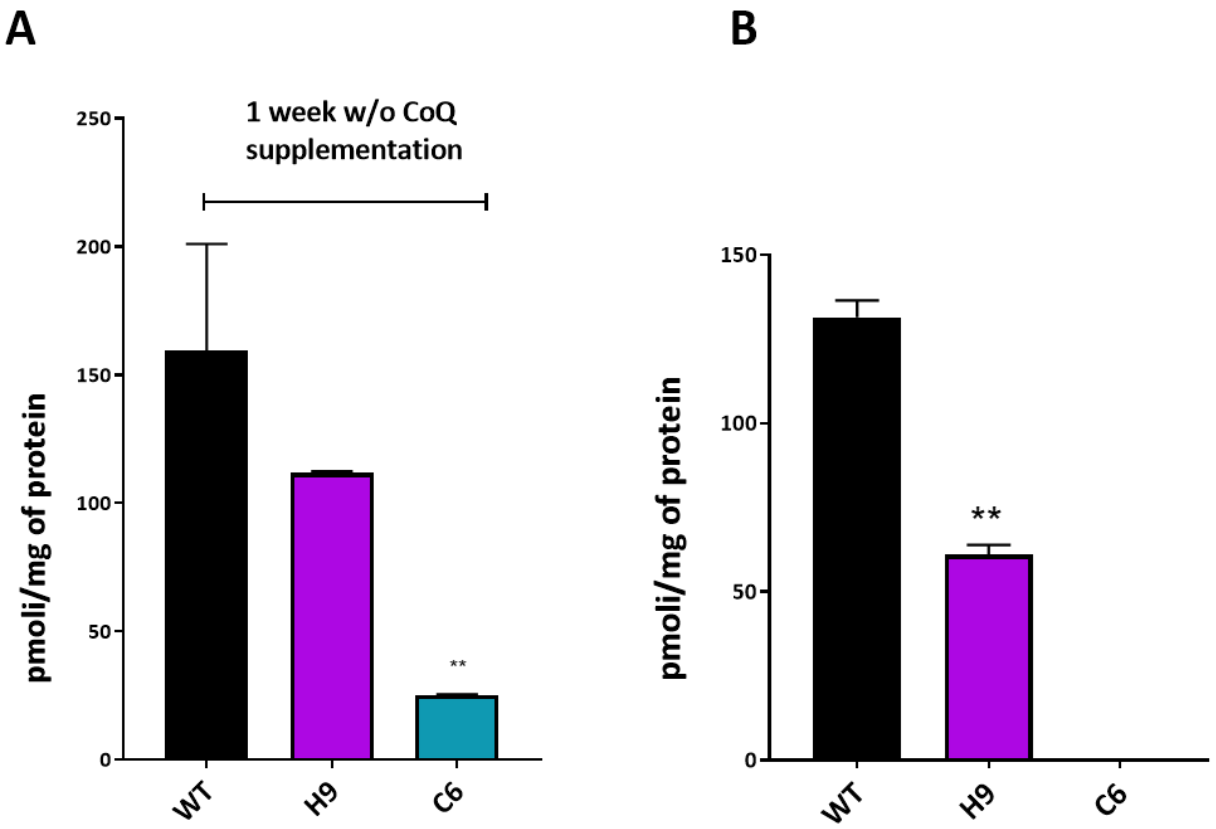

Figure 38 Q10 content in clones (**A**) After one week of Q water-soluble formulation (**B**) without Q supplementation for comparison between multiple groups, P values were obtained using the analysis of variance (ANOVA) followed by Tukey's post hoc test. **P ≤ 0.01.

Although for CRISPR-Cas 9 genome editing, guide RNAs with the lowest possibility of off-targets were chosen, to confirm that Q10 level was not affected in WT by other possible mutations or interferences, we performed some experiments on SH-SY5Y control cell, that never underwent under CRISPR-Cas 9 editing. Throughout the next and in the respective figures these cells are named SH-SY5Y CTRL, to be distinguished by WT. Moreover, we performed some experiment on SH-SY5Y CTRL to assess whether 4-NB inhibition induced the same effects observed previously in T67 and MCF-7, such as Q10 depletion, assessed by HPLC, and proliferative rate decrease, performed by MTT. As reported in the graph belove (Fig. 39A) CoQ_{10} content in SH-SY5Y control is similar to WT. The decrease of Q10 in SH-SY5Y is dose-dependent and it is in accordance with the depletion obtained in MCF-7 and T67. [77] [80] Besides, CoQ_{10} depletion presented a detrimental effect on proliferative rate in a time and dose-dependent manner and similarly to MCF-7 and T-67, as reported in Fig. 40B.

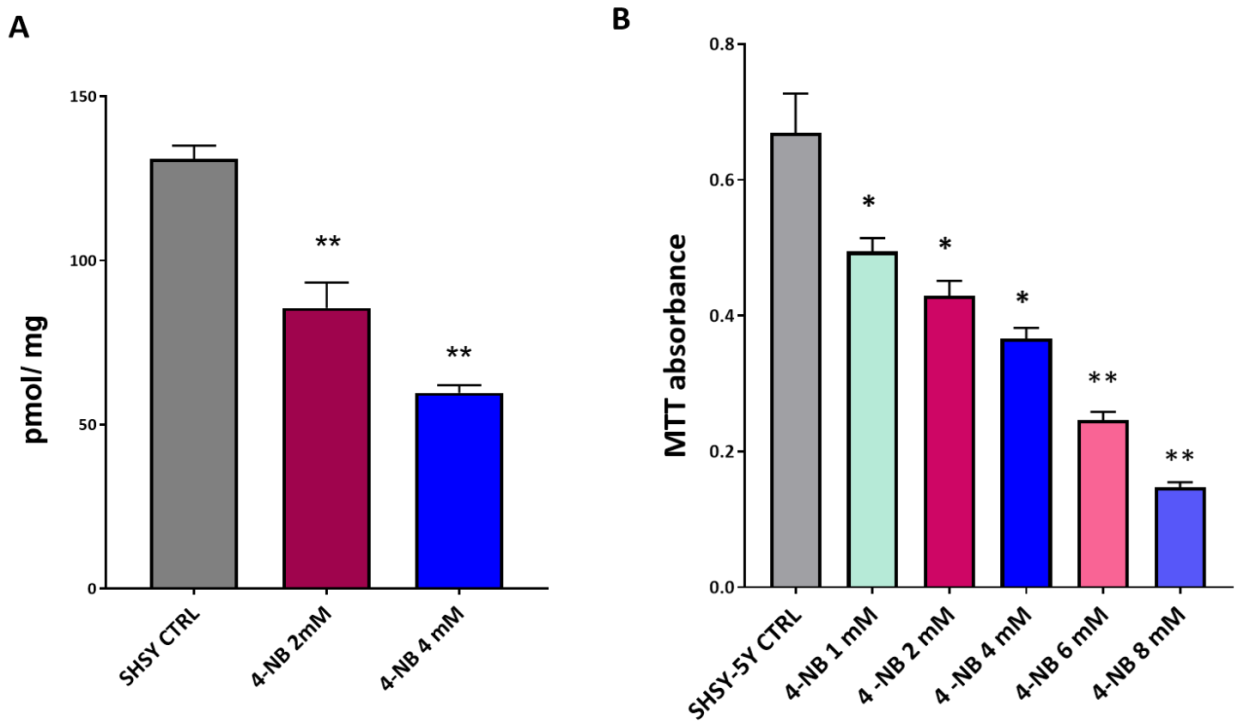

Figure 39 Effects of 4-nb treatment on SH-SY5Y cells. (**A**) HPLC Q10 content in SH-SY5Y 4-NB treated cells after 96 hours. (**B**) Effect of 4-NB treatment on SH-SY5Y proliferation. Graph show MTT absorbance after 96 hours of treatment. For comparison between multiple groups, P values were obtained using the analysis of variance (ANOVA) followed by Tukey's post hoc test. *P ≤ 0.05; **P ≤ 0.01.

3.3.3 Effects on growth rate

The growth rate of CoQ depleted cells was very low, in particular, the growth rate of the C6 clone was considerably lower in comparison to the control cells. Since CoQ is a critical cofactor for pyrimidine nucleotide biosynthesis, we supplemented culture medium with uridine (50 µg/mL). Uridine was able to restore cell proliferation in both clones (Fig. 41B). We also evaluated the combined supplementation of water-soluble Q10 and uridine (Fig. 41C) without observing any additional increment in the growth rate in both clones. To better clarify the metabolic needs of the cell we evaluated the proliferation rate in the presence of substrates able to reduce the glycolytic flux. To this scope, we used 2-DG, a competitive inhibitor of glucose, and galactose, able to force cells to have an increased reliance on oxidative phosphorylation (OXPHOS) for energy. In both cases, H9 and C6 presented a decrease growth rate. In all cases, the reduction of glycolytic flux had a higher effect on the homozygotic cell line. (Fig. 41D-F).

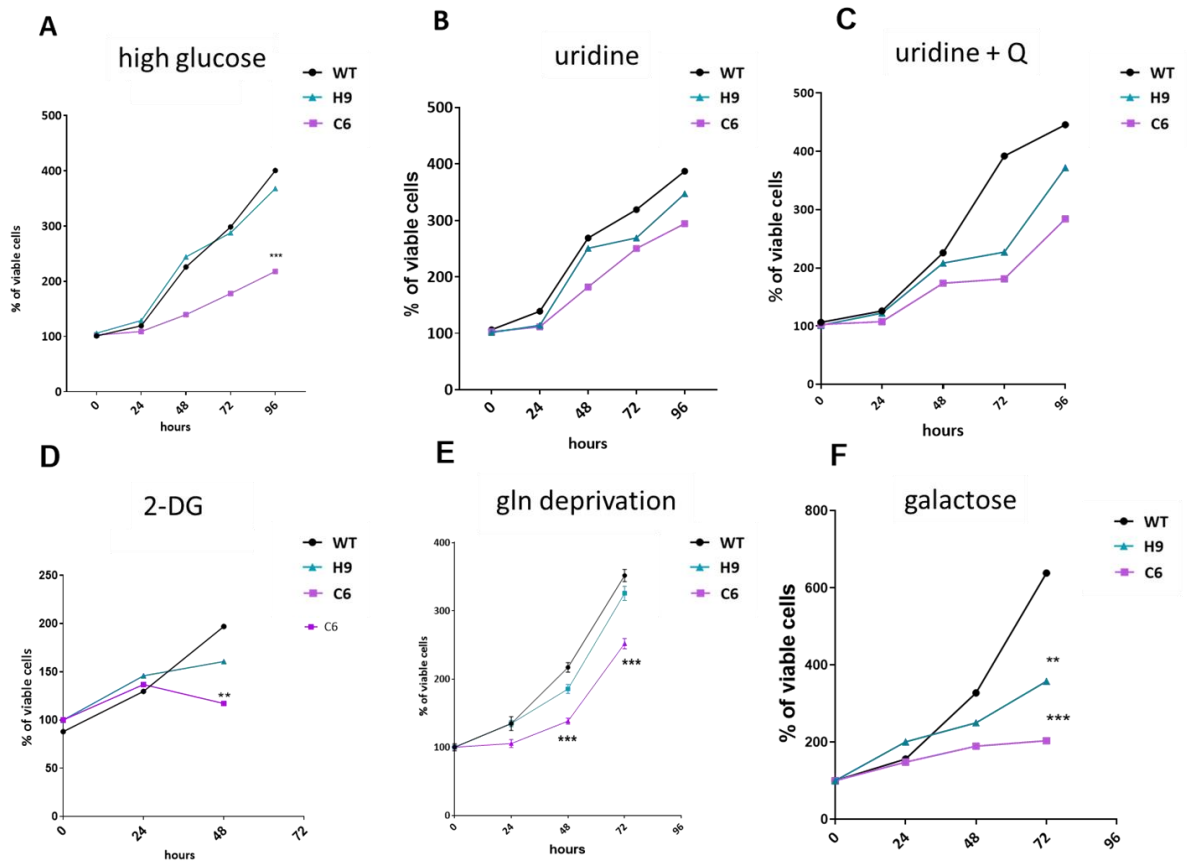

Figure 40 Cell proliferation was assessed by MTT assay in the presence of different culture media. (**A**) Cells were cultured in complete medium supplemented with FBS. (**B**) Cells were cultured in a complete medium supplemented with FBS in the presence of uridine. (**C**) Cells were cultured in complete medium supplemented with FBS in the presence of uridine and Q10 (**D**) Cells were cultured in complete medium supplemented with FBS in the presence of 10 mM hexokinase (HK) inhibitor 2-deoxyglucose (2-DG). (**E**) Cells were cultured in a glutamine free complete medium. (**F**) Cells were cultured in DMEM glucose-free medium supplemented with dialyzed FBS and 5.5mM galactose. Statistical analysis was performed using GraphPad Prism software. Error bars indicate the standard error of the mean (SEM). P values were obtained using unpaired t-test with Welch's correction. *P ≤ 0.05; **P ≤ 0.01.***P ≤ 0.001.

3.3.4 Morphology and spheroid formation

To further characterize COQ2 mutated cells, we analysed their morphology with hematoxylin and eosin staining, and cytoskeleton with phalloidin staining. Hoechst staining allowed us to distinguish nuclei. In C6 cell the morphology reveals a rearrangement of cytoskeleton, loss of neurite-like formations and round-shaped cell body (Fig. 42). To further characterize COQ2 mutated cells, we analysed morphology with hematoxylin and eosin staining, and cytoskeleton. We used Hoechst to stain nuclei and better distinguish the different cells.

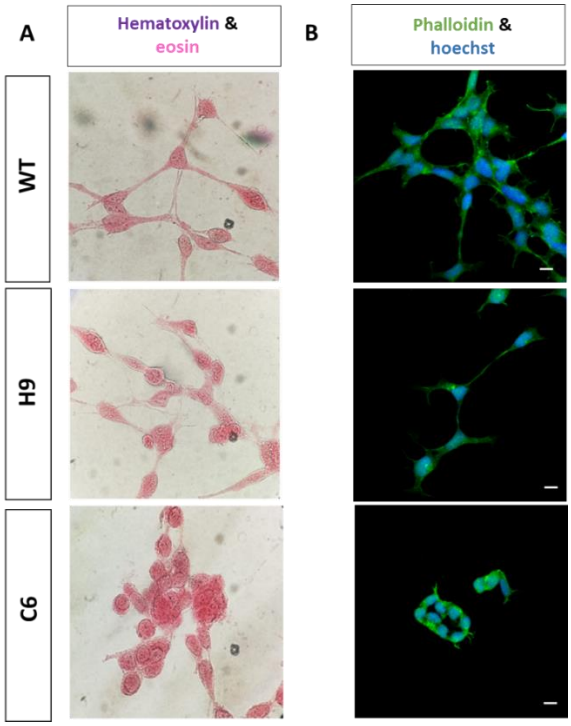

Figure 41 (**A**) Representative micrographs of haematoxylin and eosin staining (**B**) Representative micrographs of phalloidin (green) and Hoechst (blue) staining. Size bar:10 µm.

Taking into account that two-dimensional systems cannot always provide a complex and dynamic microenvironment for cells, we performed some experiments in three-dimensional cell culture, in order to investigate whether Q10 depletion could affect spheroid formation, as reported in Fig. 43. After 14 days WT and H9 cell formed more condensed and bigger spheroids (Fig. 43A). In contrast, C6 and SH-SY5Y 4-NB treated cells form smaller spheroids. To better evaluate spheroids dimension, we analysed diameters. (Fig. 43B). C6 and WT 4-NB presented lower diameters in comparison to control and H9.

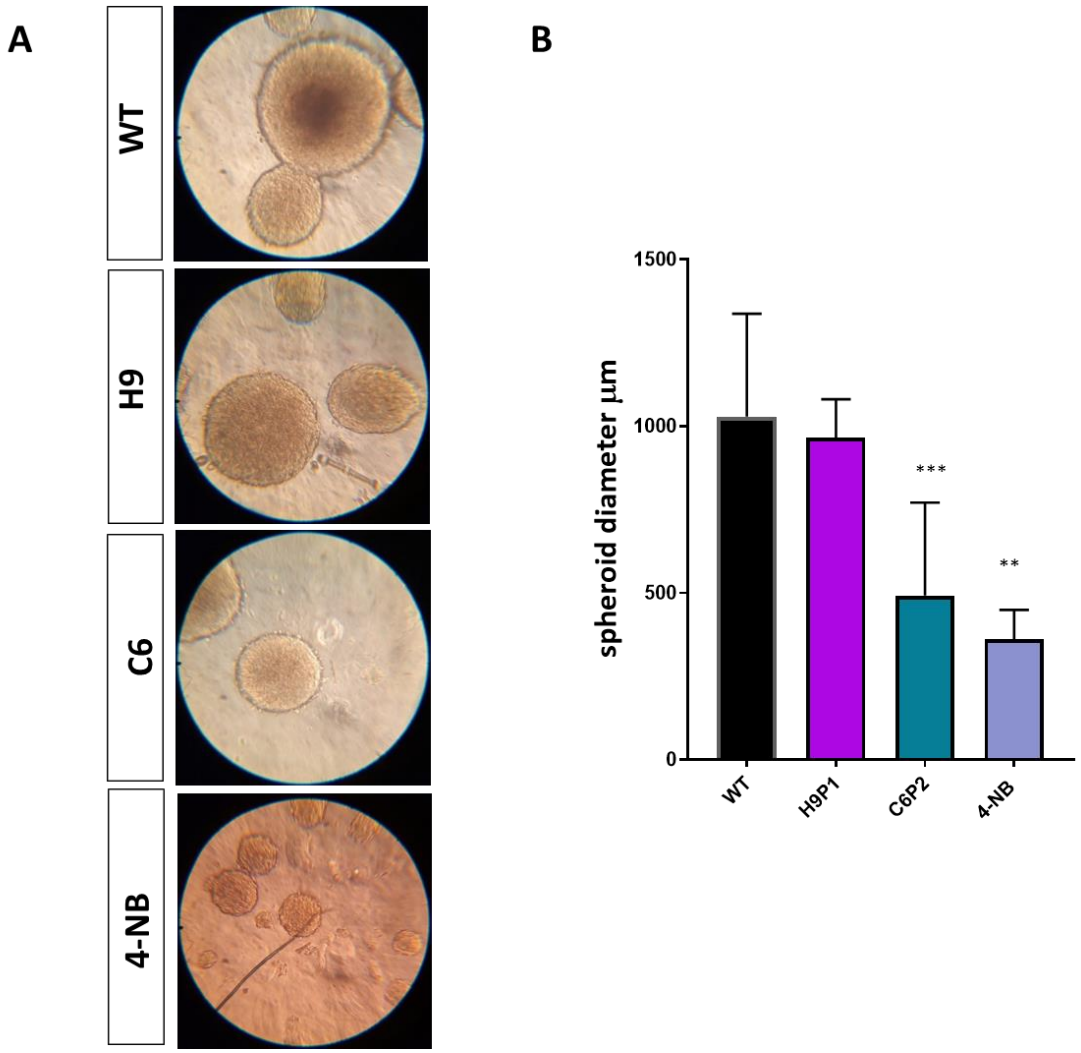

Figure 42 (**A**) Representative phase contrast light micrographs of spheroid.Cells were cultured in complete medium and complete medium with 4-NB (4-NB) in Bioinert Ibidi dishes with 25 % of Methocel to allow spheroids formation. (**B**) The diameter of the spheroid was measured after 14 days of seeding, using ImageJ software .

3.3.5 CoQ_{10} depletion affects cell metabolism

In attempt to investigate the metabolic and functional impact of COQ2 mutation, we evaluated oxidative phosphorylation by OCR and ATP quantification (Fig. 44A, D). OCR data suggested a severe respiration dysfunction in C6 mutant cell, insensitive to oligomycin and the uncoupler FCCP. ATP/ADP ratio was decreased in C6 and H9 cells.-Extracellular lactate measured by HPLC, show an increased and significative lactate secretion by C6 cell, reflecting an enhanced glycolytic metabolism (Fig. 44B). Since emerging studies .indicate that mTOR modulates energy consumption and mitochondrial functions [81], we performed WB of mTOR. We found lower expression in both mutants. (Fig. 44C). To understand if CoQ_{10} depletion was associated with cellular stress, we evaluated the expression of the mitochondrial chaperon GRP75. We found a slightly higher expression, not significative, of GRP75 in all mutants and 4-NB treated cells. (Fig. 44E).

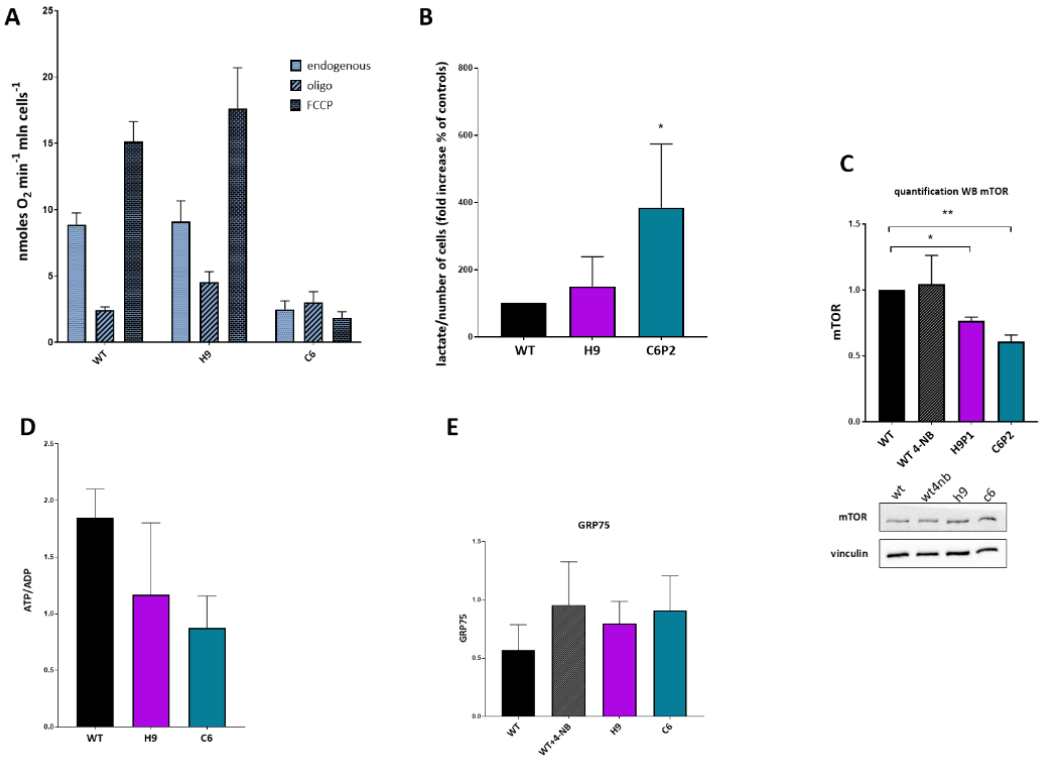

Figure 43 (**A**) Oxygen consumption rate (OCR) in intact cells measured in DMEM (basal respiration), in the presence of oligomycin A (Oligo) and carbonyl cyanide 4-(trifluoromethoxy) phenylhydrazone (FCCP). To inhibit the mitochondrial respiration, 2µM Antimycin A was added at the end of each experiment. (n = 3) (**B**) Lactate secretion determination in culture medium. Lactate was quantified by HPLC and the data were normalized on the number

of cells. (**C**) Quantification of mTOR performed by densitometry analysis, using vinculin as a loading control (n = 3). (**D**) Quantification of GRP75 performed by densitometry analysis, using vinculin as a loading control (n = 3).

To better estimate the reliance of mutant cells on glycolytic metabolism as an adaptive metabolic response, we used the fluorescent glucose derivative (2-NBDG) (Fig. 45A). The increased glucose uptake rate accounts for the glycolytic phenotype induced by CoQ depletion.

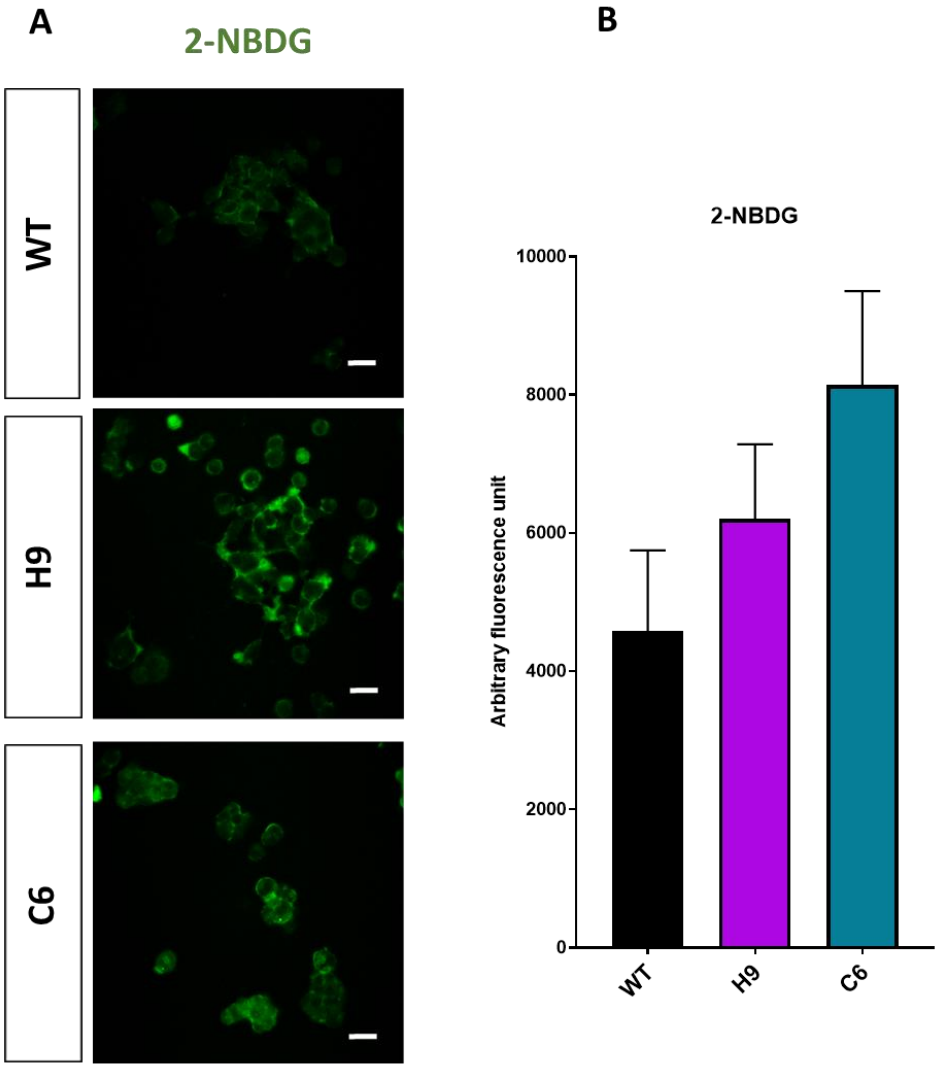

Figure 44 (**A**) Representative micrographs of the glucose fluorescent analogue 2-deoxy-2-[(7-nitro-2,1,3-benzoxadiazol-4-yl)amino]-D-glucose (2-NDBG) staining and .(**B**) their quantification Scale bar: 70 µm.

Since the mitochondrial transmembrane potential (ΔΨm) is a marker of functionality, we stained the cells with the fluorescent dye JC-1, previously described. Fig. 46 belove showed that a slight CoQ

depletion induced hyperpolarization (H9 cells), whereas a severe CoQ depletion (C6) decrease remarkably membrane potential.

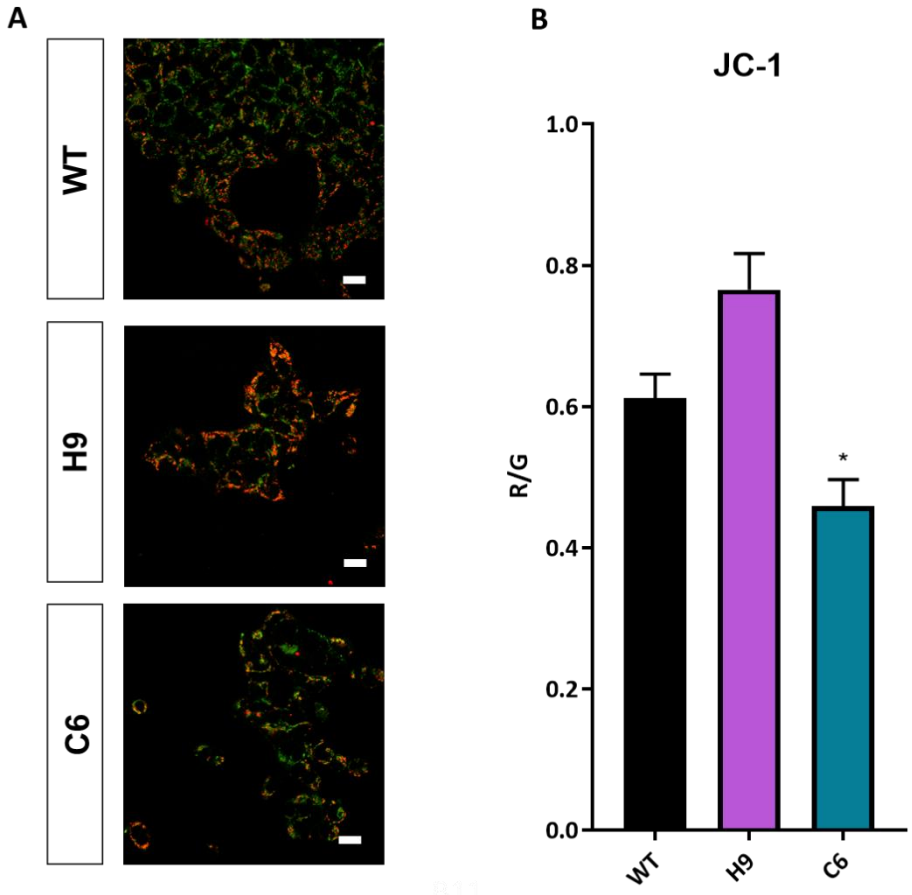

Figure 45 (**A**) Representative micrographs and their quantification (**B**) of wt and mutant cells stained with JC-1 dye. The mitochondrial potential was assessed by measuring the red on green fluorescence intensity ratio. Two randomly chosen fields, from three independent experiments, were analyzed for each condition. Scale bar: 70 µm. Statistical analysis was performed using GraphPad Prism software. Error bars indicate the standard error of the mean (SEM). P values were obtained using unpaired t-test with Welch's correction. *P ≤ 0.05.

3.3.6 HIF, BTP and cholesterol content

To estimate oxygen content in cell, we employed BTP probe, an iridium (III) complex dye. BTP signal is inversely proportional to the intracellular oxygen tension as the dye fluorescence emission is quenched by molecular oxygen. Since cells grown in three-dimensional spheroids could mirror in vivo metabolic response of the cell, we assessed oxygen content on monolayer cells and spheroids too. In

both cases we obtained similar results: BTP signal in H9 adhesive cell and in spheroids (Figure 47A, 48A), is higher in comparison to control (Fig. 47B, 48B) Since lower oxygen content could stabilize HIF-1α, a major key regulator of metabolism under many circumstances, we performed WB analysis of HIF-1α. We found a slightly higher expression in H9 cells compared to WT (Fig. 47C).

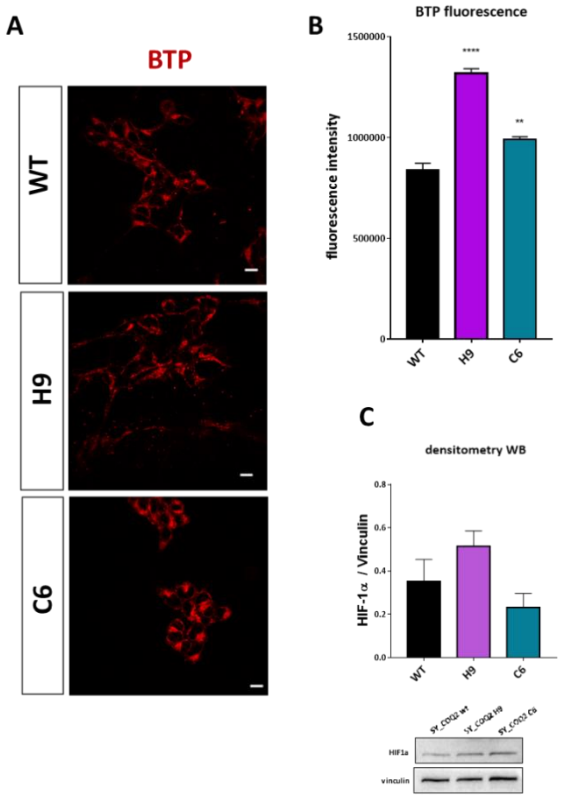

Figure 46 (**A**) Representative micrographs of BTP staining. Scale bar: 70 µm. (**B**) Quantification of fluorescence emission in cells stained with the dye bis (2-(2'-benzothienyl)-pyridinato-N, C30) iridium (acetylacetonate) (BTP). BTP is a live-cell O_2 sensor which fluorescence emission is quenched by molecular oxygen. Two randomly chosen fields, from three independent experiments, were analyzed for each condition. (**C**) Quantification of HIF-1α performed by densitometry analysis, using tubulin as a loading control (n = 3). Statistical analysis was performed using GraphPad Prism software. Error bars indicate the standard error of the mean (SEM). For comparison between multiple groups, P values were obtained using the analysis of variance (ANOVA) followed by Tukey's post hoc test. *P ≤ 0.05; **P ≤ 0.01.

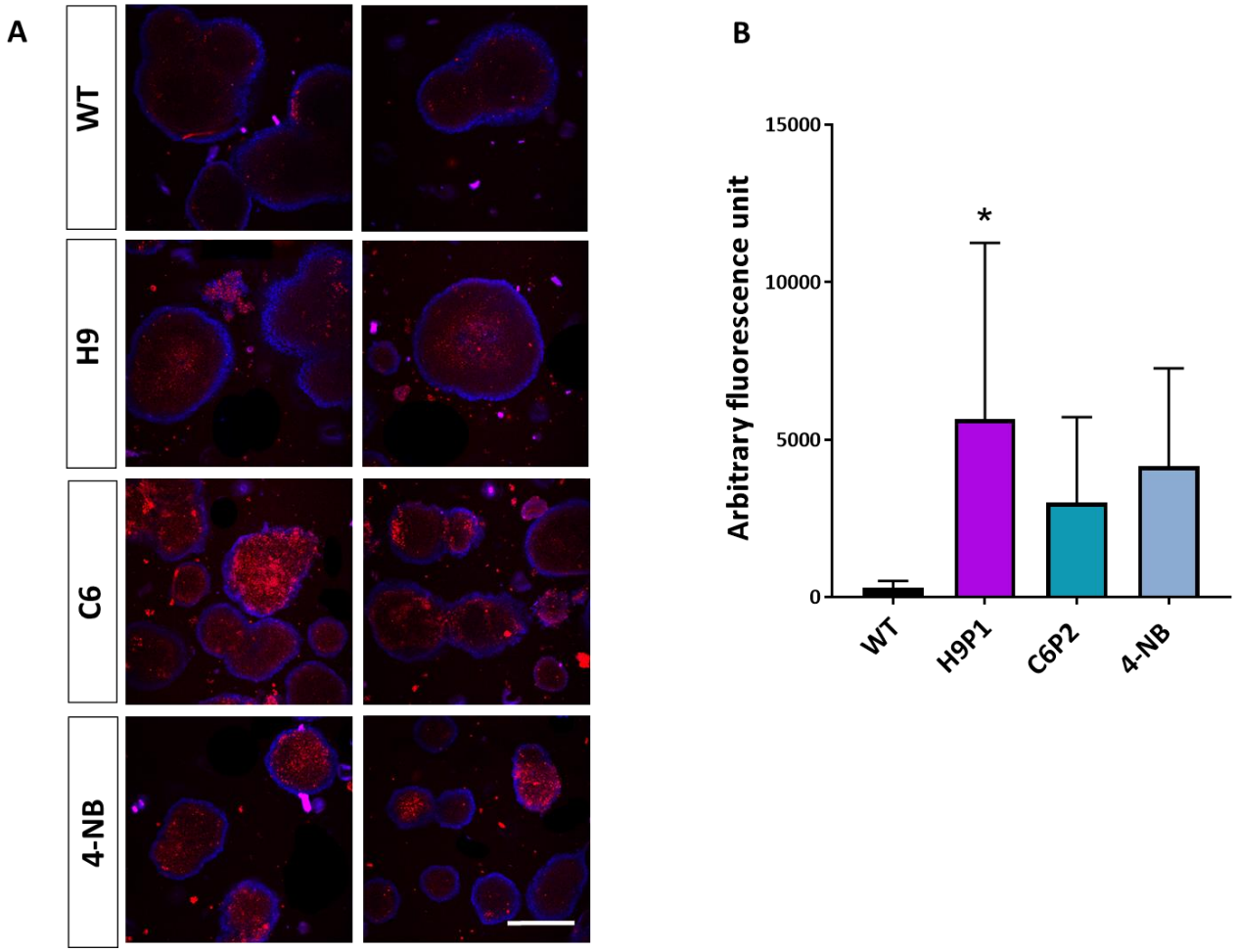

Figure 47 (**A**) Representative micrographs of control and CoQ-depleted spheroids stained with Hoechst and the oxygen sensitive probe BTP. Bar size = 100µm. (**B**) Quantification of BTP fluorescence emission in spheroid central sections. Error bars indicate SEM. For comparison between multiple groups, analysis of variance (ANOVA) was used followed by Tukey's post hoc test. *P ≤ 0.05; **P ≤ 0.01; ***P ≤ 0.001; ****P ≤ 0.0001.

As reported in T67 4-NB treated cell, CoQ_{10} depletion could increase cholesterol content. We investigate on cholesterol content by HPLC extraction but we did not detect any increase. (Fig. 49).

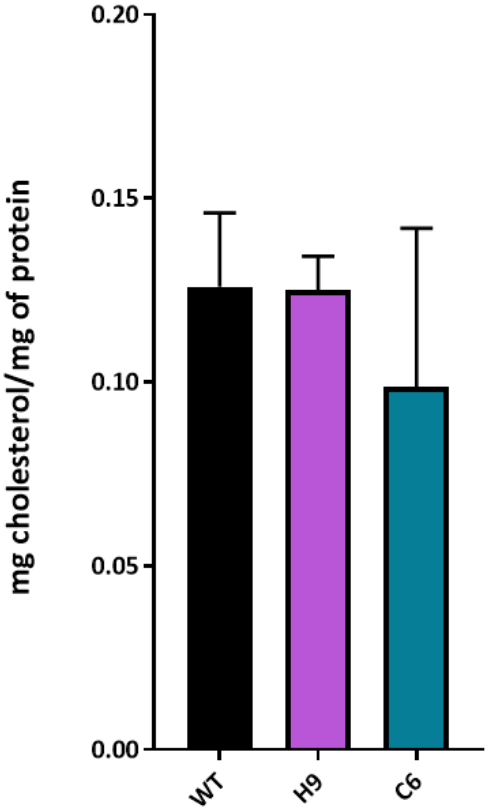

Figure 48 Total cholesterol content assessed by HPLC n lysates of WT, H9 and C6 cells.in lysates (n = 3).

3.3.7 Oxidative stress in COQ2 mutant cells

Considering CoQ antioxidant role, we investigated whether ROS production in SH-SY5Y cell lines was deranged by the COQ2 mutation using DCFDA, which measures intracellular reactive oxygen species and Mito-SOX Red, which selectively targets mitochondria and is oxidized by superoxide anion. (Fig.50A-B). Strikingly intracellular and mitochondrial ROS levels were significantly decreased in the mutant cells. Contrastingly Amplex Red staining, unable to cross the plasma-membrane, revealed an increase of oxidative stress in mutant cells. (Fig. 50C). To further investigate oxidative stress, we analysed lipid peroxidation too, using BODIPY. Under basal conditions, the ratiometric fluorescent lipid peroxidation sensor BODIPY, exhibited significative higher levels of oxidation in H9 cell, and slighter higher but not significative in C6 cell in comparison to control. (Fig.50D). To further analyse this trend, we performed RSL-3 titration on cells. RSL-3, an inhibitor of glutathione peroxidase 4

(GPX4), promoting ferroptotic death and accumulation of ROS [82]. We found higher resistance of mutant cells than control ones, demonstrated by the different values of RSL-3 IC50. (Fig. 50E). To understand whether these phenomena were due to alterations or possible variation of intracellular ROS detoxifying enzymes, we performed relative mRNA expression levels of SOD1 (mitochondrial Manganese Superoxide Dismutase 1), using GAPDH as endogenous reference. Despite there is a modest increase of SOD1 in H9 and a slight decrease in C6, there is no significant difference of mRNA expression (Fig. 50F).

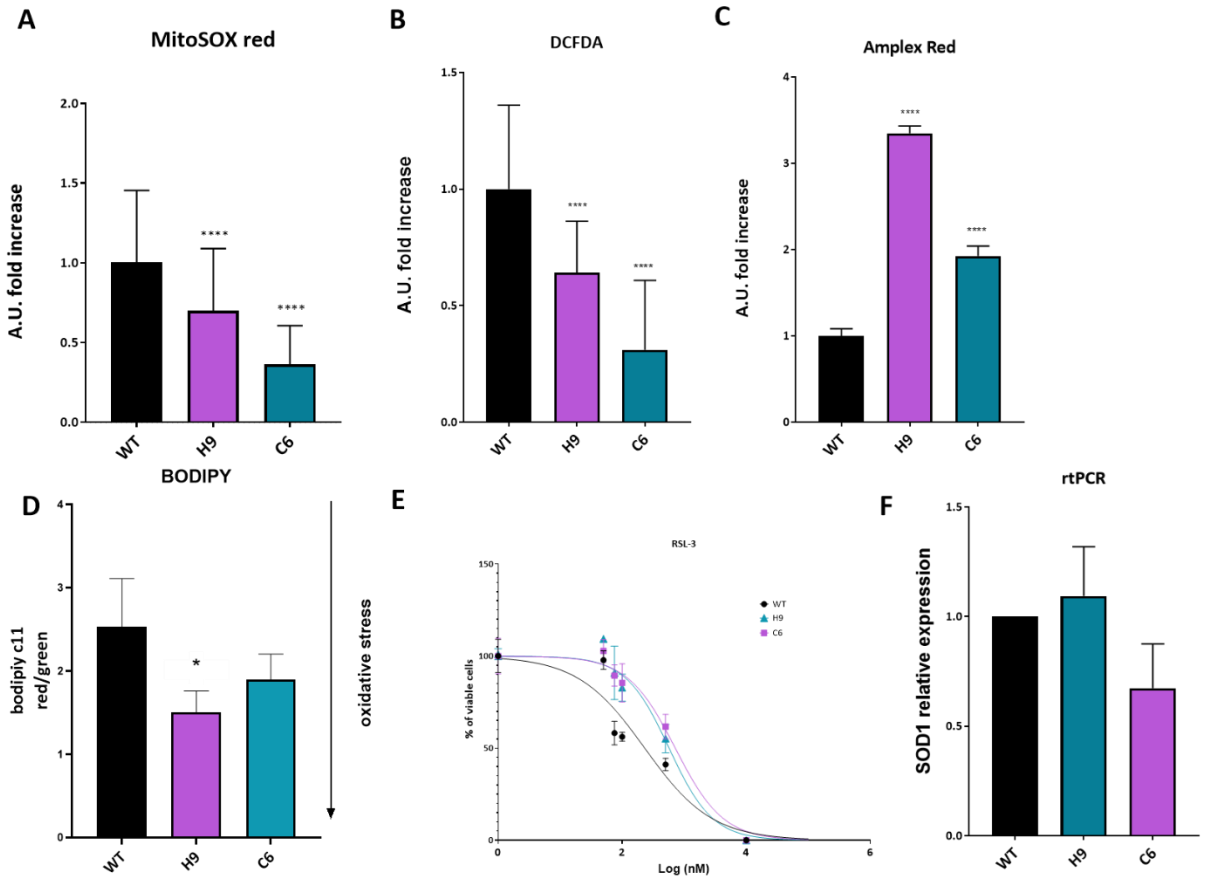

Figure 49 (**A**) mitochondrial superoxide production by using the mitochondrial specific probe MitoSOX Red, (**B**) dichlorofluorescin diacetate (DCFDA), (**C**) and Amplex Red Lipid peroxidation was assessud using BODIPY (**D**). Oxidative stress data were normalized on protein content. (**E**) Cells were cultured in complete medium for 24 hours in the presence of different concentrations of RSL-3. WT IC50: 231 nM, H9: 570 nM, C6: 717.5 nM.(**F**) SOD1 expression level was evaluated by real-time quantitative PCR in cells treated as above. The normalization was performed using TBP. Data are expressed as mean SD (n = 3). For comparison between multiple groups, analysis of variance (ANOVA) was used followed by Tukey's post hoc test. *P ≤ 0.05; **P ≤ 0.01; ***P ≤ 0.001; ****P ≤

0.0001. Error bars indicate SEM. For comparison between multiple groups, analysis of variance (ANOVA) was used followed by Tukey's post hoc test. *P ≤ 0.05; **P ≤ 0.01; ***P ≤ 0.001; ****P ≤ 0.0001.

3.3.8 SA-βgal activity X-GAL and lysosomes

The cell cycle profile (B) reveals an accumulation in G0-G1 of C6 line, reflecting the decreased proliferation rate already shown in growth rates section. To address this aspect, we analysed SA-βgal senescence activity (A). Both clones present a higher SA-βgal activity in comparison to control. In evidence Lysotracker staining (C) reflects this aspect, since H9 and C6 show a higher presence of lysosomes.

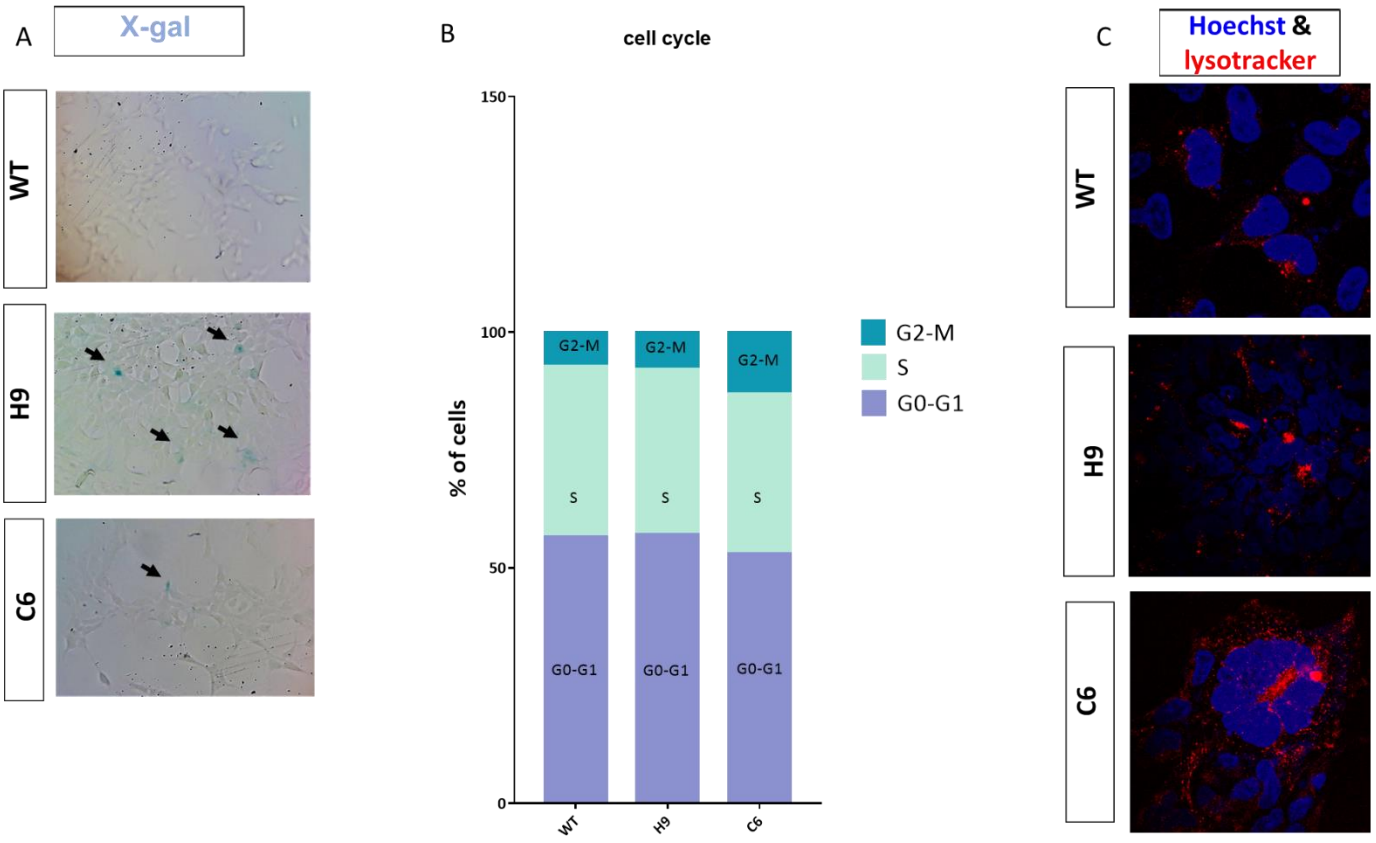

Figure 50 (**A**)Representatives micrographs of senescence-associated b-galactosidase chromogenic staining. (**B**) Cell cycle analysis by flow cytometry in control and CoQ depleted cells using propidium iodide dye staining. The column graph shows the percentage of cells in each cell cycle. (**C**) Representative micrographs of LysoTracker staining.

3.3.9 CoQ_{10} depletion and mitochondrial morphology

Under different growth conditions and metabolic stresses, mitochondrial morphology, regulated by fission, fusion, biogenesis and mitophagy events and dynamics, may change. Metabolic changes could lead to an increase or decrease in mitochondrial number and shape rearrangement. The evaluation of mitochondrial morphology was performed by confocal microscope imaging and MTG live cells staining. WT network morphology, well-organized and distributed around the nucleus and presented elongated mitochondria. H9 did not lose a mitochondrial network but presented more fragmented mitochondria than WT cells. By contrast, C6 cells displayed fragmented and disorganized mitochondrial network morphology and higher presence of balloon-like mitochondria Circularity and aspect ratio suggested us an increase round shape aspect of mitochondria in mutant cells in comparison to control. (Fig. 52B, C).

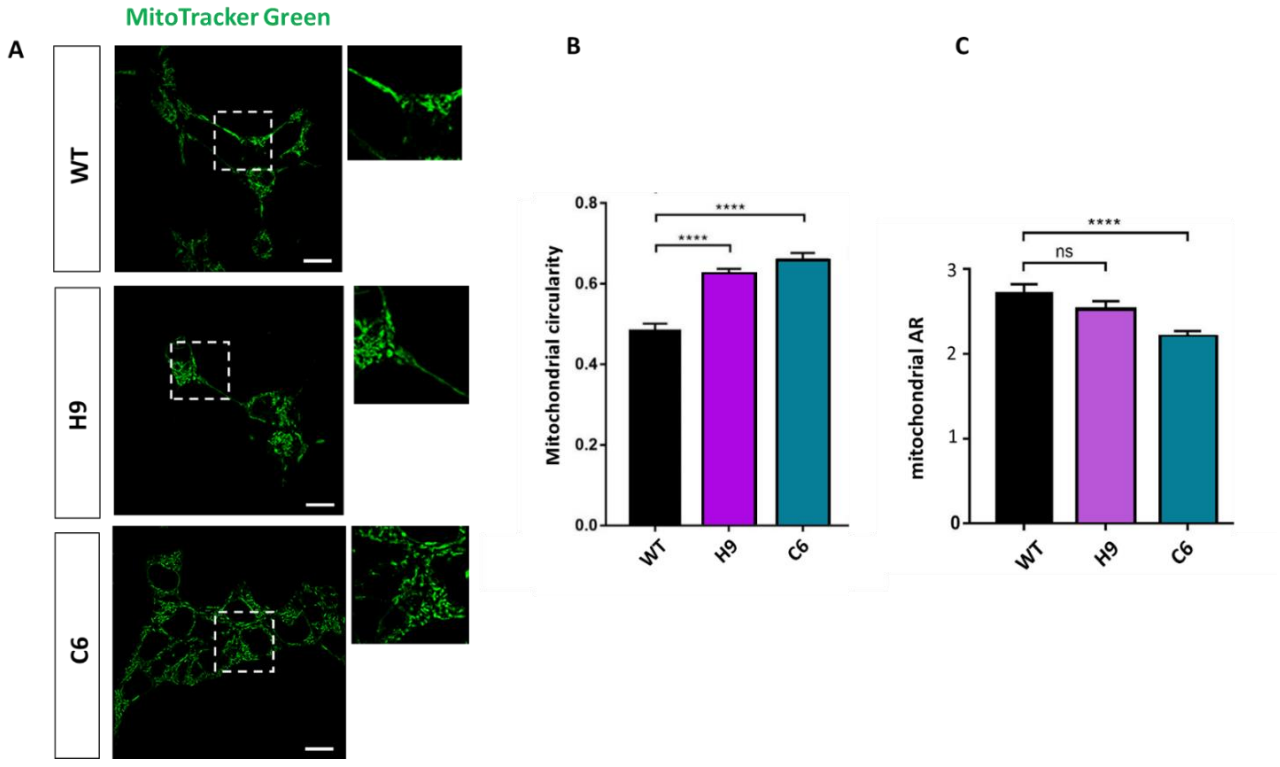

Figure 51 (A) Representative images of cells, stained with MTG (size bar = 10 µm, n = 3). Quantification of mitochondrial circularity (**B**) and aspect ratio (the ratio of the width to the height) (**C**) were performed using ImageJ tools. For each condition, at least two randomly chosen fields were analyzed. Data are expressed as mean SD (n = 3). For comparison between multiple groups, analysis of variance (ANOVA) was used followed by Tukey's post hoc test. *P ≤ 0.05; **P ≤ 0.01; ***P ≤ 0.001; ****P ≤ 0.0001. Error bars indicate SEM.

4 DISCUSSION

In this work we have generated cell lines CoQ_{10} depleted using a pharmacological and a genome editing approach, targeting one of the essential enzymes of its biosynthesis. Despite we are aware that both models have some limitations, our work highlights and embrace a different aspect of CoQ_{10} deficiency.

4.1 Coenzyme Q biosynthesis induces HIF-1α stabilization and metabolic switch toward glycolysis in T-67 cell

In the first part of the thesis, it has been reported a detailed characterization of coq2 inhibition effects in 4-NB-treated T67 cells. We reveal that CoQ biosynthesis inhibition induces several effects accountable for the deviation of FPP pool toward cholesterol biosynthesis. Results show that HIF-1α stabilization in T67 CoQ-depleted cells is strictly correlated with the cholesterol content since the depletion of membrane cholesterol through CD treatment reduces HIF-1α level. Since CoQ and cholesterol share part of their biosynthetic pathway, inhibition of the mitochondrial prenyltransferase coq2 could can possibly affect the cellular cholesterol content [83] [84] It has been demonstrated here that the inhibition of coq2 significantly increased the cholesterol level in comparison with controls Other studies reported similar results. Accordingly Liu et al.[85] have previously described that knock-down of UBIAD1, a non-mitochondrial prenyltransferase able to synthesize CoQ in the Golgi, induces an increase in intracellular cholesterol amount. Moreover, Suarez-Rivero et al. [86] reported that in fibroblasts from familial hypercholesterolemia patients, the mevalonate pathway was dysregulated, resulting in increased cholesterol levels and CoQ deficiency. We have also reported considerable changes in the physicochemical properties of the plasma membrane led by an increase in cellular cholesterol due to coq2 inhibition, as indicated by the increase in the anisotropy value of the fluorescent probe TMA-DPH and the order parameter (S)

calculated using the spin-label probe 5-DPC (Fig. 8D, E), displaying a reduced plasma membrane fluidity. In addition, considering that enzymes involved in cholesterol biosynthesis required oxygen [87], its activation can be responsible for the decreased level of oxygen content detected in 4-NB-treated cells. However, excessive cholesterol production is balanced by the stabilization of HIF-1α, able to inhibit the HMG CoA reductase [88]. To further investigate the direct relationship between increased cholesterol and intracellular hypoxia induced by 4-NB, we employed cyclodextrins to removed plasma membrane cholesterol. The cyclodextrin treatment decreased both the BTP signal and HIF-1α levels, indicating a recovery of the intracellular oxygen to control levels. From the BTP fluorescence calibration, it was possible to estimate a 50% reduction in the oxygen content in 4-NB-treated cells in comparison with controls. Even though such a decrease is not so strong to justify the occurrence of a hypoxic status, it is intriguing nonetheless, especially considering that the intracellular oxygen level is inversely correlated with the mitochondrial OCR, as Higuchi and colleagues have reported.[89 90]. The intracellular oxygen level depends on several factors, including its low diffusion coefficient in water [91 92]. Moreover, its diffusion through the plasma membrane is favoured by the mobility of the acyl chains of the phospholipids, which can be reduced by an increase of cholesterol content [93]. Assuming this, we can hypothesize that cholesterol might influence intracellular oxygen delivery. Considering also that CoQ is also an important intracellular antioxidant, it is possible to predict that its depletion can alter the cellular ROS homeostasis [93 94]. In 4-NB-treated cells, we found an increased ROS production that was rescued by CoQ supplementation. Duberley et al.[95]reported similar results obtained in SH-SY5Y cells, using para-aminobenzoic acid to inhibit ubiquinone biosynthesis. Intracellular content of NO was also enhanced by CoQ depletion. Strikingly, NO is a signalling molecule involved in response to hypoxia since HIF-1α can be S-nitrosylated at Cys533 in the oxygen-dependent degradation domain, preventing its degradation [96]. Besides, prolyl hydroxylases (PHD), responsible for HIF-1α degradation, are inactivaed once nitrosylated, further

stabilizing HIF-1α [71] [97]. Increased cholesterol was previously described as a promoter of HIF-1α accumulation by upregulation of NO production and inhibition of HIF-1α degradation [70].On the other hand, through ERK and PI3K/AKT signalling pathways, the expression of HIF-1 alpha can be subjected to transcriptional/translation regulation.[73].Despite this, we failed to identify any variations in the HIF-1α gene expression level in control and 4-NB-treated cells by qRT–PCR analysis (Fig. 10), supporting the hypothesis that HIF-1α accumulation is mainly due to a post-transcriptional stabilization. This transcription factor, once present in the cytosol, enters the nucleus where it binds to the hypoxia response elements, fostering the coordinate expression of genes triggering the glycolytic shift [71] [72] [98], thus adapting cell metabolism to O_2 deprivation. Following this notion, we reported that the rate of glucose uptake was higher in 4-NB-treated cells compared with controls. In this scenario, the HIF-1 alpha-driven metabolic transition to glycolysis has the double benefit to increase the glycolytic production of ATP and to reduce the electron flux through the respiratory complexes in order to defend cells against ROS overproduction [99] [100]. The increased accumulation of lipid droplets found in 4-NB-treated compared with 4- NB-untreated cells (Fig. 15) is consistent with the finding that HIF-1α can perturb lipid metabolism, fostering the storage of triglycerol into lipid droplets [101] [102] [103]. Remarkably, a switch to glycolytic metabolism leads to the accumulation of reducing equivalents, mostly due to the decreased NADH oxidation by mitochondria. Cells are provided with a PMOR that acts as a regulator of the intracellular reducing power due to its NAD+ regeneration capacity, and it is involved in the survival of cells with damaged mitochondria. [104] PMOR is composed of a transmembrane NAD(P)H dehydrogenase connected to a plasma membrane oxidase through a CoQ molecule [105] [106]. Mitochondrial impairment and oxidative stress stimulate CoQ-dependent oxidase activity. [107] [108]. In 4-NB-treated cells, an increased NAD(P)H content and plasma membrane NADH-FeCN activity have been observed, suggesting overexpression of the PMOR system [68]. It is possible that, because of CoQ depletion, the PMOR oxidase system in cells treated with 4-NB (Fig. 13B) did

not work at the maximum rate. Indeed, the enzyme efficiency in cells co-treated with 4-NB and Q (assessed by the ratio of PMOR oxidase to NADH-FeCN oxidoreductase activity) is threefold higher than that assessed in cells treated with 4-NB alone. In line with previous studies [41], 4-NB-treated cells retained their ΔΨm. Furthermore, we revealed that the ΔΨm of intact CoQ-depleted cells was not sensitive to oligomycin A treatment and poorly responsive to FCCP. The lack of sensitivity to oligomycin A was not ascribable to an uncoupling impact of CoQ depletion, as demonstrated by the respiratory rates shown in Fig. 1C. In addition, the lack of a depolarizing effect of oligomycin A indicates that the mitochondrial ΔμH was not due to the reverse activity of ATP synthase. Noticeably, the ΔΨm of CoQ-depleted cells permeabilized with digitonin was still sensitive to oligomycin A and FCCP (Fig. 14), prompting us to evaluate that the lack of sensitivity of ΔΨm to oligomycin A and FCCP was reversible and more related to the increased cholesterol content of the plasma membrane rather than mitochondrial CoQ depletion. A key feature of the metabolic adaptation to a mitochondrial impairment is the capacity of 4-NB-treated cells to retain the ΔΨm .[109].In the presence of a low respiration rate, the ΔΨm retention could be in accordance with an interruption of the backflow of H+ into the matrix, due to reduced activity of the ATP synthase. Several studies report that the ATP synthase is regulated in response to a metabolic change. In fact, the enzyme could be inhibited by oxidative stress and increased production of nitric oxide. Haynes et al. [110] showed that the nitration of two tyrosine residues in the β subunit of F1 part of the ATP synthase inhibited both the ATP hydrolase and synthase activities. On the other hand, it has been described a direct correlation between HIF-1α and the expression level of the ATPase inhibitor protein (IF-1) involved in the inhibition of both synthase and hydrolase activities [111]. In this regard, the high oxidative stress and nitric oxide production detected in 4-NBtreated cells may be relevant.

CoQ depletion perturbs the mitochondrial network morphology toward increased fragmentation, in agreement with data reported in COQ2 mutant cells [112] and siCOQ2-treated cells [113]; despite this, the

relationship between CoQ and the network morphology is still elusive. By determining the level of mitochondrial shaping proteins in 4- NB-treated cells, we could identify OPA1 as the only protein undergoing significant reduction, with an unbalance toward the long forms (Fig. 7 C,D). This result is unexpected because cell stress or energetic impairment generally causes unbalance toward the OPA1 short forms [115]. Nonetheless, this effect may depend on the reduction in intracellular oxygen and expression of hypoxia-induced gene domain protein-1a (Higd-1a), a protein able to bind to OPA1 and completely inhibit its cleavage [116].

In conclusion, as represented in Fig. 53, major findings have been summarized, showing how inhibition of coq2, while decreasing the amount of CoQ, redirect the farnesyl pyrophosphate pool toward cholesterol biosynthesis, thus reducing the plasma membrane fluidity. Consequently, the intracellular oxygen content is lowered, probably also due to increased consumption of oxygen required for the biosynthesis of cholesterol [117]. The reduced intracellular oxygen tension, combined with increased ROS/NO production, in turn, stabilizes HIF-1α, which mediates metabolic rewiring, by stimulating the glycolytic pathway to counteract the mitochondrial impairment due to the bioenergetic failure. Accordingly cell viability is maintained and overproduction of mitochondrial ROS is reduced. CoQ supplementation in 4-NB treated cells is not able to restore the intracellular oxygen to control levels and therefore does not fully recover neither mitochondrial function nor network fragmentation. Previous data reported in another model of CoQ depletion obtained in neuroblastoma cells reported a lack of effectiveness of CoQ treatment for restoring mitochondrial activities [118] [119]. Nevertheless, CoQ supplementation can restore the energy charge of the cell by stimulating the PMOR system (Fig 6D).

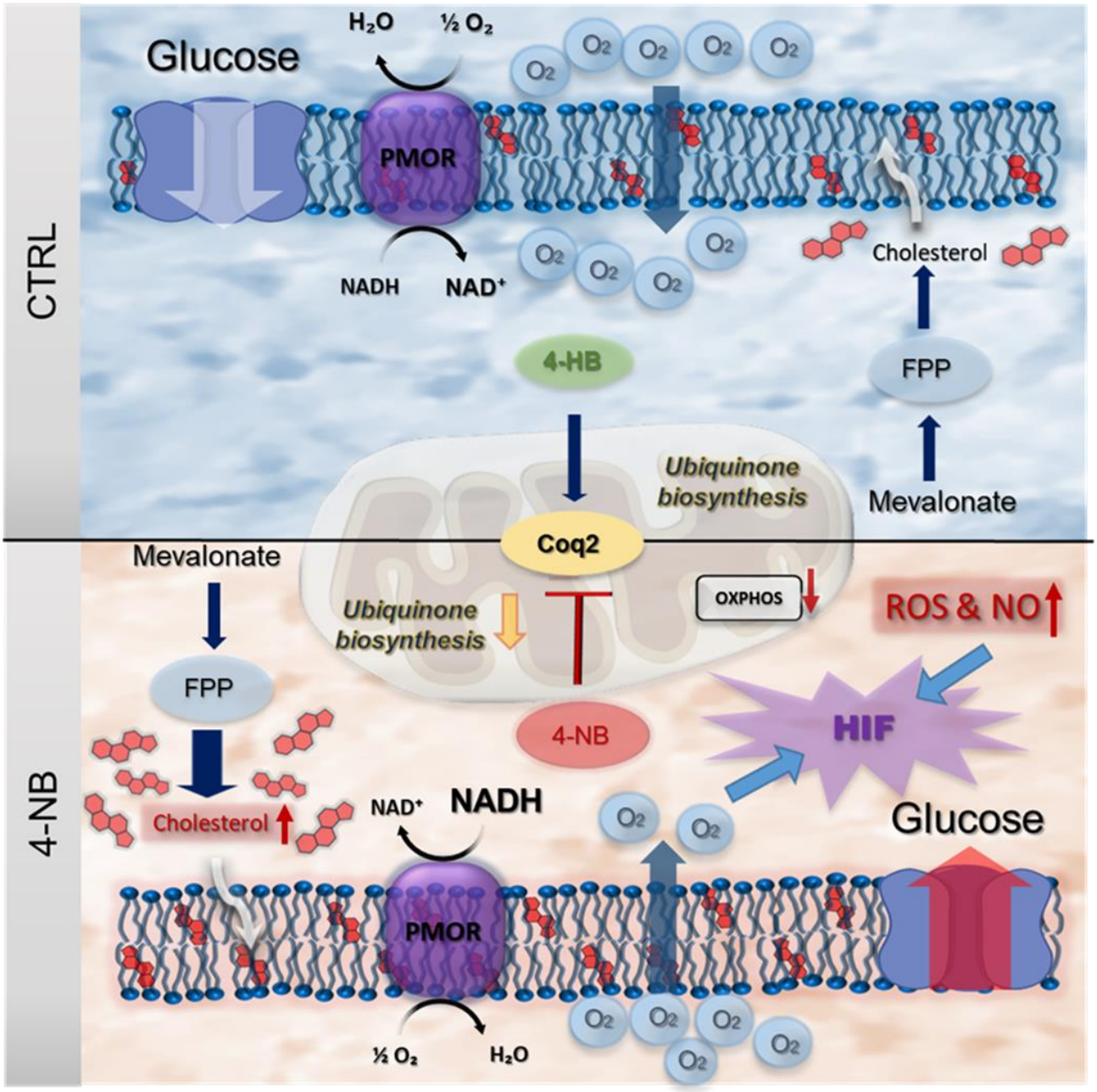

Figure 52 Schematic representation of differences between control and T67 4-NB treated cells. **Normal cells (CTRL)**: CoQ and cholesterol levels are maintained through the activities of the mevalonate pathway and the CoQ biosynthetic complex. The normal ratio of cholesterol and CoQ content in the plasma membrane allows oxygen to diffuse into the cytosol favouring an oxidative metabolic phenotype. Moreover, the antioxidant properties of CoQ counteract oxidative stress. **CoQ depleted cells (4-NB)**: the inhibition of Coq2 by 4-nitrobenzoate (4-NB) causes a reduction by 50-60% of the total CoQ content and leaves the farnesyl pyrophosphate (FPP) pool available for cholesterol biosynthesis. Total cholesterol content is increased by 30% and causes a reduction in plasma membrane fluidity, resulting in lower oxygen uptake. The hypoxic state stabilizes HIF-1α, which mediates the adaptive metabolic response by stimulating the glycolytic pathway. CoQ depletion reduces OxPhos activity and antioxidant cellular defenses. [120]

4.2 Coenzyme Q depletion reshapes MCF-7 cells metabolism

In the second part of the results, the effects of mitochondrial impairment, induced by CoQ_{10} depletion, in a human breast cancer cell line (MCF-7), have been reported. Since investigating one cell line could be a great limitation, find possible comparisons and common patterns with an additional cell line could provide further insights on CoQ_{10} deficiency. Thus, we tried to translate the previous research approach adopted on T67 cell line, on a cell breast cancer model. Since MCF-7 cell is commonly used as a in vitro model to study breast cancer, in this part we emphasise all those aspects concerning cancer metabolism too. Cancer cells metabolism represents a critical challenge and plays critical roles in tumour progression, metastasis and resistance to a different type of therapies. Moreover, tumorigenesis is often associated with mitochondrial dysfunction, which could mirror not only metabolism plasticity but an altered interaction with different cell organelles or structures too. Furthermore, analysing the bioenergetics profile of CoQ depleted MCF-7 cells, allow us to confirm a presence of reduced oxygen consumption rate, especially in the uncoupled state, increased membrane potential (Ψm), increased level of ROS, and altered mitochondrial morphology The mitochondrial dysfunction was induced by inhibiting the biosynthesis of CoQ using 4-nitrobenzoate (4-NB), an inhibitor of the biosynthetic enzyme coq2. [40]

As previously described, CoQ is a lipid-soluble molecule present in all cell membranes and of the most important function is its role as an electrons transfer in the mitochondrial respiratory chain and the antioxidant activity. In the previous results section, CoQ depletion induces in T67 cells alterations on respiratory capacity and redox state, which are associated with an increased level of cholesterol and decreased level of intracellular oxygen content. All these factors contribute to transcription factor HIF-1α stabilization, a key regulator for metabolic rearrangement necessary to allow cell survival in OXPHOS impaired condition. In this contest we analyzed the bioenergetic

profile of CoQ depleted MCF-7 cells, reporting the presence of reduced oxygen consumption rate, especially in the uncoupled state, increased membrane potential (mtΔψ), increased level of ROS, and altered mitochondrial morphology. Further analysis of the respiratory chain activity showed that Complex I activity was not affected, while complex II and complex IV activities were significantly reduced (Fig. 20B, C, D). CoQ acts as substrate only for Complex I and II, thus the decreased activity of Complex IV could be linked to enzyme damage induced by increased oxidative stress, as reported in section 3.1.6. A lowered succinate dehydrogenase activity in mitochondria with high transmembrane potential is a well-known phenomenon due to oxaloacetate inhibition, as recently elucidated by Fink B.D. et al.[121]. In CoQ depleted cells, the intracellular oxygen level was lower than controls, despite their reduced oxygen consumption rate (Fig. 20A). Moreover, the total cholesterol content and the ROS production were increased, while the antioxidant defences, evaluated as reduced glutathione content, were decreased (Fig. 25 A, B). These data suggested a metabolic change in cellular metabolism and HIF-1α stabilization, concomitantly with a switch toward glycolysis. Since HIF-1α can be destabilized bY high levels of α-ketoglutarate, cells were supplemented with a membrane-permeable derivative of this compound (TαKG), showing that CoQ depleted cells viability was significantly affected (Fig. 31E). Interestingly, the activity of the respiratory complex II can directly affect HIF-1α, since succinate inhibits the prolyl-hydroxylase domain enzymes (PHDs) activity, leading to HIF-1α stabilization under normoxic conditions [122] [123]. Noticeably, MCF-7 cells treated with 4-NB showed a 50% decrease in complex II activity, suggesting that its impairment could be significant in the metabolic reprogramming in cells with mitochondrial dysfunction (Fig. 20C). It is reported that cancer cells support their energetic and biosynthetic demands mostly by glycolysis [48]. To test on what extent CoQ-depleted cells rely on glycolysis, the glucose in the culture medium was replaced with galactose [124][125], finding that galactose treatment significantly decreased their growth rate in comparison with controls. (Fig. 31B). Nevertheless, in

the presence of glucose, the glycolytic metabolic switch can efficiently compensate for the lack of energy due to OXPHOS impairment. As a matter of fact, the total energetic charge of CoQ-depleted cells in the presence of glucose was similar to controls. (Fig. 26A). CoQ depleted cells reported a higher glucose uptake associated with a higher expression of glucose transporters Glut 1 and Glut 3 in comparison with controls. (Fig. 28A, B, C). Strikingly, CoQ-depleted cells showed a lower basal lactate secretion rate, despite the glycolytic metabolism. To further address this point, we measured the lactate secretion induced by ATP synthase inhibition, using oligomycin A. The cells with functional mitochondria respond to oligomycin A inhibition with a strong increase in lactate secretion, whereas cells with defective mitochondria, had lactate secretion under oligomycin stimulation low [48]. In MCF-7 cells treated with 4-NB, the release of lactate induced by oligomycin A was lower in comparison to control cells, confirming their glycolytic metabolism. (Fig. 29 A,B). The activation/inactivation of enzymes of several metabolic pathways is involved in the metabolic rearrangement induced by CoQ depletion. For instance, pyruvate kinase showed decreased Km (for phosphoenolpyruvate (PEP), suggesting an allosteric activation. (Fig. 29C,D). On the other hand, the expression of pyruvate dehydrogenase was unaffected, while the lactate dehydrogenase was increased; these modifications are consistent with increased glycolytic flux, without a concomitant enhancement of the oxidative degradation of pyruvate.(Fig. 30A). In CoQ depleted cells, pyruvate could be partially redirected toward biosynthetic pathways, as suggested by the low lactate secretion rate and the increased activity of LDH. This evaluation requires further experiment. Analyzing the activities of Krebs's cycle enzymes, we found increased activities of glutaminase, isocitrate dehydrogenase isoforms, and malate dehydrogenase, as well as the malic enzyme. Since CoQ depletion strongly reduces the OXPHOS activity, increased activity of these enzymes could be explained by considering a reductive metabolism of glutamine, as recently reported by Chen et al.[126]. The stimulation of the reductive carboxylation of α-ketoglutarate derived from glutamine

allows cells to provide intermediates for the biosynthetic pathways. (Fig. 30A). Notably, normal and CoQ depleted cells are equally sensitive to glutamine deprivation (Fig. 31D), probably due to the lower proliferation rate of 4-NB treated cells. Considering the low proliferation rate measured in CoQ-depleted cells, the cell cycle analysis of CoQ-depleted cells, indicated a cell accumulation in G0/G1-phase and a decreased cell number in S-phase (Fig. 30B,C).

Taking into account that two-dimensional systems cannot always provide a complex and dynamic microenvironment for cells, we performed some experiments in three-dimensional cell line, considering that spheroids could mirror in vivo metabolic response of the cell.

Spheroid characteristics may also vary remarkingly with the origin and type of cell line- In particular, it is easier to obtain spheroid with some cell lines responding to specific shape and morphology requirements. Among these cells, MCF-7 are the most used and represent the most reproducible 3-D model. [52] Furthermore, Gomes A. et al. recently have been reported how the physiological oxygen concentration could deeply affect cell growth in 3D culture systems, mimicking 3D tumour growth. In particular, different oxygen concentrations could critically affect spheroid growth. Remarkably, the oxygen reduction affects only 3D spheroids growth and has almost no effect on the 2D cell culture. These effects are induced by an oxygen concentration of 5%, which is not considered a hypoxic condition. [78] Since we found that CoQ depleted 2 D cells were characterized by a lower intracellular oxygen concentration and HIF-1α stabilization (Fig. 26B, C) as reported in T67 too, we analyzed the ability of CoQ depleted and control cells to form 3D structure. The results reported (Fig. 33 A,B) demonstrated that the spheroids dimensions were similar until day 8-10. After this time, 3D spheroids derived from control cells increased their size, while spheroids derived from CoQ-depleted cells stopped their growth. Moreover, we found that oxygen distribution inside spheroids was different: spheroids derived from control cells presented a hypoxic core, while in spheroids derived from CoQ-depleted cells the hypoxic region was extended up to the outer layer of the structure (Fig.

34 A, B). These results confirm the role of intracellular oxygen concentration as a major rate-limiting factor for cell proliferation rate. It is known that hypoxia contributes to tumour resistance to radio and chemo-therapy: here we reported that CoQ-depleted MCF-7 cells were more resistant to doxorubicin (Fig. 32A). A recent study has pointed out that increased mitochondrial cholesterol can contribute to chemotherapy resistance[127]. Thus, it is likely that elevated cholesterol reduced susceptibility to doxorubicin in cancer cells treated with 4-NB. It is also plausible that deregulation of the intrinsic apoptosis pathway may account for this resistance.[128] In contrast CoQ depleted cells are not sensitized by cisplatin treatment (Fig. 32B). The mechanisms of cellular uptake and toxicity of the anticancer drug cisplatin mechanism of cisplatin are quite complex and involve different signalling pathways that can be classified in a cytoplasmic and in a nuclear module. To become active cisplatin has to undergo a series of reactions that consist of the substitution of one or both cis-chloro groups with water molecules. These reactions occur in the cytoplasm and derived forms of cisplatin are susceptible to react with different nucleophiles substrates such as reduced glutathione (GSH). In this contest, GSH can act as cisplatin scavenger inducing the so-called pre-target resistance. In CoQ depleted cells we have found reduced levels of GSH (Fig. 25A): it is conceivable to suppose that the similar IC50 for cisplatin found in control and 4-NB treated cells is the result of a balancing of the amount of the active forms of this drug. Nevertheless, further experiments are needed to address this point. In conclusion, CoQ-depleted cells showed a decreased proliferation rate, an increased sensitivity to oxidative stress injury and energy reliance on glycolysis. Moreover, CoQ-depleted cells showed a low intracellular oxygen concentration, which hinders the formation of 3D spheroids.

These results shed light on the mechanisms of tumour metabolic reprogramming provided an insightful understanding of cancer metabolism targeting. Data resulted from both cell lines converge on mitochondrial dysfunction as a hallmark of CoQ_{10} depletion obtained by 4-NB treatment,

confirming that the cellular model could recapitulate some mitochondrial dynamics-associated parameters in the main phenotypic manifestation of the CoQ_{10} deficiency.

4.3 CoQ_{10} depletion induced in SH-SY5Y cells by targeting COQ2 by CRISPR-Cas9 genetic editing

In the third part of the thesis, we have reported the results that describe the effect of a mutation on the COQ2 gene in terms of residual CoQ_{10} content and bioenergetics characteristics. The mutation was achieved by the Crispr-Cas9 technology on a human neuronal cell line: SH-SY5Y. Since one of the most important pathological effects observed in patients affected by primary CoQ deficiency is cerebellar ataxia with brain degeneration [129], we decided to exploit a neuronal cell line. Among the different clones obtained treating the SH-SY5Y cell line with the CRISPR-Cas9 technology, we have chosen two mutated clones: one with the heterozygote mutation (H9 clone) and the other presenting the homozygote mutation (C6 clone) a third clone that did not present any mutation on the COQ2 gene was taken as control (wild type clone). (Fig. 36). All these clones were genetically analysed to characterize the kind of mutation.

Both H9 and C6 clones presented a lower proliferation rate in high glucose medium, in particular, the proliferation rate of the homozygote clone was strongly inhibited. Uridine supplementation was able to rescue the proliferation rate of both clones in high glucose while substituting glucose with galactose or 2-DG in culture medium we observed a lower proliferation rate for the H9 clone and strong inhibition of the long-term proliferation (48-72 hours) for the C6 clone. The strong impaired proliferative capacity (Fig. 44) probably linked to high senescence, confirmed by enhanced X-Gal

activity, and a reduction in the proportion of cycling cells (Fig. 50) reflecting ulteriorly the involvement of CoQ_{10} in pyrimidine synthesis.

These results confirm the strong glycolytic metabolism of the CoQ depleted cells and the crucial role of CoQ in the pyrimidine biosynthesis that are essential for cell replication. On the other hand, exogenous CoQ enrichment of the culture medium did not improve cell proliferation. This last observation rises the question about the possibility that exogenous CoQ could reach the inner mitochondrial membrane substituting the endogenous one.

To further characterize the cell proliferation, we also evaluated the generation of spheroids. The spheroid structure is driven by nutrient and signal gradients, therefore metabolic impairment could deeply affect spheroid rearrangement and formation. [130] C6 spheroid growth recapitulates cell monolayer growth. Different cell lines started aggregating at 24 hours and formed spheroids at 48 hours After 14 days WT and H9 cell formed more condensed and bigger spheroid (Figure 43), maybe due to a higher proliferation rate and a lower cell death. In contrast, C6 and 4-NB SH-SY5Y treated cells form smaller spheroids. 4-NB treated cells, in this case, have similar characteristic to C6, considering the time-dependent effect of 4-NB, as previously described. In fact, in this experiment cells were treated with 4-NB for two weeks, whereas for the other experiments performed in 4-NB described previously, there was a 4-days treatment.

According to the previous results obtained in T67 and MCF7 cell, we found that the heterozygote clone preserved 50% of the original CoQ_{10} content, whereas in the homozygote the CoQ content was under the limit of detectability of the HPLC technique used for its determination. Based on the detection limit of our HPLC system we can speculate that the residual CoQ content in C6 clone is under the 5% of the wild type. According to the almost complete lack of CoQ, the C6 showed a very low oxygen consumption rate insensitive to oligomycin and FCCP. On the other hand, H9 clone despite the 50% of reduction in the total content of CoQ_{10} presented an oxygen consumption rate

congruent to that one measured in wild type cells. This result is not in line with the results obtained in T67 and MCF7 cell lines which showed a decreased oxygen consumption rate after 50% of CoQ depletion suggesting that different cell lines might exhibit different CoQ dependence of the mitochondrial respiratory chain activity.

Analysing the total intracellular oxygen content, HIF-1α stabilization, the cholesterol content and the ROS production associated with CoQ depletion we found that oxygen content was reduced in both clones according to the results described in the previous two sections, a slight HIF-1α stabilization was detected only in the heterozygote clone, (Fig. 47 B) while total cholesterol content (Fig. 49) and intracellular as well as the mitochondrial ROS production (Fig. 50) were decreased in both clones. Since the CoQ_{10} is considered a strong liposoluble antioxidant we have detected the level of lipid peroxidation in CoQ depleted clones using the lipid peroxidation sensor BODIPY: the results showed an increased lipid peroxidation in both clones in comparison with the wild type cell line. Moreover, using the non-permeable ROS probe Amplex Red we found an increased extracellular ROS production suggesting increased activity of the plasma membrane oxidase systems that are involved in the recovery of the intracellular redox status shuttling reducing equivalents from the cytosolic NAD(P)H to extracellular oxygen. Morphological mitochondrial alteration was found in CoQ depleted clones confirming the relation between morphology and mitochondria functionality. Although in our experimental conditions, the H9 and C6 clones showed a decreased intracellular ROS production (Fig. 50 A,B) we detected an increased lipid peroxidation (Fig. 50 D) in both clones confirming the oxidative stress status of CoQ depleted cells.

Despite the increased lipid peroxidation, we found that the two mutant clones presented higher resistance to RSL 3 treatment. Since RSL 3 inhibits GPX4 which role is to interrupt the lipid peroxidation chain reaction preserving membrane integrity and counteracting ferroptosis, [131] the increased resistance of mutated clones to RSL 3 is not easily explainable. This higher resistance could

be determined also by a possible increase of GPX4 nevertheless this point requires further analysis to be elucidated (Fig. 50D).

Reliance on glycolysis was confirmed not only by the growth rate in galactose and 2-DG, but also by 2-NBDG staining and lactate production. C6 and H9 shown a higher 2-NBDG uptake (Fig. 43A) and higher extracellular lactate levels (Fig. 42B) in comparison to WT cells. We also estimated oxygen content by BTP fluorescence. The higher BTP emission in the mutant cells in comparison to control (Fig. 47) suggested a reduction in intracellular oxygen, similarly with data obtained previously in MCF-7 and T 67 4-NB cells. Spheroids BTP emission recapitulates monolayer cells behaviour. In particular, to estimate oxygen content in 3-D cells, we analysed the spheroid core, using the central spheroid section obtaining by analysing different Z-stacks (Fig. 48B)

Since mTOR pathway signalling has been found a regulator of a multitude of extracellular signals and intracellular cues, including energy production in mitochondria,[132] we performed mTOR western blot. We found lower expression in both mutants, implying an adaptive metabolic response to cope with an impaired mitochondrial functionality. C6 shown a higher decrease than H9 in comparison to control. (Fig. 44).

In summary, our observations reveal the diverse biochemical consequences of CoQ_{10}, indicating that partial CoQ_{10} deficiency, shown in H9, does not affect the activity of the respiratory chain but affects other cellular functions, in accordance with data described previously in other CoQ_{10} depleted cell models (results I and II), like ATP production, metabolic switch toward glycolysis, intracellular oxygen content. On the other hand, a severe CoQ_{10} (C6) depletion, impair dramatically OCR, cell cycle, ATP production, membrane potential. To better estimate the extent of the impact of the loss of CoQ_{10} production on other aspects of cell metabolism and elucidate the lack of accordance with previous findings in T67 and MCF-7 further experiments should be addressed, taking into account that

different cell lines could rely on different metabolic needs and characteristics. These characteristics could make it difficult to completely understand some pathogenic mechanisms.

Despite these experimental limitations, assessing Q10 depletion effects on cell metabolism could provide insightful findings for the pathological mechanisms of CoQ_{10} deficiency lead by COQ2 mutations.

5 ABBREVIATIONS

4-HB p-hydroxybenzoic acid;

4-NB 4-nitrobenzoic acid;

5DPC 1-palmitoyl-2-stearoyl-(5-doxyl)-sn-glycero-3-phosphocholine;

ADP Adenosine diphosphate

AMP Adenosine monophosphate

ATP Adenosine triphosphate;

BTP bis(2-(2'-benzothienyl)-pyridinato-N,C3')iridium(acetylacetonate));

CoQ Coenzyme Q

CS citrate synthase; DAF-FM 4-Amino-5-methylamino-2',7'-difluorescein;

DCFDA 2',7'-Dichlorofluorescin diacetate;

EPR Electron Paramagnetic Resonance;

ETC Electron transport chain

FCCP Carbonyl cyanide 4-(trifluoromethoxy)phenylhydrazone;

FCCP Carbonyl cyanide 4-(trifluoromethoxy) phe-nylhydrazone

FPP farnesyl pyrophosphate;

GLUT1 Glucose Transporter Type 1

GLUT3 Glucose Transporter Type 1

HBSS Hank's balanced salt solution

Abbreviations

HEPES 4-(2-Hydroxyethyl)piperazine-1-ethanesulfonic acid, N-(2-Hydroxyethyl)piperazine-N'-(2-ethanesulfonic acid)

HMG-CoA 3-hydroxy-3-methyl-glutaryl-coenzyme A reductase;

IMM inner mitochondrial membrane;

KM Michaelis-Menten constant;

KRB Krebs-Ringer Bicarbonate Buffer (per esteso nei materiali e metodi);

MELAS Mitochondrial encephalomyopathy, lactic acidosis and stroke-like episodes;

LDH Lactate dehydrogenase

MDH malate dehydrogenase

ME Malic enzyme

mPTP mitochondrial transition permeability pore;

MTG MitoTracker Green;

NAD(P)H Nicotinamide adenine dinucleotide phosphate;

NADH Nicotinamide adenine dinucleotide reduced;

NAD^+ Nicotinamide adenine dinucleotide;

NO nitric oxide;

OCR oxygen consumption rate;

OCR Oxygen consumption rate

OXPHOS Oxidative phosphorylation;

PBS Phosphate-buffered saline;

Abbreviations

PDC Pyruvate dehydrogenase complex

PDSS2 decaprenyldiphosphate synthase subunit 2;

PEP Phosphoenolpyruvate

PK Pyruvate kinase

PMOR NADH-oxidase of the plasma membrane;

RCI respiratory control index;

ROS reactive oxygen species;

TMA-DPH 1-(4-Trimethylammoniumphenyl)-6-Phenyl-1,3,5-Hexatriene p-Toluenesulfonate;

TMPD N,N,N',N'-tetramethyl-p-phenylenediamine ;

TMRM tetramethyl rhodamine methyl ester

6 REFERENCES

1. Crane, F. L., Hatefi, Y., Lester, R. L. & Widmer, C. Isolation of a quinone from beef heart mitochondria. 1957. *Biochim. Biophys. Acta* **1000**, 362–363 (1989).

2. Turunen, M., Olsson, J. & Dallner, G. Metabolism and function of coenzyme Q. *Biochim. Biophys. Acta* **1660**, 171–199 (2004).

3. Dallner, G., Brismar, K., Chojnacki, T. & Swiezewska, E. Regulation of coenzyme Q biosynthesis and breakdown. *Biofactors* **18**, 11–22 (2003).

4. Romero-Moya, D. *et al.* Genetic Rescue of Mitochondrial and Skeletal Muscle Impairment in an Induced Pluripotent Stem Cells Model of Coenzyme Q10 Deficiency. *Stem Cells* **35**, 1687–1703 (2017).

5. Barros, M. H. *et al.* The Saccharomyces cerevisiae COQ10 gene encodes a START domain protein required for function of coenzyme Q in respiration. *J. Biol. Chem.* **280**, 42627–42635 (2005).

6. Wang, Y. & Hekimi, S. Molecular genetics of ubiquinone biosynthesis in animals. *Crit. Rev. Biochem. Mol. Biol.* **48**, 69–88 (2013).

7. Evans, D. R. & Guy, H. I. Mammalian pyrimidine biosynthesis: fresh insights into an ancient pathway. *J. Biol. Chem.* **279**, 33035–33038 (2004).

8. Fontaine, E., Ichas, F. & Bernardi, P. A ubiquinone-binding site regulates the mitochondrial permeability transition pore. *J. Biol. Chem.* **273**, 25734–25740 (1998).

9. Gille, L. & Nohl, H. The existence of a lysosomal redox chain and the role of ubiquinone. *Arch. Biochem. Biophys.* **375**, 347–354 (2000).

10. Maneesh, M. & Jayalekshmi, H. Role of reactive oxygen species and antioxidants on pathophysiology of male reproduction. *Indian J. Clin. Biochem.* **21**, 80–89 (2006).

11. Nobrega, F. G. & Tzagoloff, A. Assembly of the mitochondrial membrane system. *FEBS Lett.* **113**, 52–54 (1980).

12. Subramanian, K. *et al.* Coenzyme Q biosynthetic proteins assemble in a substrate-dependent manner into domains at ER-mitochondria contacts. *J. Cell Biol.* **218**, 1352–1368 (2019).

13. Brown, M. S. & Goldstein, J. L. Reductase , a Control Mechanism Coordinating. *J. Lipid Res.* **21**, (1980).

14. Mullen, P. J., Yu, R., Longo, J., Archer, M. C. & Penn, L. Z. The interplay between cell signalling and the mevalonate pathway in cancer. *Nat. Rev. Cancer* **16**, 718–731 (2016).

15. Wang, Y. & Hekimi, S. The Complexity of Making Ubiquinone. *Trends Endocrinol. Metab.* **30**, 929–943 (2019).

16. Mugoni, V. *et al.* Ubiad1 is an antioxidant enzyme that regulates eNOS activity by CoQ10 synthesis. *Cell* **152**, 504–518 (2013).

17. Pierrel, F. Impact of chemical analogs of 4-hydroxybenzoic acid on coenzyme Q biosynthesis: From inhibition to bypass of coenzyme Q deficiency. *Front. Physiol.* **8**, 1–7 (2017).

18. Wang, Y. & Hekimi, S. The Complexity of Making Ubiquinone. *Trends Endocrinol. Metab.* **30**, 929–943 (2019).

19. Stefely, J. A. & Pagliarini, D. J. Biochemistry of Mitochondrial Coenzyme Q Biosynthesis. *Trends Biochem. Sci.* **42**, 824–843 (2017).

20. Awad, A. M. *et al.* Coenzyme Q10 deficiencies: Pathways in yeast and humans. *Essays Biochem.* **62**, 361–376 (2018).

21. Ogasahara, S., Engel, A. G., Frens, D. & Mack, D. Muscle coenzyme Q deficiency in familial mitochondrial encephalomyopathy. *Proc. Natl. Acad. Sci. U. S. A.* **86**, 2379–2382 (1989).

22. Procopio, R. *et al.* Genetic mutation analysis of the COQ2 gene in Italian patients with multiple system atrophy. *Gene* **716**, 144037 (2019).

23. Wang, Y. & Hekimi, S. Understanding Ubiquinone. *Trends Cell Biol.* **26**, 367–378 (2016).

24. Stefely, J. A. & Pagliarini, D. J. Biochemistry of Mitochondrial Coenzyme Q Biosynthesis. *Trends Biochem. Sci.* **42**, 824–843 (2017).

25. Acosta, M. J. *et al.* Coenzyme Q biosynthesis in health and disease. *Biochim. Biophys. Acta* **1857**, 1079–1085 (2016).

26. Quinzii, C. *et al.* A mutation in para-hydroxybenzoate-polyprenyl transferase (COQ2) causes primary coenzyme Q10 deficiency. *Am. J. Hum. Genet.* **78**, 345–349 (2006).

27. Mollet, J. *et al.* in Ubiquinone Deficiency and Oxidative Phosphorylation Disorders. *Enzyme* **117**, (2007).

28. Diomedi-Camassei, F. *et al.* COQ2 nephropathy: a newly described inherited mitochondriopathy with primary renal involvement. *J. Am. Soc. Nephrol.* **18**, 2773–2780 (2007).

29. Yubero, D. *et al.* Biochemical diagnosis of coenzyme Q10deficiency. *Mol. Syndromol.* **5**, (2014).

30. Duncan, A. J. *et al.* A nonsense mutation in COQ9 causes autosomal-recessive neonatal-onset primary coenzyme Q10 deficiency: a potentially treatable form of mitochondrial disease. *Am. J. Hum. Genet.* **84**, 558–566 (2009).

31. Montini, G., Malaventura, C. & Salviati, L. Early coenzyme Q10 supplementation in primary coenzyme Q10 deficiency. *The New England journal of medicine* **358**, 2849–2850 (2008).

32. Emmanuele, V. *et al.* Heterogeneity of Coenzyme Q $_{10}$ Deficiency. *Arch. Neurol.* **69**, 361–365 (2012).

33. Hernández-Camacho, J. D., Bernier, M., López-Lluch, G. & Navas, P. Coenzyme Q10 Supplementation in Aging and Disease. *Front. Physiol.* **9**, 1–11 (2018).

34. Lopez, L. C. *et al.* Treatment of CoQ(10) deficient fibroblasts with ubiquinone, CoQ analogs, and vitamin C: time- and compound-dependent effects. *PLoS One* **5**, e11897 (2010).

35. Parson, W. W. & Rudney, H. THE BIOSYNTHESIS OF THE BENZOQUINONE RING OF UBIQUINONE FROM p-HYDROXYBENZALDEHYDE AND p-HYDROXYBENZOIC ACID IN RAT KIDNEY, AZOTOBACTER VINELANDII, AND BAKER'S YEAST. *Proc. Natl. Acad. Sci.* **51**, 444 LP – 450 (1964).

36. Brandt, W. *et al.* Molecular and structural basis of metabolic diversity mediated by

prenyldiphosphate converting enzymes. *Phytochemistry* **70**, 1758–1775 (2009).

37. González-Aragón, D. *et al.* Coenzyme Q and the regulation of intracellular steady-state levels of superoxide in HL-60 cells. *Biofactors* **25**, 31–41 (2005).

38. Xie, L. X. *et al.* Resveratrol and para-coumarate serve as ring precursors for coenzyme Q biosynthesis. *J. Lipid Res.* **56**, 909–919 (2015).

39. Acosta Lopez, M. J. *et al.* Vanillic Acid Restores Coenzyme Q Biosynthesis and ATP Production in Human Cells Lacking COQ6. *Oxid. Med. Cell. Longev.* **2019**, (2019).

40. Forsman, U., Sjöberg, M., Turunen, M. & Sindelar, P. J. 4-nitrobenzoate inhibits coenzyme Q biosynthesis in mammalian cell cultures. *Nat. Chem. Biol.* **6**, 515–517 (2010).

41. Quinzii, C. M., Tadesse, S., Naini, A. & Hirano, M. Effects of inhibiting CoQ10 biosynthesis with 4-nitrobenzoate in human fibroblasts. *PLoS One* **7**, e30606 (2012).

42. Stocker, R. & Suarna, C. Extrecellular reduction of ubiquinone-1 and -10 by human Hep G2 and blood cells. *BBA - Gen. Subj.* **1158**, 15–22 (1993).

43. Tadesse, S., Quinzii, C. M., Tadesse, S., Naini, A. & Hirano, M. Effects of Inhibiting CoQ10 Biosynthesis with 4- nitrobenzoate in Human Fibroblasts Effects of Inhibiting CoQ 10 Biosynthesis with 4-nitrobenzoate in Human Fibroblasts. (2016). doi:10.1371/journal.pone.0030606

44. Lauro, G. M., Di Lorenzo, N., Grossi, M., Maleci, A. & Guidetti, B. Prostaglandin E2 as an immunomodulating factor released in vitro by human glioma cells. *Acta Neuropathol.* **69**, 278–282 (1986).

45. Bergamini, C., Moruzzi, N., Sblendido, A., Lenaz, G. & Fato, R. A water soluble CoQ10 formulation improves intracellular distribution and promotes mitochondrial respiration in cultured cells. *PLoS One* **7**, 1–11 (2012).

46. Takada, M., Ikenoya, S., Yuzuriha, T. & Katayama, K. [17] Simultaneous Determination of Reduced and Oxidized Ubiquinones. *Methods Enzymol.* (1984). doi:10.1016/S0076-6879(84)05020-5

47. Contreras, J. a, Castro, M., Bocos, C., Herrera, E. & Lasunción, M. a. Combination of an

enzymatic method and HPLC for the quantitation of cholesterol in cultured cells. *J. Lipid Res.* **33**, 931–936 (1992).

48. Merlo-Pich, M., Deleonardi, G., Biondi, A. & Lenaz, G. Methods to detect mitochondrial function. *Experimental Gerontology* (2004). doi:10.1016/j.exger.2003.11.014

49. Giustarini, D., Dalle-Donne, I., Milzani, A., Fanti, P. & Rossi, R. Analysis of GSH and GSSG after derivatization with N-ethylmaleimide. *Nat. Protoc.* (2013). doi:10.1038/nprot.2013.095

50. He, J. *et al.* Persistence of the mitochondrial permeability transition in the absence of subunit c of human ATP synthase. *Proc. Natl. Acad. Sci. U. S. A.* **114**, 3409–3414 (2017).

51. Christofk, H. R. *et al.* The M2 splice isoform of pyruvate kinase is important for cancer metabolism and tumour growth. *Nature* **452**, 230–233 (2008).

52. Froehlich, K. *et al.* Generation of Multicellular Breast Cancer Tumor Spheroids: Comparison of Different Protocols. *J. Mammary Gland Biol. Neoplasia* **21**, 89–98 (2016).

53. Chazotte, B. Labeling mitochondria with mitotracker dyes. *Cold Spring Harb. Protoc.* **6**, 990–992 (2011).

54. Dagda, R. K. *et al.* Loss of PINK1 function promotes mitophagy through effects on oxidative stress and mitochondrial fission. *J. Biol. Chem.* **284**, 13843–13855 (2009).

55. Zhang, S. *et al.* Phosphorescent Light–Emitting Iridium Complexes Serve as a Hypoxia-Sensing Probe for Tumor Imaging in Living Animals. *Cancer Res.* (2010).

56. Frezza, C., Cipolat, S. & Scorrano, L. Organelle isolation: Functional mitochondria from mouse liver, muscle and cultured filroblasts. *Nat. Protoc.* **2**, 287–295 (2007).

57. Debacq-Chainiaux, F., Erusalimsky, J. D., Campisi, J. & Toussaint, O. Protocols to detect senescence-associated beta-galactosidase (SA-βgal) activity, a biomarker of senescent cells in culture and in vivo. *Nat. Protoc.* **4**, 1798–1806 (2009).

58. Contreras, J. A., Castro, M., Bocos, C., Herrera, E. & Lasuncion, M. A. Combination of an enzymatic method and HPLC for the quantitation of cholesterol in cultured cells. *J. Lipid Res.* **33**, 931–936 (1992).

59. Spinazzi, M., Casarin, A., Pertegato, V., Salviati, L. & Angelini, C. Assessment of mitochondrial respiratory chain enzymatic activities on tissues and cultured cells. *Nat. Protoc.* **7**, 1235–1246 (2012).

60. Barrientos, A., Fontanesi, F. & Díaz, F. Evaluation of the mitochondrial respiratory Chain and oxidative phosphorylation system using polarography and spectrophotometric enzyme assays. *Current Protocols in Human Genetics* (2009). doi:10.1002/0471142905.hg1903s63

61. Lowry, O. H., Rosebrough, N. J., Farr, A. L. & Randall, R. J. Protein measurement with the Folin-Phenol Reagent. *J. Biol. Cemistry* **193**, 265–275 (1951).

62. Yuan, J. S., Reed, A., Chen, F. & Stewart, C. N. Statistical analysis of real-time PCR data. *BMC Bioinformatics* **7**, 85 (2006).

63. Tao, Z., Goodisman, J. & Souid, A.-K. Oxygen measurement via phosphorescence: reaction of sodium dithionite with dissolved oxygen. *J. Phys. Chem. A* **112**, 1511–1518 (2008).

64. Pang, L. & Eyzaguirre, C. Different effects of hypoxia on the membrane potential and input resistance of isolated and clustered carotid body glomus cells. *Brain Res.* **575**, 167–173 (1992).

65. Lin, Y.-C., Tsai, P.-F. & Wu, J. S.-B. Protective effect of anthocyanidins against sodium dithionite-induced hypoxia injury in C6 glial cells. *J. Agric. Food Chem.* **62**, 5603–5608 (2014).

66. Mohanty, J. G., Jaffe, J. S., Schulman, E. S. & Raible, D. G. A highly sensitive fluorescent micro-assay of H2O2 release from activated human leukocytes using a dihydroxyphenoxazine derivative. *J. Immunol. Methods* **202**, 133–141 (1997).

67. GAFFNEY, B. J. The Chemistry of Spin Labels. *Spin Labeling* 183–238 (1976). doi:10.1016/b978-0-12-092350-2.50010-2

68. Lenaz, G. *et al.* Enhanced Activity of the Plasma Membrane Oxidoreductase in Circulating Lymphocytes from Insulin-Dependent Diabetes Mellitus Patients. *Biochem. Biophys. Res. Commun.* **290**, 1589–1592 (2002).

69. Picard, M., Shirihai, O. S., Gentil, B. J. & Burelle, Y. Mitochondrial morphology transitions and functions: implications for retrograde signaling? *Am. J. Physiol. Regul. Integr. Comp.*

Physiol. **304**, R393–R406 (2013).

70. Anavi, S., Hahn-Obercyger, M., Madar, Z. & Tirosh, O. Mechanism for HIF-1 activation by cholesterol under normoxia: A redox signaling pathway for liver damage. *Free Radic. Biol. Med.* **71**, 61–69 (2014).

71. Semenza, G. L. Hypoxia-inducible factor 1: Regulator of mitochondrial metabolism and mediator of ischemic preconditioning. *Biochim. Biophys. Acta - Mol. Cell Res.* **1813**, 1263–1268 (2011).

72. Iyer, N. V *et al.* Cellular and developmental control of O2 homeostasis by hypoxia-inducible factor 1 alpha. *Genes Dev.* **12**, 149–162 (1998).

73. Movafagh, S., Crook, S. & Vo, K. Regulation of Hypoxia-Inducible Factor-1a by Reactive Oxygen Species : New Developments in an Old Debate. *J. Cell. Biochem.* **116**, 696–703 (2015).

74. Zanna, C. *et al.* OPA1 mutations associated with dominant optic atrophy impair oxidative phosphorylation and mitochondrial fusion. *Brain* **131**, 352–367 (2007).

75. Mishra, P. & Chan, D. C. Metabolic regulation of mitochondrial dynamics. *J. Cell Biol.* **212**, 379–387 (2016).

76. Handy, D. E. & Loscalzo, J. Redox regulation of mitochondrial function. *Antioxidants and Redox Signaling* **16**, 1323–1367 (2012).

77. Liparulo, I. *et al.* Coenzyme Q biosynthesis inhibition induces HIF-1α stabilization and metabolic switch toward glycolysis. *FEBS J.* 1–19 (2020). doi:10.1111/febs.15561

78. Gomes, A. *et al.* Oxygen partial pressure is a rate-limiting parameter for cell proliferation in 3D spheroids grown in physioxic culture condition. *PLoS One* (2016). doi:10.1371/journal.pone.0161239

79. Nickless, A., Bailis, J. M. & You, Z. Control of gene expression through the nonsense-mediated RNA decay pathway. *Cell Biosci.* **7**, 1–12 (2017).

80. Wang, W. *et al.* Coenzyme q depletion reshapes mcf-7 cells metabolism. *Int. J. Mol. Sci.* **22**, 1–18 (2021).

81. Morita, M. *et al.* mTOR coordinates protein synthesis, mitochondrial activity and proliferation. *Cell Cycle* **14**, 473–480 (2015).

82. Yang, W. S. *et al.* Regulation of ferroptotic cancer cell death by GPX4. *Cell* **156**, 317–331 (2014).

83. Marcoff, L. & Thompson, P. D. The Role of Coenzyme Q10 in Statin-Associated Myopathy. *J. Am. Coll. Cardiol.* **49**, 2231–2237 (2007).

84. Tavintharan, S. *et al.* Reduced mitochondrial coenzyme Q10 levels in HepG2 cells treated with high-dose simvastatin: A possible role in statin-induced hepatotoxicity? *Toxicol. Appl. Pharmacol.* **223**, 173–179 (2007).

85. Zhang, M. *et al.* SIRT3 protects rotenone-induced injury in SH-SY5Y cells by promoting autophagy through the LKB1-AMPK-mTOR pathway. *Aging Dis.* **9**, 273–286 (2018).

86. Suárez-Rivero, J. M. *et al.* Intracellular cholesterol accumulation and coenzyme Q(10) deficiency in Familial Hypercholesterolemia. *Biochim. Biophys. acta. Mol. basis Dis.* **1864**, 3697–3713 (2018).

87. Summons, R. E., Bradley, A. S., Jahnke, L. L. & Waldbauer, J. R. Steroids, triterpenoids and molecular oxygen. *Philos. Trans. R. Soc. London. Ser. B, Biol. Sci.* **361**, 951–968 (2006).

88. Nguyen, A. D., McDonald, J. G., Bruick, R. K. & DeBose-Boyd, R. A. Hypoxia stimulates degradation of 3-hydroxy-3-methylglutaryl-coenzyme A reductase through accumulation of lanosterol and hypoxia-inducible factor-mediated induction of insigs. *J. Biol. Chem.* **282**, 27436–27446 (2007).

89. Prior, S. *et al.* Mitochondrial respiratory function induces endogenous hypoxia. *PLoS One* **9**, e88911–e88911 (2014).

90. Kim, A., Davis, R. & Higuchi, M. Intracellular oxygen determined by respiration regulates localization of Ras and prenylated proteins. *Cell Death Dis.* **6**, e1825–e1825 (2015).

91. Iommarini, L., Porcelli, A. M., Gasparre, G. & Kurelac, I. Non-Canonical Mechanisms Regulating Hypoxia-Inducible Factor 1 Alpha in Cancer. *Front. Oncol.* **7**, 286 (2017).

92. Subczynski, W. K., Raguz, M. & Widomska, J. Studying lipid organization in biological

membranes using liposomes and EPR spin labeling. *Methods Mol. Biol.* **606**, 247–269 (2010).

93. Dumas, D. *et al.* Membrane Fluidity and Oxygen Diffusion in Cholesterol-Enriched Erythrocyte Membrane. *Arch. Biochem. Biophys.* **341**, 34–39 (1997).

94. Pytel, E., Olszewska-Banaszczyk, M., Koter-Michalak, M. & Broncel, M. Increased oxidative stress and decreased membrane fluidity in erythrocytes of CAD patients. *Biochem. Cell Biol.* **91**, 315–318 (2013).

95. Duberley, K. Neurometabolic Implications of Coenzyme Q 10 Deficiency : Pathogenesis , Detection and Treatment Submitted By : (2013).

96. Li, F. *et al.* Regulation of HIF-1alpha stability through S-nitrosylation. *Mol. Cell* **26**, 63–74 (2007).

97. Jeffrey Man, H. S., Tsui, A. K. Y. & Marsden, P. A. Nitric Oxide and Hypoxia Signaling. *Vitamins & Hormones* 161–192 (2014). doi:10.1016/b978-0-12-800254-4.00007-6

98. Seagroves, T. N. *et al.* Transcription factor HIF-1 is a necessary mediator of the pasteur effect in mammalian cells. *Mol. Cell. Biol.* **21**, 3436–3444 (2001).

99. Lenaz, G. *et al.* Oxidative stress, antioxidant defences and aging. *BioFactors* **8**, 195–204 (1998).

100. Yoneda, M., Katsumata, K., Hayakawa, M., Tanaka, M. & Ozawa, T. Oxygen Stress Induces an Apoptotic Cell Death Associated with Fragmentation of Mitochondrial Genome. *Biochem. Biophys. Res. Commun.* **209**, 723–729 (1995).

101. Du, W. *et al.* HIF drives lipid deposition and cancer in ccRCC via repression of fatty acid metabolism. *Nat. Commun.* **8**, 1769 (2017).

102. Mylonis, I. *et al.* Hypoxia causes triglyceride accumulation by HIF-1-mediated stimulation of lipin 1 expression. *J. Cell Sci.* **125**, 3485–3493 (2012).

103. Mylonis, I., Simos, G. & Paraskeva, E. Hypoxia-Inducible Factors and the Regulation of Lipid Metabolism. *Cells* **8**, 214 (2019).

104. Morré, D. M., Lenaz, G. & Morré, D. J. Surface oxidase and oxidative stress propagation in aging. *J. Exp. Biol.* **203**, 1513–1521 (2000).

105. Kishi, T., Morré, D. M. & Morré, D. J. The plasma membrane NADH oxidase of HeLa cells has hydroquinone oxidase activity. *Biochim. Biophys. Acta - Bioenerg.* **1412**, 66–77 (1999).

106. Sun, I. L. *et al.* Requirement for coenzyme Q in plasma membrane electron transport. *Proc. Natl. Acad. Sci. U. S. A.* **89**, 11126–11130 (1992).

107. Larm, J. A. *et al.* Increase of plasma membrane oxidoreductase activity is not correlated with the production of extracellular Superoxide radicals in human Namalwa cells. *Protoplasma* **184**, 173–180 (1995).

108. Navarro, F. *et al.* Vitamin E and selenium deficiency induces expression of the ubiquinone-dependent antioxidant system at the plasma membrane. *FASEB J.* **12**, 1665–1673 (1998).

109. Turcotte, M. L., Parliament, M., Franko, A. & Allalunis-Turner, J. Variation in mitochondrial function in hypoxia-sensitive and hypoxia-tolerant human glioma cells. *Br. J. Cancer* **86**, 619–624 (2002).

110. Haynes, V., Traaseth, N. J., Elfering, S., Fujisawa, Y. & Giulivi, C. Nitration of specific tyrosines in FoF1 ATP synthase and activity loss in aging. *Am. J. Physiol. Endocrinol. Metab.* **298**, E978–E987 (2010).

111. Huang, L.-J., Chuang, I.-C., Dong, H.-P. & Yang, R.-C. Hypoxia-Inducible Factor 1α Regulates the Expression of the Mitochondrial ATPase Inhibitor Protein (IF1) in Rat Liver. *Shock* **36**, 90–96 (2011).

112. Quinzii, C. M. *et al.* Reactive oxygen species, oxidative stress, and cell death correlate with level of CoQ10 deficiency. *FASEB J.* **24**, 3733–3743 (2010).

113. Mugoni, V. *et al.* Ubiad1 is an antioxidant enzyme that regulates eNOS activity by CoQ10 synthesis. *Cell* **152**, 504–518 (2013).

114. Mourier, A. *et al.* Mitofusin 2 is required to maintain mitochondrial coenzyme Q levels. *J. Cell Biol.* **208**, 429 LP – 442 (2015).

115. Del Dotto, V., Fogazza, M., Carelli, V., Rugolo, M. & Zanna, C. Eight human OPA1 isoforms, long and short: What are they for? *Biochim. Biophys. Acta - Bioenerg.* **1859**, 263–269 (2018).

116. An, H.-J. *et al.* Higd-1a interacts with Opa1 and is required for the morphological and

functional integrity of mitochondria. *Proc. Natl. Acad. Sci.* **110**, 13014–13019 (2013).

117. Brown, A. J. & Galea, A. M. CHOLESTEROL AS AN EVOLUTIONARY RESPONSE TO LIVING WITH OXYGEN. *Evolution (N. Y).* no-no (2010). doi:10.1111/j.1558-5646.2010.01011.x

118. Duberley, K. E. *et al.* Effect of Coenzyme Q10 supplementation on mitochondrial electron transport chain activity and mitochondrial oxidative stress in Coenzyme Q10 deficient human neuronal cells. *Int. J. Biochem. Cell Biol.* **50**, 60–63 (2014).

119. Duberley, K. E. C. *et al.* Human neuronal coenzyme Q10 deficiency results in global loss of mitochondrial respiratory chain activity, increased mitochondrial oxidative stress and reversal of ATP synthase activity: Implications for pathogenesis and treatment. *J. Inherit. Metab. Dis.* **36**, 63–73 (2013).

120. Liparulo, I. *et al.* Coenzyme Q biosynthesis inhibition induces HIF-1α stabilization and metabolic switch toward glycolysis. *FEBS J.* febs.15561 (2020). doi:10.1111/febs.15561

121. Fink, B. D. *et al.* Oxaloacetic acid mediates ADP-dependent inhibition of mitochondrial complex II–driven respiration. *J. Biol. Chem.* **293**, 19932–19941 (2018).

122. Tretter, L., Patocs, A. & Chinopoulos, C. Succinate, an intermediate in metabolism, signal transduction, ROS, hypoxia, and tumorigenesis. *Biochim. Biophys. Acta - Bioenerg.* (2016). doi:10.1016/j.bbabio.2016.03.012

123. Zhang, S. *et al.* Phosphorescent light-emitting iridium complexes serve as a hypoxia-sensing probe for tumor imaging in living animals. *Cancer Res.* **70**, 4490–4498 (2010).

124. Aguer, C. *et al.* Galactose Enhances Oxidative Metabolism and Reveals Mitochondrial Dysfunction in Human Primary Muscle Cells. *PLoS One* **6**, e28536 (2011).

125. Kase, E. T. *et al.* Remodeling of Oxidative Energy Metabolism by Galactose Improves Glucose Handling and Metabolic Switching in Human Skeletal Muscle Cells. *PLoS One* (2013). doi:10.1371/journal.pone.0059972

126. Chen, Q. *et al.* Rewiring of Glutamine Metabolism Is a Bioenergetic Adaptation of Human Cells with Mitochondrial DNA Mutations. *Cell Metab.* **27**, 1007-1025.e5 (2018).

127. Montero, J. *et al.* Mitochondrial Cholesterol Contributes to Chemotherapy Resistance in

Hepatocellular Carcinoma. *Cancer Res.* **68**, 5246–5256 (2008).

128. Su, J. *et al.* Bcl-2 family proteins are involved in the signal crosstalk between endoplasmic reticulum stress and mitochondrial dysfunction in tumor chemotherapy resistance. *Biomed Res. Int.* **2014**, 234370 (2014).

129. Desbats, M. A. *et al.* The COQ2 genotype predicts the severity of Coenzyme Q10 deficiency. *Hum. Mol. Genet.* **25**, 4256–4265 (2016).

130. Khaitan, D., Chandna, S., Arya, M. B. & Dwarakanath, B. S. Establishment and characterization of multicellular spheroids from a human glioma cell line ; Implications for tumor therapy. **13**, 1–13 (2006).

131. Bersuker, K. *et al.* The CoQ oxidoreductase FSP1 acts parallel to GPX4 to inhibit ferroptosis. *Nature* **575**, 688–692 (2019).

132. Yecies, J. L. & Manning, B. D. mTOR links oncogenic signaling to tumor cell metabolism. *J. Mol. Med.* **89**, 221–228 (2011).